

# CMS Draft Analysis Note

*The content of this note is intended for CMS internal use and distribution only*

2013/08/14

Head Id: 202658

Archive Id: 202665

Archive Date: 2013/08/14

Archive Tag: trunk

## Search for high mass exotic resonances decaying to WW in the semi-leptonic channel

Nural Akchurin<sup>1</sup>, Jake Anderson<sup>2</sup>, Chayanit Asawatangtrakuldee<sup>11</sup>, Tariq Aziz<sup>14</sup>, Andrew Beretvas<sup>2</sup>, Jeffrey Berryhill<sup>2</sup>, Pushpa Bhat<sup>2</sup>, Sarah Boutle<sup>4</sup>, Chris Clarke<sup>5</sup>, Analu Custodio<sup>10</sup>, Jordan Damgov<sup>1</sup>, Leonardo Di Matteo<sup>3</sup>, Phil Dudero<sup>1</sup>, Ricardo Eusebi<sup>6</sup>, Raffaele Gerosa<sup>3</sup>, Pietro Govoni<sup>3</sup>, Dan Green<sup>2</sup>, Joey Goodell<sup>4</sup>, Robert Harr<sup>5</sup>, Pratima Jindal<sup>13</sup>, Ajay Kumar<sup>7</sup>, Kristina Krylova<sup>5</sup>, Kevin Lannon<sup>9</sup>, Sung-Won Lee<sup>1</sup>, Qiang Li<sup>11</sup>, Shuai Liu<sup>11</sup>, Wuming Luo<sup>9</sup>, Yajun Mao<sup>11</sup>, Kellen McGee<sup>5</sup>, Kalanand Mishra<sup>2</sup>, Gagan Mohanty<sup>14</sup>, Md. Naimuddin<sup>7</sup>, Chris Neu<sup>4</sup>, Ilya Osipenkov<sup>6</sup>, Bibhuti Parida<sup>14</sup>, Alexx Perloff<sup>6</sup>, Kirti Ranjan<sup>7</sup>, Sasha Sakharov<sup>5</sup>, Ram K Shivpuri<sup>7</sup>, Kevin Siehl<sup>5</sup>, Andre Sznajder<sup>10</sup>, Nhan V. Tran<sup>2</sup>, Zijun Xu<sup>11</sup>, Weimin Wu<sup>2</sup>, John Wood<sup>4</sup>, Fan Yang<sup>2</sup>, Francisco Yumiceva<sup>2</sup>, and Wei Zou<sup>11</sup>

<sup>1</sup> Texas Tech University, Lubbock, Texas, USA

<sup>2</sup> Fermi National Accelerator Laboratory, Batavia, Illinois, USA

<sup>3</sup> Milano-Bicocca University and INFN, Milan, Italy

<sup>4</sup> University of Virginia, Charlottesville, Virginia, USA

<sup>5</sup> Wayne State University, Detroit, Michigan, USA

<sup>6</sup> Texas A&M University, College Station, Texas, USA

<sup>7</sup> Delhi University, Delhi, India

<sup>8</sup> University of Nebraska at Lincoln, Nebraska, USA

<sup>9</sup> University of Notre Dame, Notre Dame, Indiana, USA

<sup>10</sup> Universidade do Estado do Rio de Janeiro (UERJ), Brazil

<sup>11</sup> Peking University, China

<sup>12</sup> CERN

<sup>13</sup> Princeton University, New Jersey, USA

<sup>14</sup> Tata Institute of Fundamental Research, Mumbai, India

## Abstract

In this note, we describe a search for new physics at high mass in the  $WW$  final state. The search is performed in the semi-leptonic channel where the hadronic  $W$  decay is merged and the decay products are contained in one large  $R$  jet. Jet substructure techniques are used in identifying the hadronic  $W$ . Benchmark searches are performed for Gravitons decaying to  $WW$  in warped extra-dimension models.

DRAFT

This box is only visible in draft mode. Please make sure the values below make sense.

---

PDFAuthor: Raffaele Gerosa, Pietro Govoni, Nhan Tran, Zijun Xu  
PDFTitle: Search for Exotic resonances decaying to  $WW$  in the semi-leptonic channel  
PDFSubject: CMS  
PDFKeywords: CMS, physics, software, computing

---

Please also verify that the abstract does not use any user defined symbols

## 1 Contents

2	1	Introduction . . . . .	2
3	2	Data and simulated samples . . . . .	2
4	2.1	Data samples . . . . .	2
5	2.2	Monte Carlo Samples . . . . .	3
6	3	Objects Definition . . . . .	5
7	3.1	Physics Objects . . . . .	5
8	3.2	Event-Level Criteria . . . . .	8
9	3.3	Lepton reconstruction, selection and trigger efficiencies . . . . .	8
10	4	Identifying Merged W bosons . . . . .	10
11	5	Analysis Strategy . . . . .	12
12	5.1	Event Selection . . . . .	12
13	5.2	Data to MC comparison . . . . .	12
14	5.3	Control Region, $t\bar{t}$ . . . . .	20
15	5.4	W+Jets Background Extraction, Sideband $\alpha$ procedure . . . . .	27
16	5.5	Signal Model . . . . .	45
17	6	Systematic Uncertainties . . . . .	49
18	6.1	Background Normalization and Shape . . . . .	49
19	6.2	Shape uncertainty on the $t\bar{t}$ shape . . . . .	49
20	6.3	Other systematic on Background Normalization . . . . .	52
21	6.4	Signal Normalization and Shape . . . . .	54
22	7	Statistical Interpretation . . . . .	58
23	7.1	Blinding Policy . . . . .	58
24	7.2	Upper Limits for Bulk Graviton Production . . . . .	58
25	8	Final Result Reported in the PAS . . . . .	62
26	8.1	Control Region $t\bar{t}$ . . . . .	62
27	8.2	W+Jets Background Extraction . . . . .	64
28	9	Conclusions . . . . .	73
29	A	Choice of W+jets Fit Function . . . . .	74
30	A.1	Result in the [0.4-1.3] TeV Range . . . . .	74
31	A.2	Result in the [0.7-3.0] TeV Range . . . . .	74
32	B	Closure test for alpha method . . . . .	83
33	B.1	Closure Test A1 → A2 . . . . .	83
34	B.2	Closure Test A → B . . . . .	92
35	C	Analysis Robustness Test . . . . .	101
36	C.1	Limit Extraction without any Systematic Uncertainty . . . . .	101
37	C.2	Limit Extraction without Systematic Uncertainty on Alpha . . . . .	101
38	C.3	Limit Extraction without Low Purity Categories . . . . .	102
39	C.4	Limit Extraction with full CLs . . . . .	103

## 40 1 Introduction

41 The LHC represents a new energy regime in particle physics. Searches for new physics in the  
 42 high mass region at the kinematic limit of the machine is often at very high pTs. To improve  
 43 the rate of these new final states, it is often worthwhile to search in hadronic decay modes.  
 44 With very high pT hadronic objects, the  $q\bar{q}$  decay products are often merged into a single jet  
 45 to the point where traditional di-jet searches cannot be performed. In this case, we use jet  
 46 substructure techniques for identifying single jets that have originated from a highly boosted  
 47 hadronically decaying W boson. In this analysis note, the main benchmark signal model we  
 48 consider is a Graviton decaying in the exclusive  $WW \rightarrow \ell\nu q\bar{q}'$  final state.

49 This analysis note presents searches in the  $WW \rightarrow \ell\nu j$  final state with the full 2012 8 TeV CMS  
 50 dataset. In Sec. 2, data and simulated samples, used in this study, are described. In Sec. 3, there  
 51 is a brief description of trigger details and physics objects while, in Sec. 4, we introduce several  
 52 jet substructure concepts, which are relevant in the identification of merged W bosons and in  
 53 the optimization of how we select W-jet candidates. Sec. 5 outlines the basic cuts of the analysis,  
 54 the procedures for estimating each background contribution and cross-checks involving control  
 55 samples. Finally, Sec. 6 describes the systematic uncertainties considered in this analysis and,  
 56 in Sec 7, results are presented in the search for benchmark resonances decaying to a pair of W  
 57 bosons.

## 58 2 Data and simulated samples

### 59 2.1 Data samples

60 The data sample considered in this analysis was recorded by the CMS experiment in 2012. Only  
 61 certified runs and luminosity sections are considered, which means that a good functioning of  
 62 all CMS sub-detectors is required. The total statistics analyzed corresponds to an integrated  
 63 luminosity of approximately  $19.3 \text{ fb}^{-1}$ . The current uncertainty on the luminosity is 4.4%.  
 64 The dataset and the corresponding run ranges are listed in Table 1; they refers to the CMS  
 65 Prompt Reconstruction (PromptReco). All samples have been processed using a CMSSW\_5\_3\_2  
 66 release version.

Dataset name	Run range	$L [\text{fb}^{-1}]$
/SingleMu/Run2012A-13Jul2012-v1/AOD	190456-193621	0.809
/SingleElectron/Run2012A-13Jul2012-v1/AOD		
/SingleMu/Run2012A-recover-06Aug2012-v1/AOD	190782-190949	0.082
/SingleElectron/Run2012A-recover-06Aug2012-v1/AOD		
/SingleMu/Run2012B-13Jul2012-v1/AOD	193833-196531	4.383
/SingleElectron/Run2012B-13Jul2012-v1/AOD		
/SingleMu/Run2012C-24Aug2012-v1/AOD	198022-198913	0.489
/SingleElectron/Run2012C-24Aug2012-v1/AOD		
/SingleMu/Run2012C-PromptReco-v2/AOD	198934-203746	6.285
/SingleElectron/Run2012C-PromptReco-v2/AOD		
/SingleMu/Run2012D-PromptReco-v1/AOD	203894-205618	7.238
/SingleElectron/Run2012D-PromptReco-v1/AOD		

Table 1: Summary of data samples used and run ranges of applicability.

---

## 67 2.2 Monte Carlo Samples

### 68 2.2.1 Signal Samples

69 The signal model is taken to be the Randall-Sundrum warped extra-dimensions model [1]. The  
70 signal MC samples, for different Graviton mass hypothesis, are privately produced with the  
71 JHU generator [2, 3] and are showered with Pythia 6 using the central production workflow,  
72 with TuneZ2Star configuration. The inclusive cross section for  $pp \rightarrow G_{bulk} \rightarrow WW \rightarrow l\nu + qq$   
73 are calculated via CALCHEP generator [4] and their values are reported in Table 2.  
74 GEN-SIM files were produced with CMSSW version 5\_2\_6, which uses GEANT4 version 9.4.p03-  
75 cms for the full simulation of the CMS detector. The DIGI-RAW and RECO steps were pro-  
76 duced with CMSSW version 5\_3\_2\_patch4. These steps include an approximate description  
77 of pileup effects through the mixing of simulated minimum bias at the DIGI level.  
78 The simulated minimum bias events used are taken from the dataset  
79 /MinBias\_TuneZ2star\_8TeV-pythia6/Summer12-START50\_V13-v3/GEN-SIM, and the  
80 distribution of the number of pileup events superimposed to the signal event was done accord-  
81 ing to the 2012\_Summer\_50ns\_PoissonOOTPU configuration.

$M_G$ [GeV]	Sample Name	cross-section (fb)
600	BulkG_WW_lvjj_c0p2_M600-JHU-v2	1.500
700	BulkG_WW_lvjj_c0p2_M700-JHU-v2	5.478
800	BulkG_WW_lvjj_c0p2_M800-JHU-v2	2.280
900	BulkG_WW_lvjj_c0p2_M900-JHU-v2	1.048
1000	BulkG_WW_lvjj_c0p2_M1000-JHU-v2	0.511
1100	BulkG_WW_lvjj_c0p2_M1100-JHU-v2	0.265
1200	BulkG_WW_lvjj_c0p2_M1200-JHU-v2	0.141
1300	BulkG_WW_lvjj_c0p2_M1300-JHU-v2	7.903e-02
1400	BulkG_WW_lvjj_c0p2_M1400-JHU-v2	4.525e-02
1500	BulkG_WW_lvjj_c0p2_M1500-JHU-v2	2.654e-02
1600	BulkG_WW_lvjj_c0p2_M1600-JHU-v2	1.577e-02
1700	BulkG_WW_lvjj_c0p2_M1700-JHU-v2	9.569e-03
1800	BulkG_WW_lvjj_c0p2_M1800-JHU-v2	5.871e-03
1900	BulkG_WW_lvjj_c0p2_M1900-JHU-v2	3.667e-03
2000	BulkG_WW_lvjj_c0p2_M2000-JHU-v2	2.307e-03
2100	BulkG_WW_lvjj_c0p2_M2100-JHU-v2	1.458e-03
2200	BulkG_WW_lvjj_c0p2_M2200-JHU-v2	9.399e-04
2300	BulkG_WW_lvjj_c0p2_M2300-JHU-v2	6.035e-04
2400	BulkG_WW_lvjj_c0p2_M2400-JHU-v2	3.910e-04
2500	BulkG_WW_lvjj_c0p2_M2500-JHU-v2	2.551e-04

Table 2: Summary of Monte Carlo signal samples used in the analysis. The quoted cross-sections refer to the  $G_{bulk} \rightarrow WW \rightarrow l\nu + qq$ ,  $l = e, \mu$  final states. The chosen value of  $\tilde{k} = k/M_{pl}$  is equal to 0.2.

### 82 2.2.2 Backgrounds

83 All the background MC samples considered in this analysis come from the official “Sum-  
84 mer12\_53X” production: Summer12\_DR53X-PU\_S10\_START53\_V7A-v1. Events from Sum-  
85 mer12 samples were reconstructed making use of a CMSSW\_5\_3\_X release version. The simu-  
86 lated samples are re-weighted to represent the distribution of number of pp interactions per  
87 bunch crossing (pile-up) as measured in the data.

The main backgrounds considered are W+jets, WW/WZ, Drell-Yan,  $t\bar{t}$  and single top. We considered two W+jet samples with different parton shower models, Pythia6 and Herwig++. Both these W+jet samples are produced with the generated  $W p_T > 100$  GeV to provide more statistics in the boosted topology. In addition, we have another simulated sample with  $W p_T > 180$  GeV to increase statistics for the highest mass points. Finally, the  $W p_T > 100$  GeV and  $W p_T > 180$  GeV samples are combined using the generator level  $p_T$  to maximize the available simulated statistics. Details of the background samples are presented in Table 3; cross section values are taken from this twiki<sup>1</sup>. W+jets cross section is rescaled by the NNLO/LO k-factor  $\sim 1.3$ , neglecting the effect of the change in the  $W p_T$  distribution moving from LO to NNLO, while, for the other processes, NLO or approx. NNLO calculations have been considered.

process	sample name	cross-section (pb)
W+jets	/WJetsToLNu_PtW-100_TuneZ2star_8TeV-madgraph	$222.5 \times 1.3$
W+jets	/WJetsToLNu_PtW-180_TuneZ2star_8TeV-madgraph	$26.4 \times 1.3$
W+jets (herwig)	/WJetsToLNu_PtW100_8TeVHerwigpp	$222.5 \times 1.3$
WW	/WW_TuneZ2star_8TeV_pythia6_tauola	54.8
WZ	/WZ_TuneZ2star_8TeV_pythia6_tauola	32.3
ZZ	/ZZ_TuneZ2star_8TeV_pythia6_tauola	8.05
$t\bar{t}$	/TTJets_MassiveBinDECAY_TuneZ2star_8TeV-madgraph-tauola	225.2
$t\bar{t}$	/TTJets_scaleup_TuneZ2star_8TeV-madgraph-tauola	225.1
$t\bar{t}$	/TTJets_scaledown_TuneZ2star_8TeV-madgraph-tauola	228.1
$t\bar{t}$	/TTJets_matchingup_TuneZ2star_8TeV-madgraph-tauola	228.3
$t\bar{t}$	/TTJets_matchingdown_TuneZ2star_8TeV-madgraph-tauola	214.6
$t\bar{t}$	/TT_CT10_TuneZ2star_8TeV-powheg-tauola	225.2
Z+jets	/DYJetsToLL_M-50_TuneZ2Star_8TeV-madgraph-tarball	3503
single top	/T_t-channel_TuneZ2star_8TeV-powheg-tauola	56.4
single top	/T_s-channel_TuneZ2star_8TeV-powheg-tauola	3.79
single top	/T_tW-channel-DR_TuneZ2star_8TeV-powheg-tauola	11.2
single top	/Tbar_t-channel_TuneZ2star_8TeV-powheg-tauola	30.7
single top	/Tbar_tW-channel-DR_TuneZ2star_8TeV-powheg-tauola	11.2
single top	/Tbar_s-channel_TuneZ2star_8TeV-powheg-tauola	1.76

Table 3: Summary of the Monte Carlo samples used in the analysis.

<sup>1</sup><https://twiki.cern.ch/twiki/bin/viewauth/CMS/StandardModelCrossSectionsat8TeV>

---

## 98 3 Objects Definition

99 In this section, we first describe the criteria applied to objects selected in the event and then we  
100 describe the requirements made at the event-level.

101 **3.1 Physics Objects**

102 The analysis relies on the standard reconstruction algorithms produced by the CMS commu-  
103 nity. A basic set of noise filters are required:

- 104 • **Good Offline Primary Vertex Filter:** it requires at least one vertex in the event with:  
105 number degrees of freedom greater than 4, absolute value of longitudinal distance  
106 from nominal interaction point ( $abs(z)$ ) less than 24 cm and transverse distance from  
107 z-axis ( $\rho$ ) less than 2 cm.
- 108 • **noscrapingFilterPath**
- 109 • **HBHENoiseFilterPath**
- 110 • **trackingFailureFilterPath**
- 111 • **CSCTightHaloFilterPath**
- 112 • **hcalLaserEventFilterPath**
- 113 • **eeBadScFilterPath**
- 114 • **EcalDeadCellTriggerPrimitiveFilterPath**

115 The vertex with the highest tracks sum of  $pT^2$  is taken as the primary one, it is used to identify  
116 the tracks associated to the hard scattering and for PU removal in jet clustering (charged hadron  
117 subtraction).

118 The PF2PAT procedure is used to coherently define the collection of particle-flow jets, leptons  
119 and MET considered in the event selection. The technical details of the software configuration  
120 can be found in the group twiki page <sup>2</sup>.

121 The signature of the analysis consists in an isolated high  $p_T$  lepton (electron or muon), large  
122 missing transverse energy  $E_T^{\text{miss}}$  and a large R jet containing the full decay of a hadronically  
123 decaying W boson.

124 **3.1.1 Electron Cuts (e+jets)**

125 Electrons are reconstructed in CMS using a Gaussian-Sum-Filter algorithm (GSF); in addition it  
126 is required that each GSF electron must pass the HEEPID identification criterion [5], following  
127 the latest version of HEEP selection (v4.1):

- 128 • The electron reconstruction should be driven by ECAL deposits (ecalDriven).
- 129 • Number of inner layer hits greater than two.
- 130 • Supercluster transverse energy ( $E_T$ ) greater than 35 GeV.
- 131 • Reject electron with supercluster pseudorapidity ( $\eta_{SC}$ ) within the barrel-endcap gap  
132 region ( $1.442 < |\eta_{SC}| < 1.556$ ).
- 133 •  $|\Delta\eta_{in}|$  smaller than 0.005 (0.007) for barrel (endcap) electrons.
- 134 •  $|\Delta\phi_{in}|$  smaller than 0.006 for both barrel and endcap electrons.
- 135 •  $\sigma_{i\eta i\eta}$  smaller than 0.003 only for endcap electrons.

---

<sup>2</sup><https://twiki.cern.ch/twiki/bin/view/CMSPublic/SWGuidePF2PAT>

- The ratio between the energy deposition in the hadronic and the electromagnetic calorimeter ( $H/E$ ) smaller than 0.05.
- Have either  $E_{2x5}/E_{5x5}$  larger than 0.94 or  $E_{1x5}/E_{5x5}$  greater than 0.83.
- Transverse impact parameter  $|d_{xy}|$ , respect to the selected primary vertex, less than 0.02 (0.05) cm for barrel (endcap) electrons.
- Electron candidates have also to be isolated from charged hadron activity in the detector, requiring that the sum of tracks transverse momentum ( $I_{tk}$ ), within an isolation cone of  $\Delta R = 0.3$  around the GSF track, should be less than 5 GeV.
- The sum of the electromagnetic ( $I_{em}$ ) and the hadronic ( $I_{had}$ ) isolation, calculated in a cone of  $\Delta R = 0.3$  around the electron track, is corrected for the pile-up using an effective correction ( $0.28 \cdot \rho$ ), where  $\rho$  is the average particle energy density, coming from pile-up, calculated independently for each event. It is required  $I_{em} + I_{had} - (0.28 \cdot \rho)$  smaller than  $2+0.003 \cdot E_T$  for electrons in the barrel, while, in the endcap, smaller than  $2.5+0.03 \cdot [E_T-50]$  (2.5) for electrons with  $E_T > 50$  ( $< 50$ ) GeV.

Finally, by means of a kinematic selection on the transverse momentum, *tight electrons* are defined as HEEP electrons with  $p_T > 90$  GeV and  $|\eta| < 2.5$ , while *loose electrons* when  $p_T > 35$  GeV and  $|\eta| < 2.5$ <sup>3</sup>.

### 3.1.2 Muon Cuts (mu+jets)

Muons are reconstructed by tracker and global algorithms [6]: one proceeds from the inner tracker outwards, the other one starts from tracks measured in the muon chambers matching them with the ones reconstructed in the silicon tracker. Muons are identified by means of the high- $p_T$  muon selection (old version before CMSSW\_5\_3\_6\_patch1):

- Each muon must be both a tracker and a global muon.
- Number of pixel hits greater than zero.
- Number of muon hits larger than zero.
- Number of matched muon station greater than one.
- Transverse impact parameter  $|d_{xy}|$ , respect to the selected primary vertex, less than 0.2 cm.
- Longitudinal impact parameter  $|d_z|$ , respect to the selected primary vertex, less than 0.5 cm.
- Number of tracker layers with a valid hits greater than eight.

The selected muon candidates have also to be isolated from charged hadron activity in the detector, requiring that the sum of tracks transverse momentum ( $I_{tk}$ ), within an isolation cone of  $\Delta R = 0.3$  around the muon track, should be  $I_{tk}/p_T < 0.1$ .

In addition, looking at the muon transverse momentum, we define a *tight muon* as a high- $p_T$  muon with  $p_T > 50$  GeV and  $|\eta| < 2.1$ , while a *loose muon* when it has a  $p_T > 20$  GeV and  $|\eta| < 2.4$ <sup>4</sup>.

<sup>3</sup>This kinematic requirements are motivated by the thresholds of the HLT trigger slots in use; for electron+jets final state → *HLT\_Ele80\_CaloIDVT\**, see Sec.3.3.1.

<sup>4</sup>This kinematic requirements are motivated by the thresholds of the HLT trigger slots in use; for muon+jets final state → *HLT\_Mu40\_eta2p1\**, see Sec.3.3.1

174 **3.1.3 Jet Selection**

175 Jets are reconstructed starting from the set of objects produced by the particle flow algorithm [7]  
 176 [8] [9].

177 Two collections of jets are used in this analysis: the CMS standard R=0.5 jets reconstructed  
 178 with the anti-kT algorithm [10] (AK5) and R=0.8 jets reconstructed with the Cambridge-Aachen  
 179 one [11] (CA8). During the jet clustering, charged hadrons, originating from pile-up vertices,  
 180 are skipped according to the Charged Hadron Subtraction (CHS) procedure.

181 **CA8 Jet Selection**

182 In this analysis, CA8 jets are used as the default jet collection for identifying merged W bosons,  
 183 as already done in other approved CMS analysis [? ]. Dedicated corrections for CA8 jets do not  
 184 exist, so AK7 jet corrections are applied to CA8 uncorrected jets. Systematic differences due to  
 185 using AK7 corrections are computed in Sec. 6.

186 In CMS, jets are corrected such that their measured energy correctly reproduces the energy of  
 187 the initial particle. The standard L2 (relative) correction makes the jet response flat vs  $\eta$ , while  
 188 the standard L3 (absolute) correction brings the jet closer to the  $p_T$  of a matched generated  
 189 jet, created using generator level input and a similar jet clustering algorithm. The L2 and L3  
 190 corrections are calculated using simulated events, thus a L2L3 residual correction is applied to  
 191 fix the discrepancies between data and Monte Carlo [12]. JEC correction for CA8 jets are taken  
 192 directly from the chosen Global Tags: GR\_P\_V39\_AN3 for data and START53\_V15 for MC.

193 W merged jet candidates are selected from a skimmed CA8 jet collection obtained requiring:

- 194 •  $p_T^{CA8} > 80 \text{ GeV}$  and  $|\eta| < 2.4$ .
- 195 • Cleaning between CA8 jet and isolated tight lepton (electron or muon):  $\Delta R(j, l) > 1$ .
- 196 • Loose Jet ID: muon energy fraction  $< 0.99$ , photon energy fraction  $< 0.99$ , electro-  
 197 magnetic energy fraction  $< 0.99$ , number of jet constituent greater than one, neutral  
 198 and charged hadron energy fraction respectively  $< 0.99$  and  $> 0$ .

199 **AK5 Jet Selection**

200 AK5 jets are used for some supporting cuts, such as the number of additional jets originated  
 201 from a  $b$  quark, and they have their own dedicated corrections. Jets candidate are selected  
 202 requiring:  $p_T^{AK5} > 30 \text{ GeV}$ ,  $|\eta| < 2.4$  and passing Loose JetID criteria. In addition, jets over-  
 203 lapping with a loose lepton ( $e$  or  $\mu$ ), within a cone of  $\Delta R = 0.3$ , are discarded. AK5 jets are  
 204 identified as coming from a  $b$ -quark according to the Combined Secondary Vertex algorithm  
 205 (CSV), choosing a medium working point.

206 B-tag data/MC scale factors (SF), for the CSV medium working point, are applied in order to  
 207 weight each simulated event, according to the official b-tag POG recipe<sup>5</sup>. These SFs are around  
 208  $\sim 0.95$  for  $b$ -jets and  $\sim 1.2$  for light flavours and gluons; the b-tag efficiency, in bins of  $p_T$ ,  $\eta$   
 209 and flavour, is measured independently for each simulated sample after the basic selections  
 210 described is Sec.3.2.

211 **3.1.4 Missing Transverse Energy**

212 An accurate MET measurement is essential for distinguishing the W signal from QCD back-  
 213 grounds. We use the MET estimate defined by the Particle Flow algorithm (PF MET) as the  
 214 negative vectorial sum of all the reconstructed PF Candidates transverse momentum. A good

<sup>5</sup>Method 1a indicated in this official twiki:

[https://twiki.cern.ch/twiki/bin/viewauth/CMS/BTagSFMethodsb\\_tagging\\_efficiency\\_in\\_MC\\_sample](https://twiki.cern.ch/twiki/bin/viewauth/CMS/BTagSFMethodsb_tagging_efficiency_in_MC_sample).

215 agreement is found between the  $E_T^{miss}$  distributions of  $W \rightarrow l\nu$  events in data and simulation [13]. The resolution for inclusive multi-jet samples and for  $W \rightarrow l\nu$  events is also well  
216 reproduced by the simulation.

218 The standard PF MET is corrected to account for jet energy corrections (Type-1 MET correction).  
219 The jet collection used for Type-I is the AK5 CHS, with a minimum jet  $p_T$  of 10 GeV. In addition,  
220 jets with EM fraction greater than 90% or identified as muons are not used.

221 Finally, missing energy is also correct for a  $\phi$  modulation observed in data as well as in Monte  
222 Carlo. This modulation is due to a systematic shift of the x/y momentum components which  
223 increases linearly with the number of reconstructed vertices. Since the magnitude of the shift is  
224 different between data and MC, a dedicated correction has been developed by JetMET experts<sup>6</sup>  
225 and applied in the analysis (MET x/y Shift Correction).

226 We require the event to have missing transverse energy MET, obtained after the aforementioned  
227 corrections, in excess of 50 GeV in case of muon sample and 80 GeV in case of the electron one.  
228 These cuts are designed to reduce the background from QCD multijet production.

## 229 3.2 Event-Level Criteria

230 In the e+jets channel, we select events that contain exactly one tight electron candidate fulfilling  
231 the selection criteria described in Sec. 3.1.1 and we reject events which contain loose electrons  
232 in addition to the tight one. In this channel we are only interested in the decay to electron and  
233 jets, and we therefore reject events containing loose muons.

234 In the mu+jets channel, we select events that contain exactly one tight muon candidate whose  
235 criteria are described in Section 3.1.2 and we reject events which contain additional loose  
236 muons. In an analogous way to the e+jets channel, we reject events containing loose electrons.

## 237 3.3 Lepton reconstruction, selection and trigger efficiencies

Since lepton reconstruction, identification and trigger efficiencies can be slightly different between data and simulation, correction factors have to be applied to the MC to account for these differences. The efficiencies are calculated using a Tag and Probe technique exploiting Z boson decays to a pair of electrons or muons, respectively. The total lepton efficiency can be factorized into three components:

$$\epsilon_{\text{total}}(p_T, \eta) = \epsilon_{\text{Reco}}(p_T, \eta) \cdot \epsilon_{\text{Id}}(p_T, \eta) \cdot \epsilon_{\text{HLT}}(p_T, \eta) \quad (1)$$

$$\epsilon_{\text{Reco}}(p_T, \eta) = \frac{N_{\text{Reco}}^{\text{lep}}}{N_{\text{SC}}^{\text{lep}}} \quad \epsilon_{\text{Id}}(p_T, \eta) = \frac{N_{\text{Id}}^{\text{lep}}}{N_{\text{Reco}}^{\text{lep}}} \quad \epsilon_{\text{HLT}}(p_T, \eta) = \frac{N_{\text{HLT+Id}}^{\text{lep}}}{N_{\text{Id}}^{\text{lep}}} \quad (2)$$

238 all results are taken from POG or HEEP group studies.

### 239 3.3.1 Electron efficiencies

240 In the electron case, the reconstruction efficiency  $\epsilon_{\text{Reco}}$  characterizes the transition from a supercluster in the electromagnetic calorimeter to a reconstructed Particle Flow electron.  
241 The ability of a reconstructed electron to pass the offline selection, stated in Sec.3.1.1, consisting  
242 of several isolation and identification selection, is given by the identification efficiency  $\epsilon_{\text{Id}}$ .

---

<sup>6</sup> <https://twiki.cern.ch/twiki/bin/view/CMSPublic/WorkBookMetAnalysis>

Finally, the selected electron has a certain probability to fire the high level trigger and this efficiency to fulfill the HLT requirements, calculated respect to the offline selection, is parametrized as  $\epsilon_{\text{HLT}}$ . In data, a single electron trigger is used at HLT level, while in MC the trigger requirements are dropped. Since the HLT efficiency in MC is equal to 100%, the trigger efficiency measured on data is applied directly in the analysis of MC samples, while the other two efficiency components are calculated both for data and MC, so that a data/MC scale factor has to be applied.

As stated in Table 1, e+jets data are taken starting from SingleElectron datasets. Considering the whole dataset, the optimal trigger choice is represented by an un-prescaled single electron trigger with id requirements (no isolation selections) and lower  $p_T$  threshold, respect to the offline identification:

- `HLT_Ele80_CaloIdVT_TrkIdT*` → active during a subset of Run2012A.
- `HLT_Ele80_CaloIdVT_GsfTrkIdT*` → active during  $\sim 95\%$  of the data taking.

The efficiency of this trigger has been evaluated in the contest of the search for  $W' \rightarrow l\nu$  channel [14] and it is equal to  $\epsilon_{\text{HLT}} = 0.991$  for electrons in the EB ( $0 < |\eta| < 1.442$ ),  $\epsilon_{\text{HLT}} = 0.976$  for electron in EE ( $1.566 < |\eta| < 2.5$ ).

The electron HEEPID efficiencies have been measured by the HEEP group [15]; data/MC scale factors of  $\sim 0.98$  are used as event weights to correct the MC.

### 3.3.2 Muon efficiencies

In the muon case, the reconstruction efficiency  $\epsilon_{\text{Reco}}$  describes the ability to reconstruct a Particle Flow muon starting with a particle track and it can be assumed to be one [16]. The identification efficiency  $\epsilon_{\text{Id}}$  gives an estimate for a reconstructed muon to pass the offline selection criteria. It can be computed for both data and simulation, thus a scale factor being the ratio of the two efficiencies is derived.

The trigger efficiency  $\epsilon_{\text{HLT}}$  is the fraction of selected muons fulfilling the HLT requirements respect to the offline selection. Since the HLT requirement is dropped in the MC analysis, the efficiency computed on data is used directly to correct the MC event expectation.

As stated in Table 1, mu+jets data are taken starting from SingleMu datasets. Considering the whole dataset, the optimal trigger choice is represented by an un-prescaled single muon trigger with no isolation requirements and lower  $p_T$  threshold, respect to the offline identification:

- `HLT_Mu40_eta2p1*` → active during the whole data taking at 8 TeV.

The efficiency of this trigger has been evaluated in the contest of the search for  $W' \rightarrow l\nu$  channel [14] and it is equal to:  $\epsilon_{\text{HLT}} = 0.940$  for muons with  $0 < |\eta| < 0.9$ ,  $\epsilon_{\text{HLT}} = 0.843$  for  $0.9 < |\eta| < 1.2$  and  $\epsilon_{\text{HLT}} = 0.824$  for  $1.2 < |\eta| < 2.1$ .

The muon high- $p_T$  efficiencies have been measured by the muon POG; data/MC scale factors of  $\sim 0.99$  are used as event weights to correct the MC.

## 280 4 Identifying Merged W bosons

281 The most typical variables used in jet analyses are the jet direction and its transverse momentum ( $p_T$ ). In the past several years, many methods have been put forth for using the information beyond their direction and  $p_T$ , to perform searches for new physics at the LHC. By understanding the substructure of jets, we are able to identify jets originating from heavy objects such as  $W, Z$ , Higgs, or top quarks that have been produced with a significant Lorentz boost, such that their decay products are highly collimated into a single jet. Such substructure algorithms improve the separation over typical background jets produced in soft or hard QCD processes.

289 In this particular analysis, we are especially concerned with using jet substructure techniques  
290 for discriminating highly boosted  $W$  bosons decaying hadronically, where the decaying quarks  
291 are contained within one large radius jet (CA8), from background jets coming from QCD pro-  
292 cesses. The subject of using jet substructure for distinguishing  $W$ -jets from background is stud-  
293 ied alone in its own document [17].

294 In [18] and [17], we have performed in-depth studies of observables which give the best signal-  
295 to-background discrimination. The outcome of the study is as follows:

- 296 • The jet mass is the best discriminating variable for distinguishing between signal  
297 and background jets.
- 298 • Grooming the jet mass, in particular, gives improved discrimination power by sup-  
299 pressing background jet masses to zero while preserving the signal jet mass near the  
300  $W$  mass. The optimal grooming algorithm of the parameters studied is the pruning  
301 algorithm.
- 302 • In addition to the jet mass, we find that a rectangular cut on the N-subjettiness vari-  
303 able,  $\tau_2/\tau_1$ , provides the best discrimination power additionally with the pruned jet  
304 mass. The ROC curve is given in Fig. 1.

In pruning, the jet is re-clustered using all the particles belonging to the original CA8 jet, ignoring in each recombination step the softer “protojet” if the recombination is softer than a given threshold  $z_{\text{cut}} = 0.1$  or forms an angle  $\Delta R_{i,j}$  wider than  $D_{\text{cut}} = \alpha \times \frac{m}{p_T}$  with respect to the previous recombination step, where  $\alpha = 0.5$  and  $m$  and  $p_T$  are, respectively, the mass and the transverse momentum of the original jet. The hardness of the recombination  $z_{ij}$  is defined as:

$$z_{ij} = \frac{\min(p_{T,i}, p_{T,j})}{p_{T,(i+j)}} < z_{\text{cut}} \quad (3)$$

305 where  $p_{T,i}$  and  $p_{T,j}$  are the transverse momenta of the  $i$  and  $j$  protojets, while  $p_{T,(i+j)}$  is the  $p_T$   
306 of the combined jet.

N-subjettiness  $\tau_N$  was introduced in [19] and it is a generalized jet shape observable. For  $N$  subjets of a given jet, defined via the exclusive  $k_T$  algorithm, the N-subjettiness observables is defined as:

$$\tau_N = \frac{1}{d_0} \sum_k p_{T,k} \min\{\Delta R_{1,k}, \Delta R_{2,k}, \dots, \Delta R_{N,k}\} \quad (4)$$

307 where  $k$  runs over all constituent particles. The normalization factor is  $d_0 = \sum_k p_{T,k} R_0$ , where  
308  $R_0$  is the original jet radius. The  $\tau_N$  observable is, in effect, a way to quantify to a certain degree  
309 how much a jet is likely to be composed of  $N$  subjets. In fact, jets with  $\tau_N \approx 0$  have all their  
310 radiation aligned with the candidate subjet direction and therefore have  $N$  or fewer subjets;  
311 while jets with  $\tau_N > 0$  have a large fraction of their energy distributed away from the jet axis

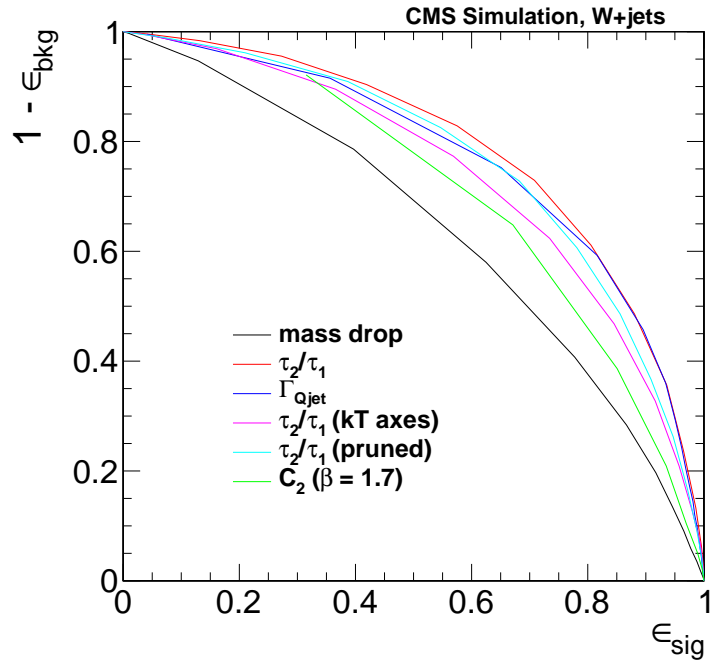


Figure 1: Comparison of jet substructure observable performance for W+jet events in the jet  $p_T$  bin, 250-350 GeV, for longitudinally polarized W-jet signal.

<sup>312</sup> and therefore have at least  $N + 1$  subjets. For this reason, jets coming from boosted Ws have  
<sup>313</sup> typically a lower value of  $\tau_N$  respect to a QCD jet. Finally, for better distinguish QCD jets  
<sup>314</sup> (typically 1 subjet) from a W-jet (typically 2 subjets), we use the observable  $\tau_2/\tau_1$ .

## 315 5 Analysis Strategy

316 In this section, we define basic analysis cuts and compare data vs Monte Carlo distributions in  
 317 the analysis phase space. The main observables are the pruned jet mass distribution,  $m_j$ , the  
 318 N-subjettiness,  $\tau_2/\tau_1$ , and the three-body mass,  $m_{l\nu j}$ .

### 319 5.1 Event Selection

320 The main goal of the kinematic cuts is to isolate a highly boosted topology which is consistent  
 321 with the WW semi-leptonic system. Once have asked the presence of only one tight lepton ( $e$   
 322 or  $\mu$ ) and no further loose leptons, as described in Sec. 3.2, the  $p_T$  of the leptonic W is required  
 323 to be greater than 200 GeV, as well as  $p_T$  of the hardest CA8 jet in the event. In addition,  
 324 the missing transverse energy should be greater than 40 GeV (80 GeV) for the muon (electron)  
 325 channel, in order to suppress the contribution to the analysis from QCD-like background (QCD  
 326 multijets and  $\gamma$ -jets).

327 Moreover, there are specific topological cuts which require that the W bosons are back-to-back:

- 328 • The distance between the lepton and the jet should be large,  $\Delta R_{l,j} > \pi/2$ ,
- 329 • The azimuthal distance between the missing energy and the jet should be large,  
 $\Delta\phi_{MET,j} > 2.0$ .
- 331 • The azimuthal distance between the leptonic W boson and the jet should be large,  
 $\Delta\phi_{V,j} > 2.0$ .

333 Finally, to further suppress the contamination from top backgrounds, namely  $t\bar{t}$  and single top,  
 334 the event is required to have no b-tagged AK5 jets, according to CSV medium working point.

335 Since the pruned jet mass of the two jet system, originated from W decay but reconstructed  
 336 as only one single jet due to the high Lorentz boost, exhibits a better discriminator power  
 337 between signal and background, as reported in Sec. 4, this variable is chosen as our main jet  
 338 mass observable for W-tagging. Looking at the pruned mass of the leading CA8 jet, selected as  
 339 our hadronic W candidate, three orthogonal region are defined:

- 340 • **Signal Region (SR)**  $\rightarrow 65 \text{ GeV} < m_j < 105 \text{ GeV}$ .
- 341 • **Low-Sideband Region (LSB)**:  $\rightarrow 40 \text{ GeV} < m_j < 65 \text{ GeV}$ .
- 342 • **High-Sideband Region (HSB)**:  $\rightarrow 105 \text{ GeV} < m_j < 130 \text{ GeV}$ .

343 The signal region window was not optimized precisely for this analysis, we based the cur-  
 344 rent definition on what was done in a previous analysis targeting lower  $X \rightarrow WW$  resonance  
 345 masses [20].

346 On the contrary, for reconstructing the WW resonance we still use the kinematic of the un-  
 347 groomed CA8 jet. This is why jet energy scale correction are not yet available at CMS for  
 348 pruned jets, so keeping the original jet we can use properly calibrated jets to describe the event  
 349 kinematics.

### 350 5.2 Data to MC comparison

351 Given the event selection from the previous section, we make comparisons of the data and  
 352 MC for various kinematic observables, taking the events falling in the low plus high sideband  
 353 regions ( $40 \text{ GeV} < m_{pr}^W < 65 \text{ GeV}$  and  $105 \text{ GeV} < m_{pr}^W < 130 \text{ GeV}$ ), where the contamination from  
 354 the graviton signal is expected to be small.

355 It can been seen that the dominant background contribution comes from the W+jets production,

356 with sub-leading contributions from the  $t\bar{t}$  SM process and even smaller events from WW/WZ,  
 357 single top quark production and DY+jets.

358 All the backgrounds, except the W+jets, are normalized to their expected cross section values,  
 359 reported in Table 3. Instead, the W+jets cross section listed in Table 3 is corrected by a factor  
 360 1.342 (1.336) for muon (electron) final state, such that the total integral of the MC matches  
 361 the number of events seen in data in the low+high sideband region. This lack of W+jets in  
 362 the sideband control region is due to a mis-model of the jet pruned mass between data and  
 363 MC; pruned mass for QCD jets is particularly sensitive to the parton shower model and its  
 364 tune, thus it tends to assume smaller values in the simulation than in data, as proved in [17].  
 365 However, this does not represents a problem in the presented analysis, since the normalization,  
 366 as well as the shape, of the W+jets background in the signal region are data driven estimated,  
 367 as described is Sec. 5.4.

368 In the following control plots, the `WJetsToLNu_PtW-100_TuneZ2star_8TeV-madgraph` sam-  
 369 ple has been considered for the W+jets; various distribution are shown both for muon and  
 370 electron channel:

- 371 • In Fig. 2, the lepton  $p_T$  and  $\eta$ .
- 372 • In Fig. 3, the missing transverse energy  $E_T^{\text{miss}}$  and the number of reconstructed ver-  
 373 texes after MC re-weight, as described in [21].
- 374 • In Fig. 4, the leptonic W transverse momentum  $p_T^W$  and its transverse mass  $m_T^W$ .
- 375 • In Fig. 5, the hadronic W  $p_T$  and  $\eta$ .
- 376 • In Fig. 6, the hadronic W pruned mass  $m_j$  and the N-subjettiness  $\tau_2/\tau_1$ .
- 377 • In Fig. 7, the three body invariant mass  $m_{WW} = m_{l\nu j}$ .

378 The agreement between data and simulation is not perfect, although the main kinematic fea-  
 379 tures of these events in data are correctly described by the MC.

380 The agreement between data and MC is improved for events with real Ws decaying to hadrons,  
 381 as discussed in Sec 5.3 for the  $t\bar{t}$  control sample.

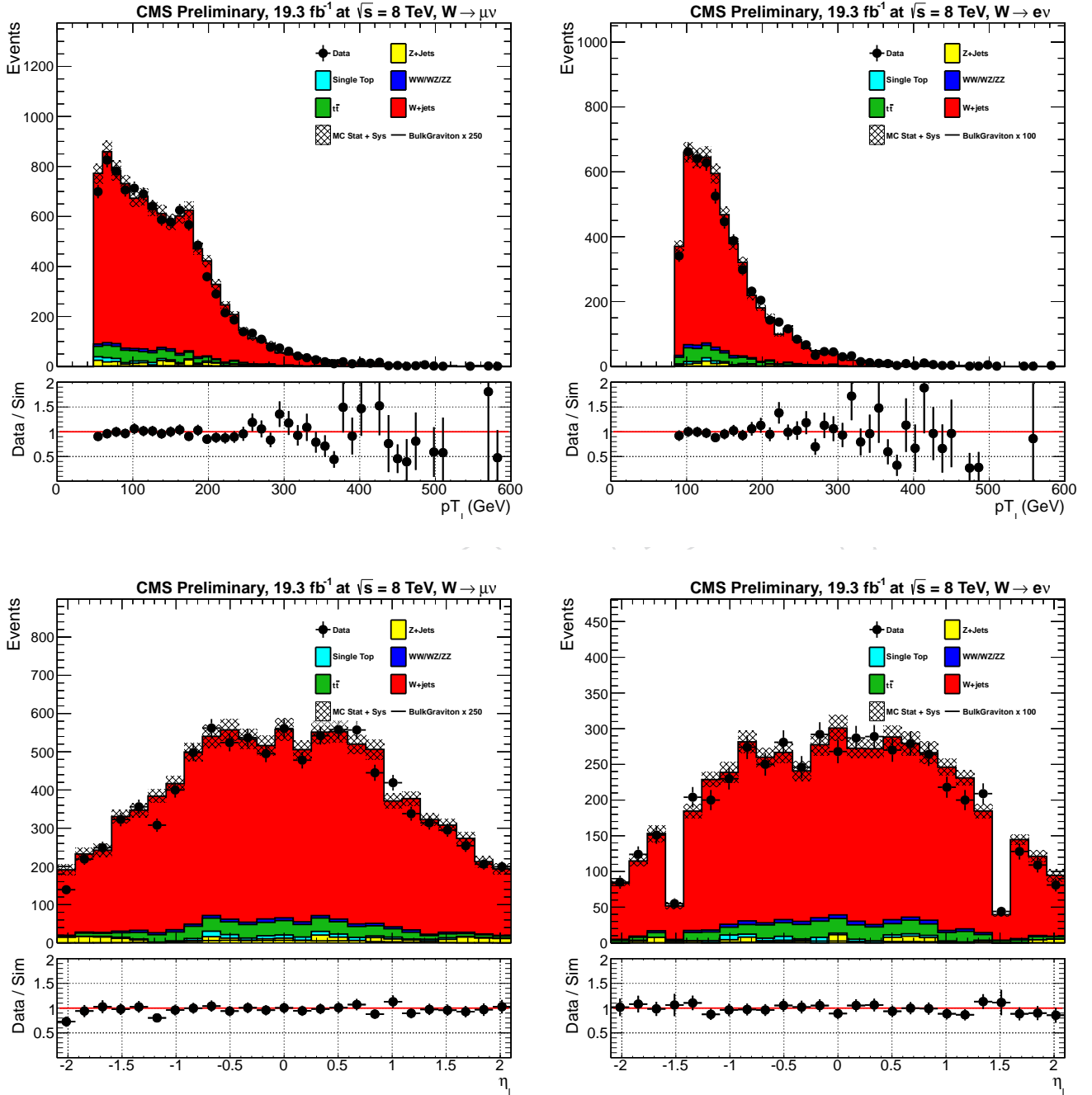


Figure 2: Lepton  $p_T$  and  $\eta$  for muon channel (left) and electron channel (right) for events in the pruned mass sidebands.

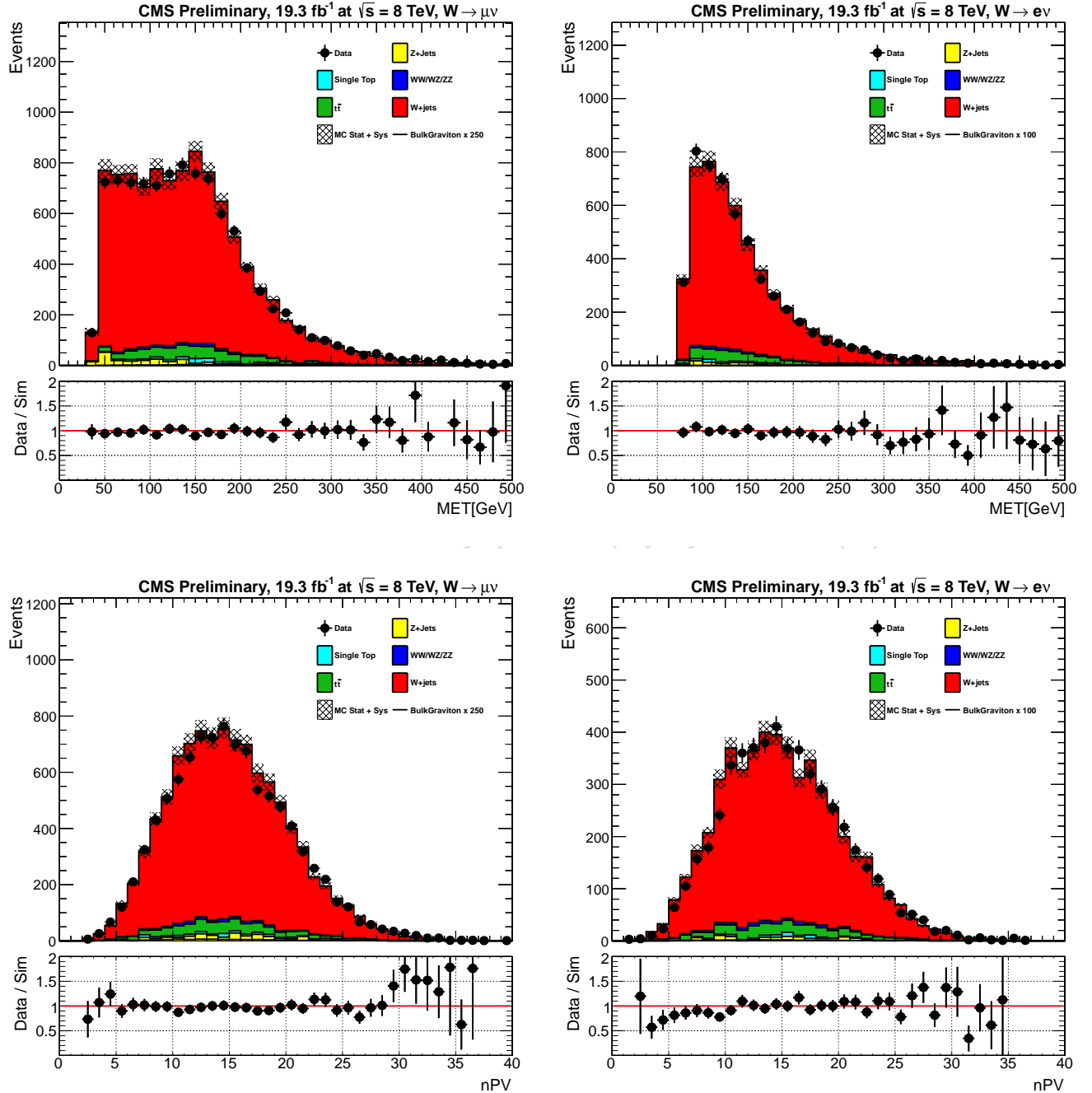


Figure 3:  $E_T^{\text{miss}}$  and  $N_{\text{PV}}$  for muon channel (left) and electron channel (right) for events in the pruned mass sidebands.

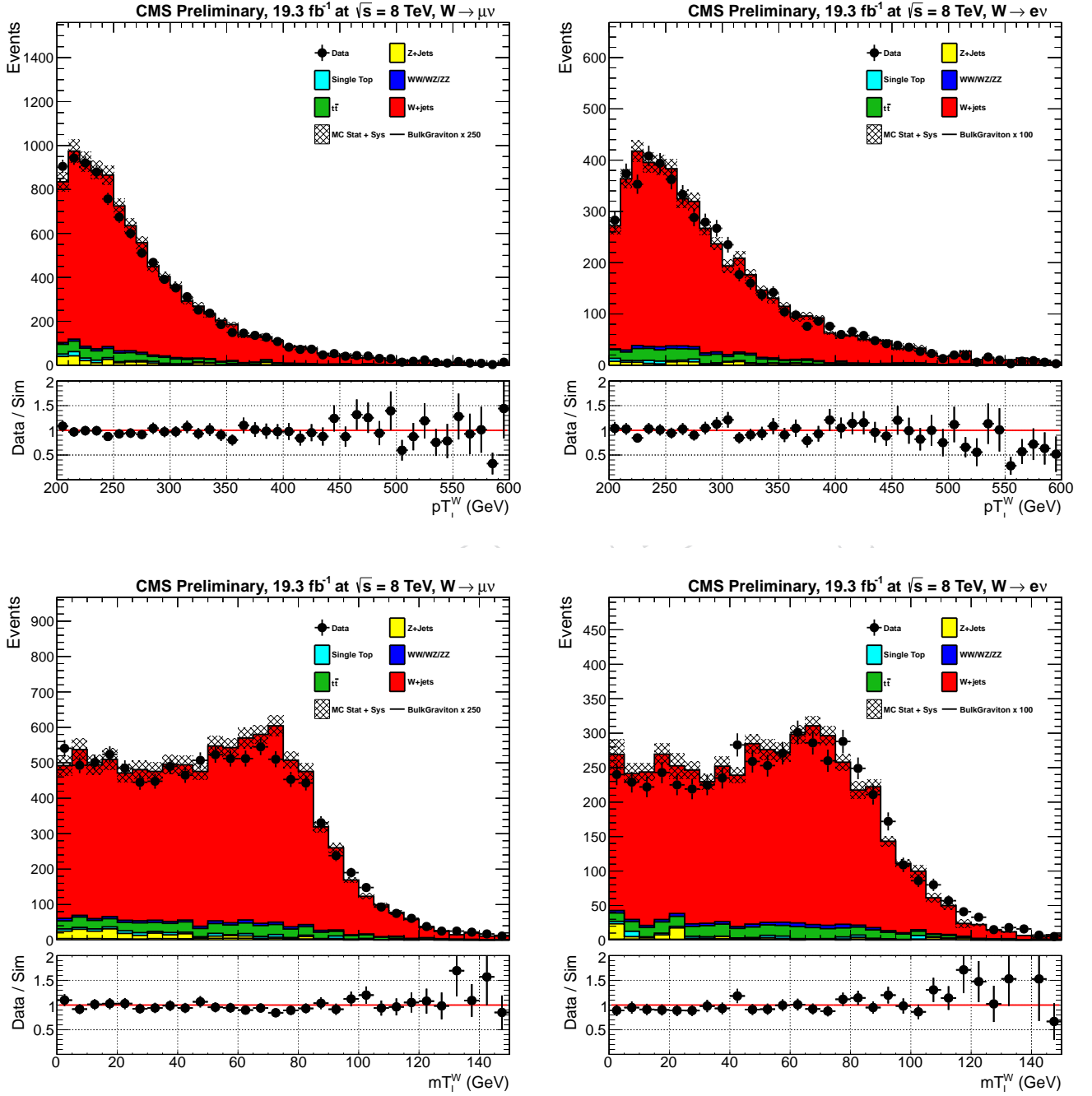


Figure 4: Leptonic  $W$   $p_T^W$  and its transverse mass  $m_T^W$  for muon channel (left) and electron channel (right) for events in the pruned mass sidebands.

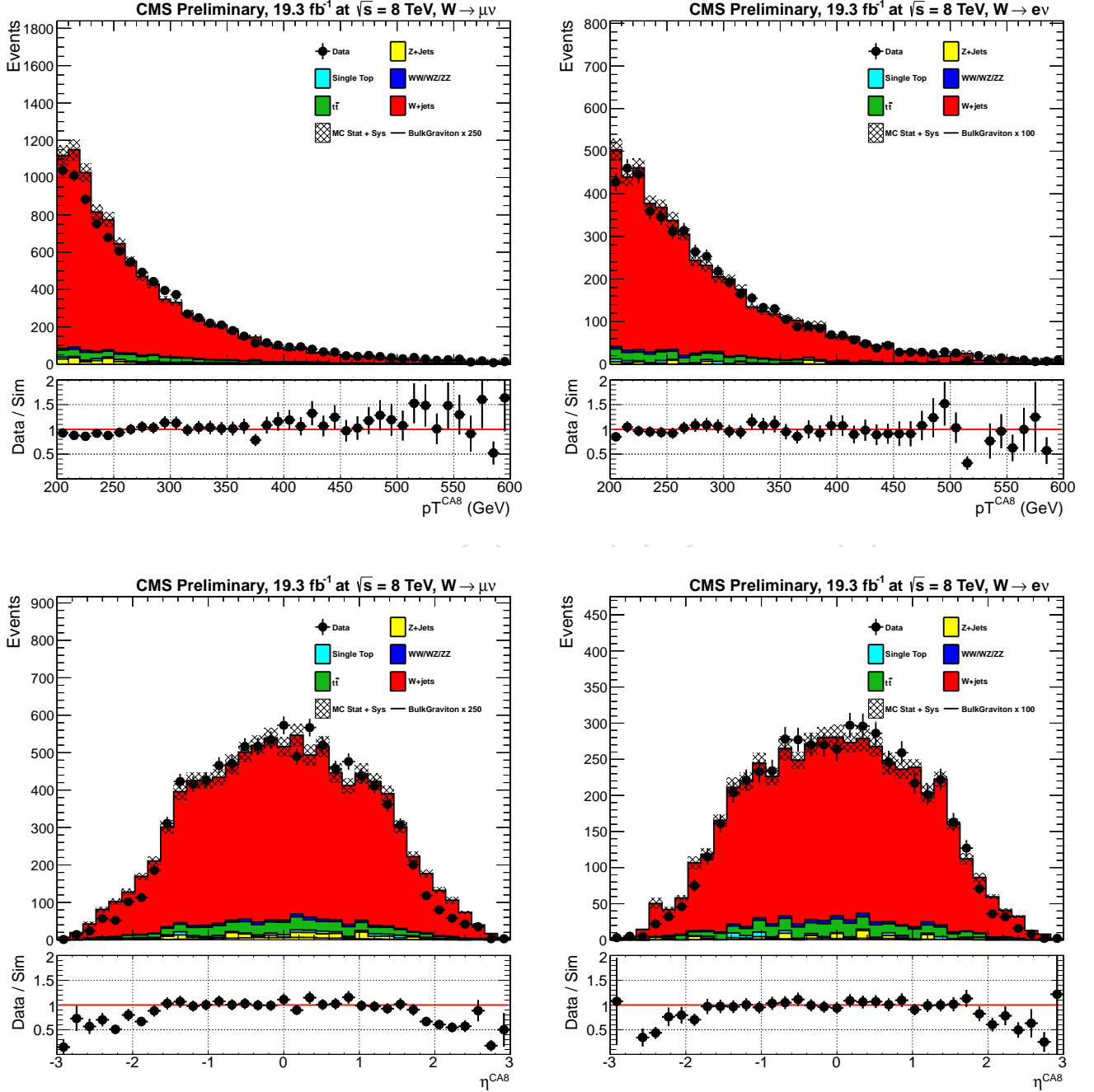


Figure 5: Hadronic  $W$   $p_T^W$  and  $\eta$  for muon channel (left) and electron channel (right) for events in the pruned mass sidebands.

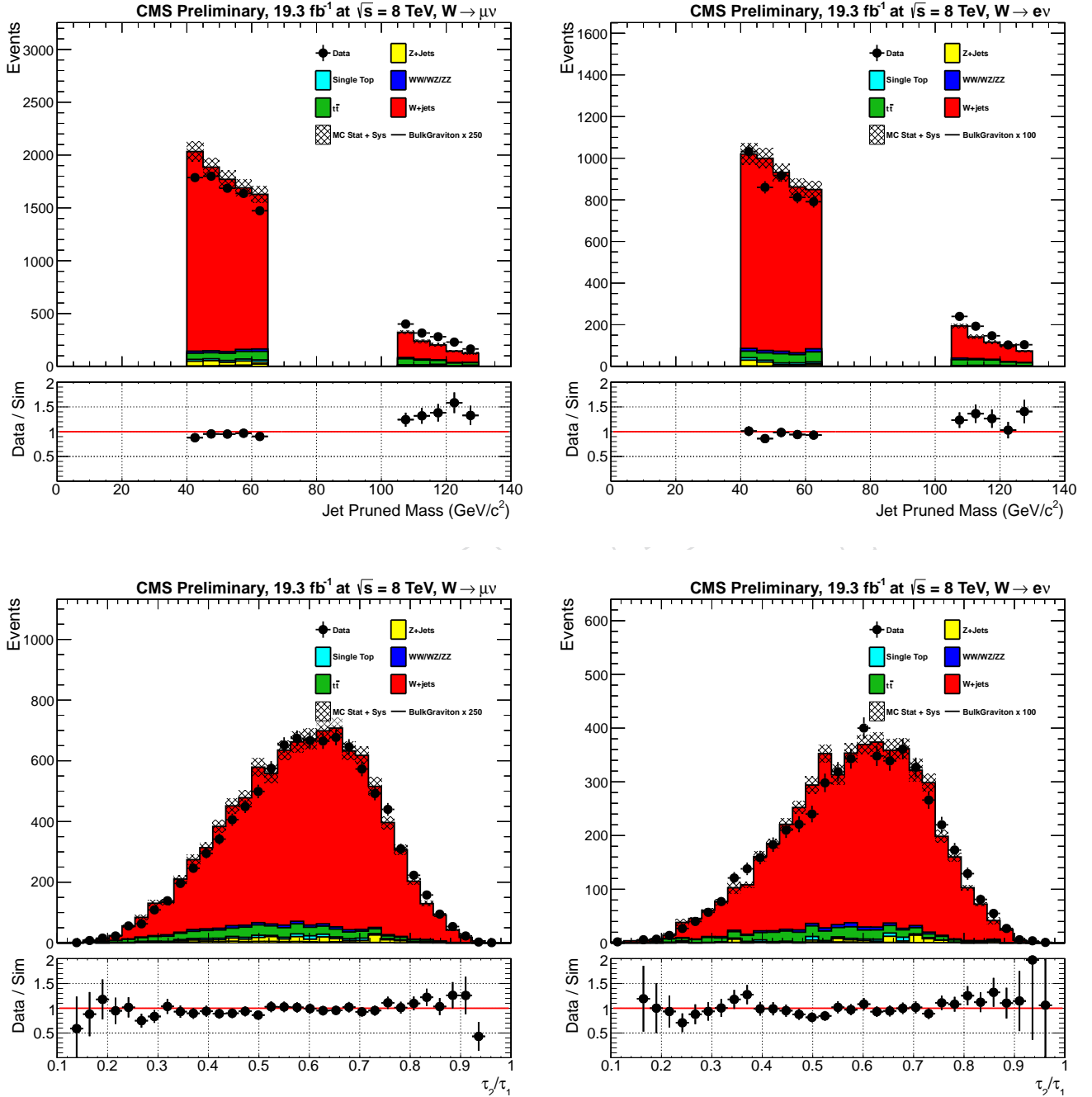


Figure 6: Hadronic  $W$  pruned mass  $m_{pr}^W$  and  $\tau_2/\tau_1$  for muon channel (left) and electron channel (right) for events in the pruned mass sidebands.

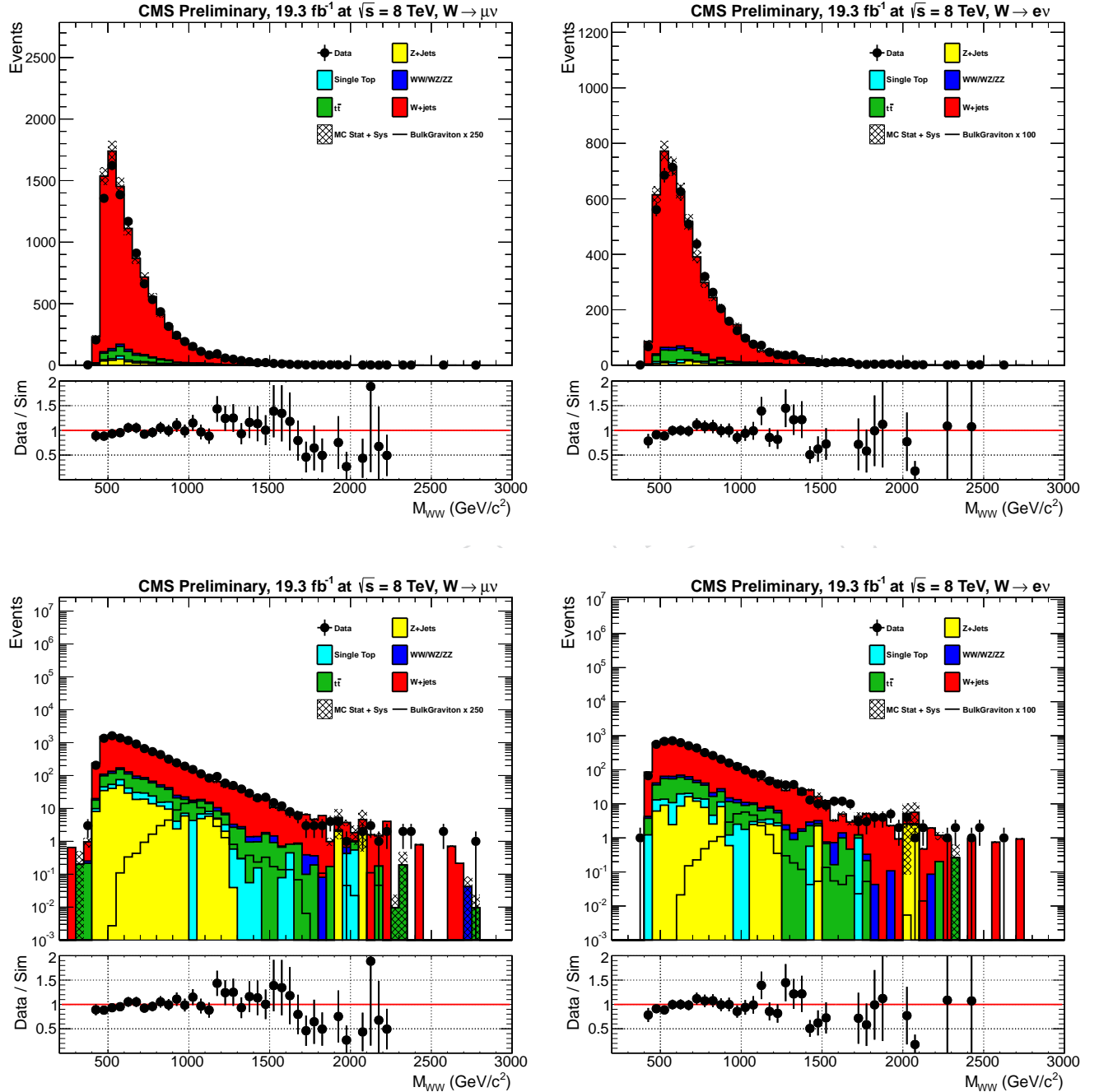


Figure 7: Hadronic  $W$   $p_T^W$  and  $\eta$  for muon channel (left) and electron channel (right) for events in the pruned mass sidebands.

382 **5.3 Control Region,  $t\bar{t}$**

383 To understand the performance of groomed and substructure variables on merged W bosons,  
 384 a control sample of pure hadronic W's can be isolated in data, looking at the high pT  $t\bar{t}$  sample.

385 **5.3.1 Control plots in  $t\bar{t}$  control sample**

386 To select this control sample, we use the standard kinematic pre-selections described in Sec. 5.1,  
 387 but changing the requirement on the number of b-tagged AK5 jets: looking at the AK5 recon-  
 388 structed jets, outside of the CA8 jet cone, it is required at least one CSV "medium" AK5 b-jet.  
 389 To boost statistics, we choose the CA8 jet in the opposite hemisphere of the lepton, with the  
 390 highest mass and a  $p_T^{CA8} > 200$  GeV. This is different from the standard selection, which uses  
 391 the highest  $p_T$  CA8 jet in the event, with a minimum  $p_T$  threshold at 200 GeV.

392 Making these cuts, we have a nearly pure sample of  $t\bar{t}$  events, with a small contamination from  
 393 single top, W+jets and VV events. The jet mass, jet  $p_T$ ,  $m_{l\nu J}$ , and  $\tau_2/\tau_1$  variables are shown  
 394 in Fig. 8 for muon channel and Fig. 9 for electron one. These plots include systematic and  
 395 statistical uncertainties on the Monte Carlo prediction, where the systematics come from the  
 396 normalization uncertainty on the VV, single Top and W+jets cross-section. These are taken to  
 397 conservatively be 30%, as quoted by the VHbb analysis [22].

398 Since we know that  $\tau_2/\tau_1$  is the best variable for discriminating W-jet signal from QCD jet  
 399 background (see ROC curve reported in Fig.1), the N-subjettiness selection has been optimized  
 400 in the analysis region, in different CA8 jet  $p_T$  bins for events falling inside jet mass window  
 401  $m_j \in [65, 105]$  GeV, by means of the optimization metric:  $\sigma = \epsilon_S / \sqrt{\epsilon_B}$ . This selection is applied  
 402 on top of the kinematic selections described in Sec. 5.1 and is applied for all further analysis.  
 403 For this reason, the last four plots in Fig. 8 and Fig. 9 are plotted after a cut on  $\tau_2/\tau_1 < 0.5$ .

404 **5.3.2 Background scale factors and mass scale/resolution uncertainties**

405 The  $t\bar{t}$  control sample is used to extract data/MC scale factors for non-dominant background  
 406 contributions:  $t\bar{t}$ , single top, WW/WZ as well as for the signal.

407 For the  $t\bar{t}$  and single top contributions, we compute a scale factor based on the difference be-  
 408 tween data and MC expectation in the signal region of the control sample. On the contrary,  
 409 for the WW/WZ and signal contributions, we are only concerned with the efficiency for pure  
 410 W-jet signal, so it is necessary to subtract background contributions to get the correct signal  
 411 efficiency scale factor.

412 For the  $t\bar{t}$  and single top contributions, we apply all the cuts used to define the  $t\bar{t}$  control region,  
 413 stated in Sec. 5.3.1. Then, looking only inside the jet mass signal region ( $m_J \in [65-105]$  GeV) and  
 414 applying the N-subjettiness  $\tau_2/\tau_1$  selection, we account for the difference after the  $\tau_2/\tau_1$  cut, to  
 415 get the data/MC scale factor for both low purity ( $\tau_2/\tau_1 \in [0.5, 0.75]$ ) and high purity category  
 416 ( $\tau_2/\tau_1 < 0.5$ ). Results are listed given in Table 4; these scale factors are applied to normalize  
 the  $t\bar{t}$  and single top expectation in the analysis signal region.

Signal window	$\mu$ SF High Purity	$e$ SF High Purity	$\mu$ SF low Purity	$e$ SF Low Purity
65-105 GeV	$0.986 \pm 0.034$	$0.968 \pm 0.059$	$1.238 \pm 0.060$	$1.321 \pm 0.082$
70-100 GeV	$0.978 \pm 0.037$	$0.981 \pm 0.049$	$1.236 \pm 0.067$	$1.337 \pm 0.094$

Table 4:  $t\bar{t}$  and single top data/MC scale factor "SF" for both muon and electron channel, low  
 purity and high purity category.

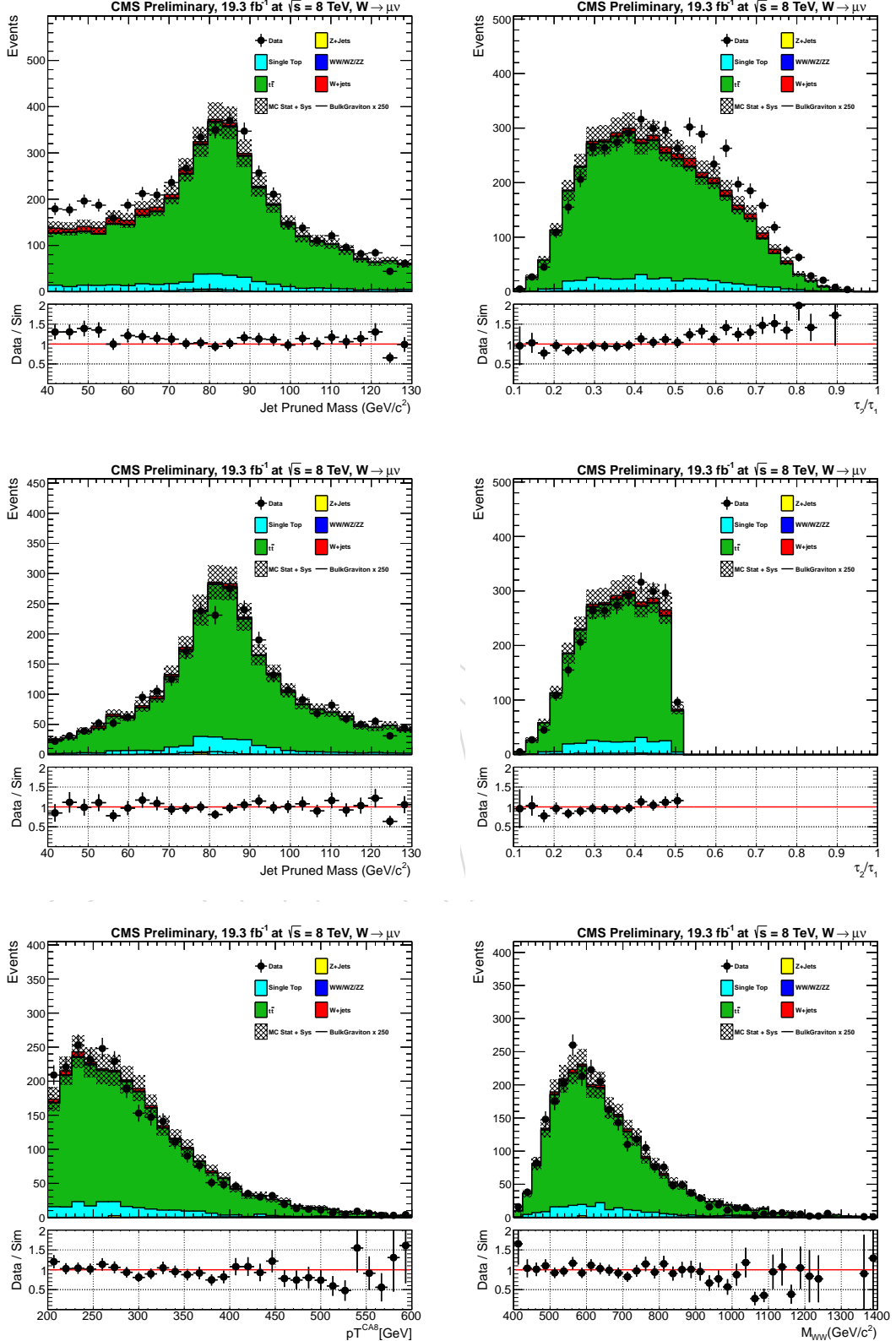


Figure 8: Distributions in the  $t\bar{t}$  control sample for muon+jet final state. The top two plots are before making any cut on  $\tau_2/\tau_1$ , while the remaining ones are after  $\tau_2/\tau_1 < 0.5$ .

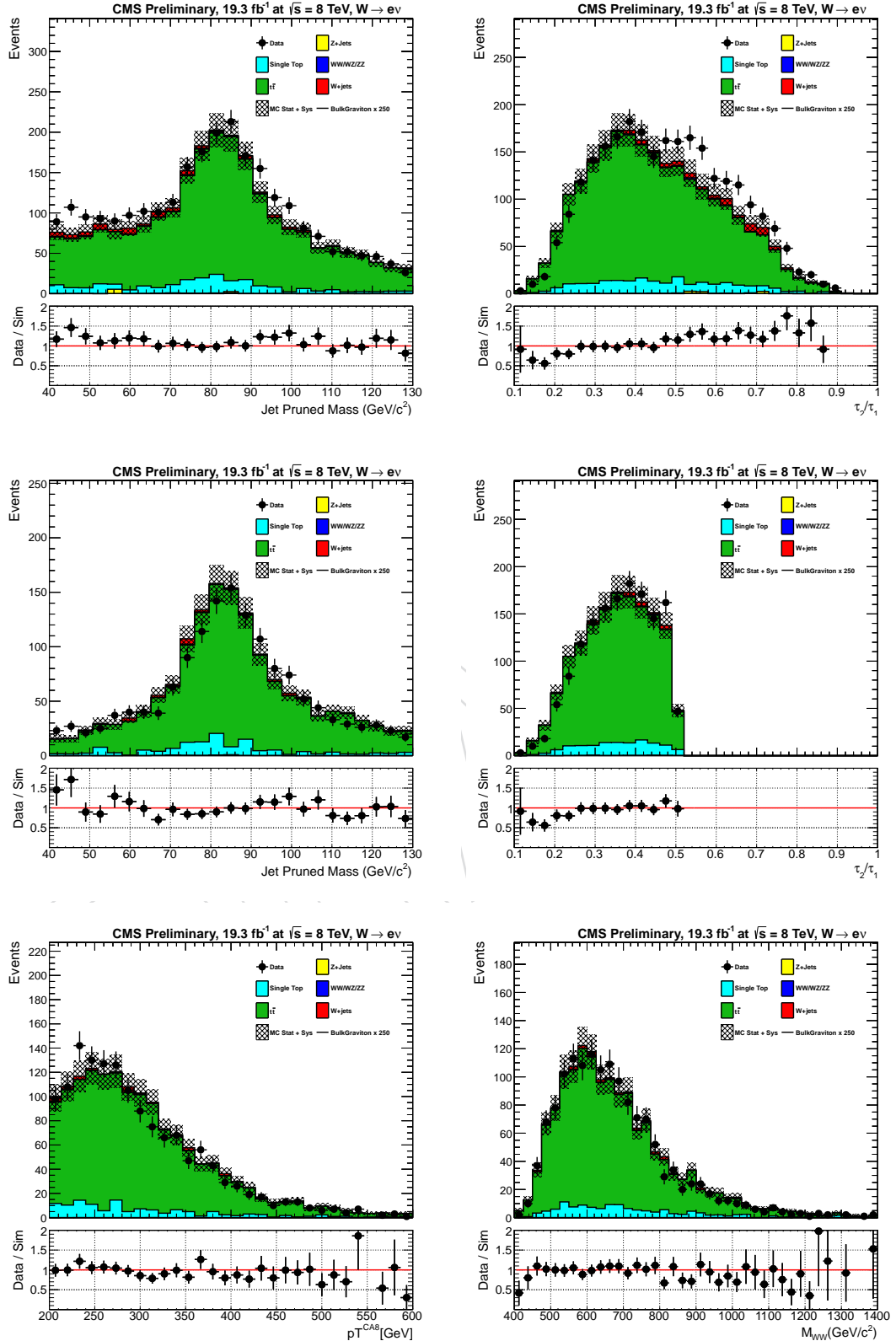


Figure 9: Distributions in the  $t\bar{t}$  control sample for electron+jet final state. The top two plots are before making any cut on  $\tau_2/\tau_1$ , while the remaining ones are after  $\tau_2/\tau_1 < 0.5$ .

For the WW/WZ and signal contributions, we are only concerned with the data/MC scale factor for the *pure* W-jet tagging efficiency. In order to understand the part of the  $t\bar{t}$  jet mass distribution which contains "real" merged W's and pure combinatorial background, we use the  $t\bar{t}$  MC sample. By matching the CA8 jet with the hadronic W at generator level, in a cone of  $\Delta R < 0.3$ , we can get the "real" merged W's (matched) and pure combinatorial background (unmatched) shapes. These plots from  $t\bar{t}$  MC are shown in Fig. 10 for the matched (upper line) and unmatched (bottom line) samples that passed (left column) and failed (right column) the N-subjettiness selection  $\tau_2/\tau_1 < 0.5$ . The chosen functional forms are:

- $f_{\text{bkg}}(m_j) = F_{\text{ExpErf}} = e^{c_0 m_j} \cdot \frac{1 + \text{Erf}((m_j - a)/b)}{2}$  for the unmatched-passed and unmatched-failed sample (second line plots in Fig. 10);
- $f_{\text{pass}}^{\text{sig}}(m_j) = F_{\text{2Gaus}}(m_j) = c_0 \cdot e^{-(m_j - m_{j0})^2/2\sigma_0^2} + c_1 \cdot e^{-(m_j - m_{j1})^2/2\sigma_1^2}$  for the matched-passed sample.
- $f_{\text{fail}}^{\text{sig}}(m_j) = F_{\text{Gaus}}(m_j) + F_{\text{Chebychev}}^{II}(m_j)$  for the matched-failed sample.

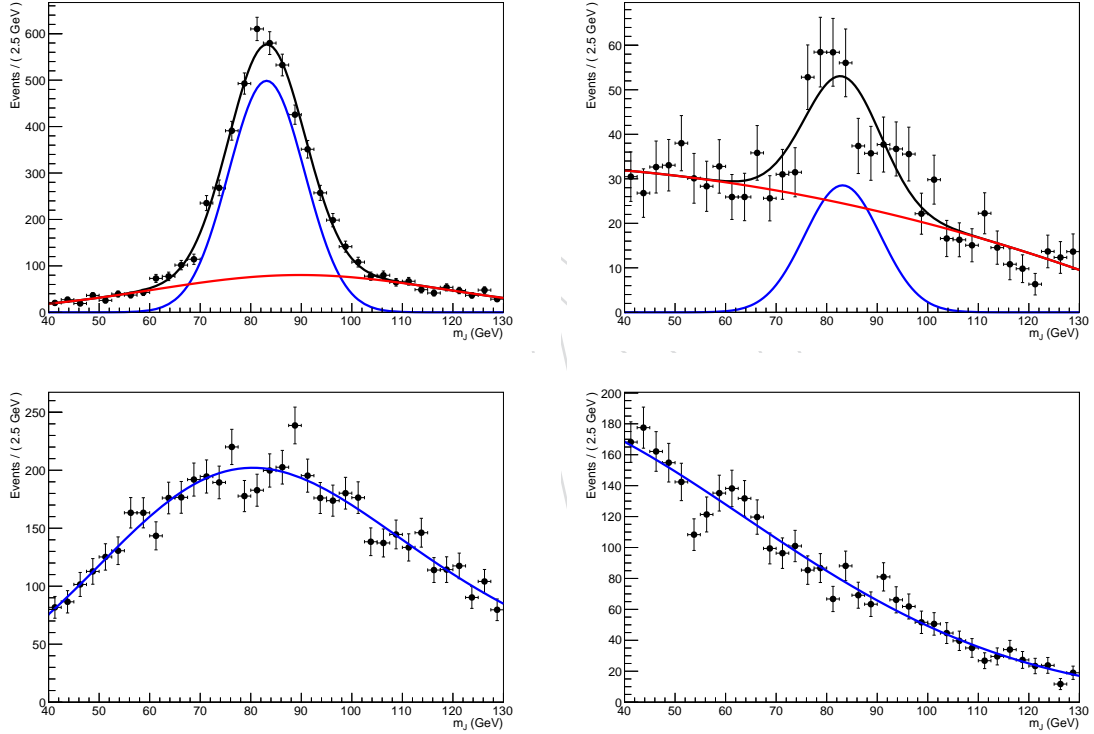


Figure 10: Matched (top) and unmatched (bottom) samples for  $t\bar{t}$  MC in  $t\bar{t}$  control region: pass (left) and fail (right) the cut on  $\tau_2/\tau_1 < 0.5$ .

The W-tagger scale factors ( $SF_{HP}$ ), for the high purity selection ( $\tau_2/\tau_1 < 0.5$ ), are extracted estimating the cut efficiency on both data and MC fitting, simultaneously, "pass" and "fail" samples:

$$L_{\text{pass}} = \prod_i^{N_{\text{evt}}^{\text{pass}}} [N_W \cdot \epsilon_{HP} \cdot f_{\text{pass}}^{\text{sig}}(m_j) + N_2 \cdot f_{\text{pass}}^{\text{bkg}}(m_j) + N_{\text{pass}}^{\text{sTop}} \cdot f_{\text{pass}}^{\text{sTop}} + N_{\text{pass}}^{\text{VV}} \cdot f_{\text{pass}}^{\text{VV}} + N_{\text{pass}}^{\text{wjet}} \cdot f_{\text{pass}}^{\text{wjet}}] \quad (5)$$

$$L_{\text{fail}} = \prod_i^{N_{\text{evt}}^{\text{fail}}} [N_W \cdot (1 - \epsilon_{HP}) \cdot f_{\text{fail}}^{\text{sig}}(m_j) + N_3 \cdot f_{\text{fail}}^{\text{bkg}}(m_j) + N_{\text{fail}}^{\text{sTop}} \cdot f_{\text{fail}}^{\text{sTop}} + N_{\text{fail}}^{\text{VV}} \cdot f_{\text{fail}}^{\text{VV}} + N_{\text{fail}}^{\text{wjet}} \cdot f_{\text{fail}}^{\text{wjet}}] \quad (6)$$

$$SF_{HP} = \frac{\epsilon_{HP}(dat)}{\epsilon_{HP}(sim)} \quad (7)$$

431 The difference between data and MC efficiencies are taken as the W-tagging scale factor. Fit  
 432 results are shown in Fig. 11, where the fitting functions are motivated by the shapes shown in  
 433 Fig. 10 and, considering the fitting robustness, we fix some of the parameters in the shapes,  
 434 such as the area ratio of the double Gaussian in  $f_{pass}^{\text{sig}}$ .

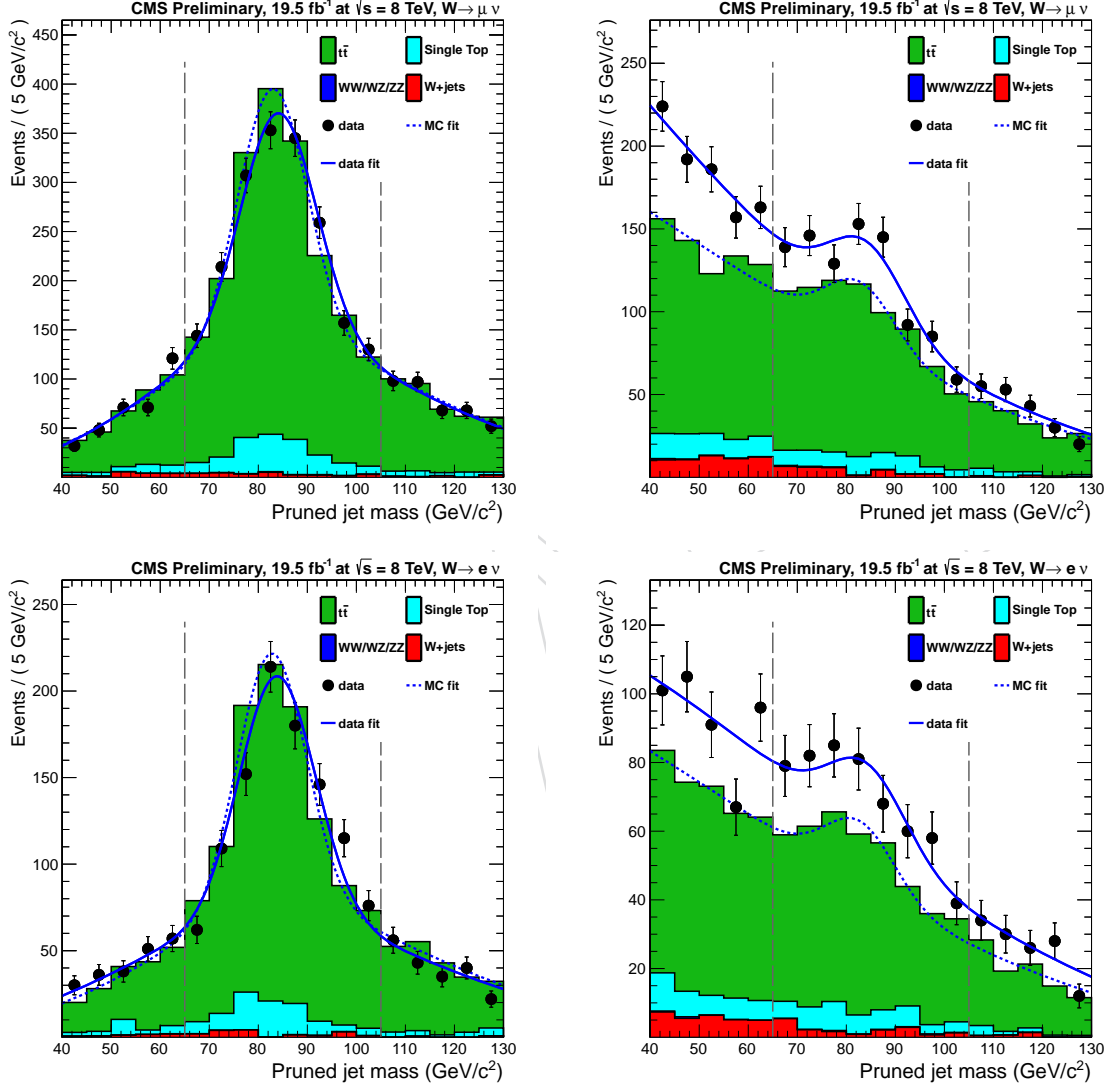


Figure 11: Pruned jet mass distribution in the  $t\bar{t}$  control sample passing(left) and failing (right) the high purity W-tag cut. Upper line the muon channel fits, bottom line the electron ones.

435 The scale factors for electrons and muons, taking into account the high purity working point,  
 436 are computed to be:

$$\begin{cases} \epsilon(dat, \mu) = 0.637 \pm 0.049 \\ \epsilon(sim, \mu) = 0.715 \pm 0.049 \end{cases} \Rightarrow SF_{HP}(\mu) = 0.891 \pm 0.092 \quad (8)$$

$$\begin{cases} \epsilon(dat, el) = 0.693 \pm 0.069 \\ \epsilon(sim, el) = 0.740 \pm 0.066 \end{cases} \Rightarrow SF_{HP}(el) = 0.937 \pm 0.125 \quad (9)$$

In addition, again from the simultaneous fit of the likelihoods defined by Eq. 5 and Eq. 6, we can extract also the number of real W-jets in  $t\bar{t}$  events ( $N_W$ ), the number of combinatorial background events passing ( $N_2$ ) and failing ( $N_3$ ) the  $\tau_2/\tau_1$  selection:

$$\begin{aligned} \begin{cases} N_W(sim, \mu) = 1696 \pm 171 \\ N_W(sim, el) = 937 \pm 111 \end{cases} & \quad \begin{cases} N_W(dat, \mu) = 1867 \pm 208 \\ N_W(dat, el) = 1039 \pm 137 \end{cases} \\ \begin{cases} N_2(sim, \mu) = 1152 \pm 107 \\ N_2(sim, el) = 625 \pm 69 \end{cases} & \quad \begin{cases} N_2(dat, \mu) = 1162 \pm 133 \\ N_2(dat, el) = 588 \pm 74 \end{cases} \\ \begin{cases} N_3(MC, \mu) = 894 \pm 119 \\ N_3(MC, el) = 487 \pm 85 \end{cases} & \quad \begin{cases} N_3(Data, \mu) = 1162 \pm 133 \\ N_3(Data, el) = 687 \pm 107 \end{cases} \end{aligned}$$

Considering that, both for data and MC,  $\epsilon_{HP} + \epsilon_{LP} + \epsilon_{fail} = 1$ , the scale factor for low purity category can be defined as:

$$SF_{LP} = \frac{1 - \epsilon_{HP}(data) - \epsilon_{fail}(data)}{1 - \epsilon_{HP}(MC) - \epsilon_{fail}(MC)} \quad (10)$$

<sup>437</sup> where, fitting the failing samples ( $\tau_2/\tau_1 > 0.75$ ) with a pdf given by the sum of two exponential,  
<sup>438</sup> one for the fail-matched sample and another for the fail-unmatched one, we get:

$$\begin{cases} \epsilon_{fail}(dat, \mu) = 0.010 \pm 0.050 \\ \epsilon_{fail}(sim, \mu) = 0.008 \pm 0.037 \end{cases} \quad \begin{cases} \epsilon_{fail}(dat, el) = 0.055 \pm 0.052 \\ \epsilon_{fail}(sim, el) = 0.026 \pm 0.037 \end{cases} \quad (11)$$

<sup>439</sup> In Fig. 12, the  $t\bar{t}$  MC distribution for fail-matched and fail-unmatched samples are shown while,  
<sup>440</sup> in Fig.13, the final muon and electron channel fits are shown for both data and MC in the fail  
<sup>441</sup> sample (events with  $\tau_2/\tau_1 > 0.75$ ).

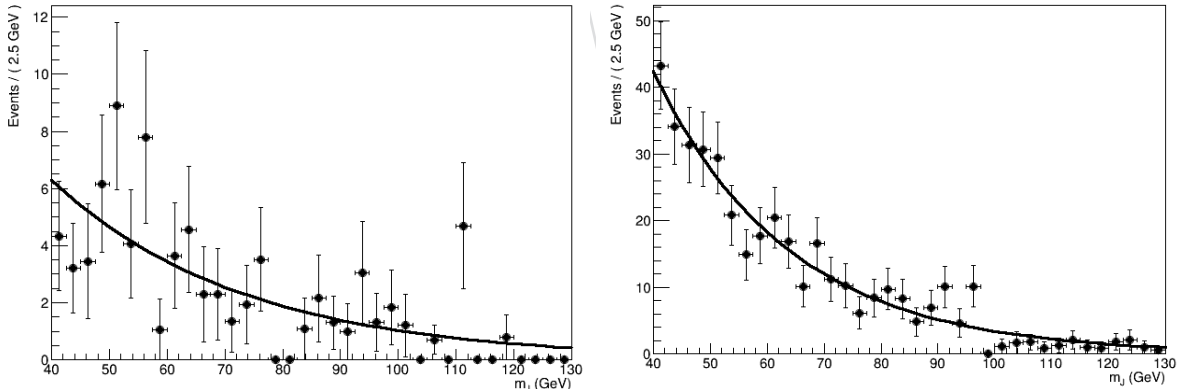


Figure 12: Matched (left) and unmatched (right) events in  $t\bar{t}$  simulation in the control region failing the N-subjettiness selection  $\tau_2/\tau_1 < 0.75$ .

<sup>442</sup> Finally, thanks to Eq. 10, the LP scale factors can be extracted:

$$\begin{cases} \epsilon_{LP}(data, \mu) = 0.352 \pm 0.072 \\ \epsilon_{LP}(MC, \mu) = 0.276 \pm 0.061 \end{cases} \Rightarrow SF_{LP}(\mu) = 1.275 \pm 0.506 \quad (12)$$

$$\begin{cases} \epsilon_{LP}(data, el) = 0.251 \pm 0.086 \\ \epsilon_{LP}(MC, el) = 0.234 \pm 0.076 \end{cases} \Rightarrow SF_{LP}(el) = 1.077 \pm 0.506 \quad (13)$$

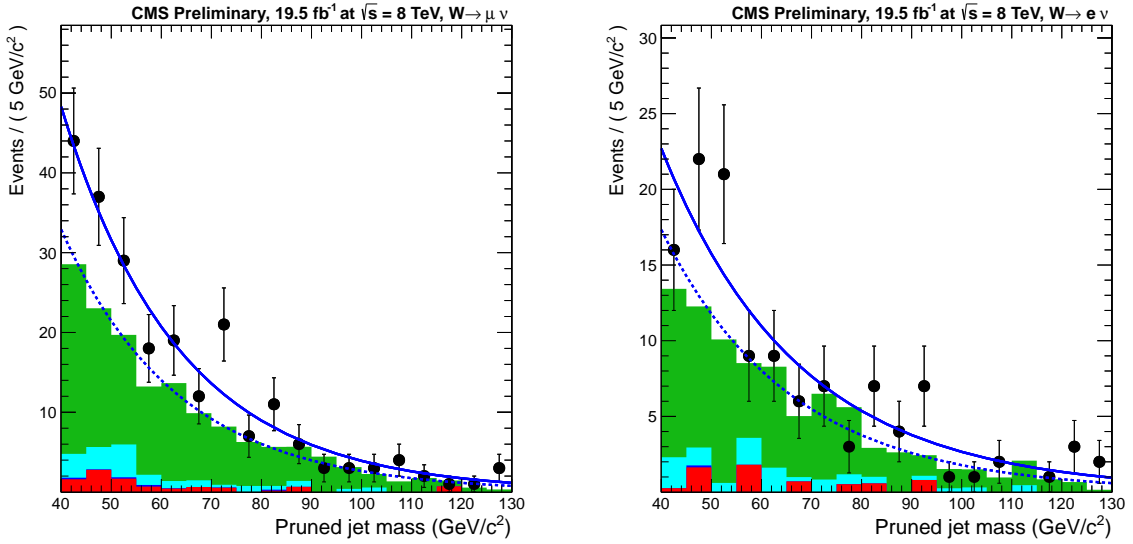


Figure 13: Muon (left) and electron (right) channel final fits in the failing region ( $\tau_2/\tau_1 > 0.75$ ): Monte Carlo result (blue dashed line) and data one (blue solid line).

443 To extract the jet mass scale and resolution correction, we use the mean and sigma value of the  
 444 narrower Gaussian in  $f_{\text{pass}}^{\text{sig}}(x)$ . Since we do not expect that the jet mass scale and resolution  
 445 should differ between electron and muon channels, we fit the muon and electron data simulta-  
 446 neously, constraining the mean and sigma of the narrower Gaussian the be the same between  
 447 electron and muon channels during fitting.  
 448 The extracted  $W$  mass peak position and resolution are:

$$\langle m \rangle_{\text{sim}} = 82.9 \pm 0.3 \text{ GeV}, \sigma_{\text{sim}} = 7.1 \pm 0.4 \text{ GeV} \quad (14)$$

$$\langle m \rangle_{\text{dat}} = 84.3 \pm 0.4 \text{ GeV}, \sigma_{\text{dat}} = 7.8 \pm 0.6 \text{ GeV} \quad (15)$$

449 We find that both the  $W$ -jet mass scale and resolution in data are greater than the one coming  
 450 from the simulation. We will shift the MC mean by +1.4 GeV and enlarge the MC sigma by  
 451 10.5% in the analysis (Sec. 5.4) to correct for this observed difference between data and MC.

## 452 5.4 W+Jets Background Extraction, Sideband $\alpha$ procedure

453 The basic strategy for estimating W+jets background contribution is to use a data-driven side-  
 454 band method to extract both its shape and normalization. This choice is motivated by the  
 455 disagreement in the jet mass distribution between the data and simulation, as proved in [23].  
 456 Non-dominant background contributions will be estimated from MC, with data-to-MC correc-  
 457 tions applied for mass scale, mass resolution and normalization, as described in Sec. 5.3.

458 In the sideband  $\alpha$  procedure, which is used to determine the W+jets  $m_{lvj}$  shape and normal-  
 459 ization in the signal region, data from a sideband region are used to extract the shape of the  
 460 distribution of interest, while correlations, needed to extrapolate from sideband to signal re-  
 461 gion, are taken from the simulation. In the below procedure, the sideband and signal regions,  
 462 for the three-body distribution  $m_{lvj}$ , are defined in the jet mass distribution ( $m_j$ ), as stated in  
 463 Sec. 5.1.

The shape for the W+jets contribution in the mass of the  $l + \nu + j$  system ( $m_{lvj}$ ) is derived as:

$$F_{\text{data,SR}}(m_{lvj}) = \alpha_{\text{MC}}(m_{lvj}) \times F_{\text{data,LSB}}(m_{lvj}) \quad (16)$$

where

$$\alpha_{\text{MC}}(m_{lvj}) = \frac{F_{\text{MC,SR}}(m_{lvj})}{F_{\text{MC,LSB}}(m_{lvj})}$$

464 Here, LSB refers to the low sideband region, while SR refers to the signal region; LSB is defined  
 465 as the pruned jet mass,  $m_J = [40-65]$  GeV, while SR region is defined as the pruned jet mass,  $m_J$   
 466 = [65-105] GeV. The upper sideband HSB,  $m_J = [105-130]$  GeV, is not used to extract the W+jet  
 467 shape for mainly two reasons:

- 468 • The W+jet  $m_{lvj}$  shapes are different between LSB and HSB region, in particular when  
 469 event with  $m_{lvj} \in [0.4-1.3]$  TeV are considered. Thus, despite a loss of statistics, the  
 470 modelling of the  $m_{lvj}$  distribution to extract  $\alpha$  is easier considering only in the LSB.
- 471 • Since the upper sideband you can have contribution from resonances decaying into  
 472 HW/HZ, this has to be discarded not to introduce a bias in the shape extrapolation.

473 Thus, in order to fully understand the W+jets contribution, we need three components:

- 474 • W+jets normalization in the signal region, which is derived fitting data in the side-  
 475 band of  $m_j$ .
- 476 •  $\alpha_{\text{MC}}(m_{lvj})$
- 477 •  $F_{\text{data,LSB}}(m_{lvj})$

478 A number of different functions are used both for the continuous  $m_j$  and  $m_{lvj}$  shapes. A default  
 479 shape is chosen for each fit and the other shapes, which also describe well the fit sample, are  
 480 used as alternative to estimate systematic uncertainties:

- Functions used for fitting  $m_j$  spectrum:

$$F_{\text{ErfExp}}(x) = e^{c_0 x} \cdot \frac{1 + \text{Erf}((x - a)/b)}{2}$$

$$F_{\text{ErfPow}}(x) = \frac{(1 + \text{Erf}((x - A)/B))}{2} \cdot x^{\text{CLog}x}$$

$$F_{\text{ExpGaus}}(x) = e^{c_0 x} \cdot e^{-(x - x_0)^2 / 2\sigma^2}$$

$$F_{\text{4Gaus}}(x) = c_0 \cdot G_0(x, x^0, \sigma^0) + c_1 \cdot G_1(x, x^1, \sigma^1) + c_2 \cdot G_2(x, x^2, \sigma^2) + c_3 \cdot G_3(x, x^3, \sigma^3)$$

- Functions used for fitting  $m_{lvj}$  spectrum in the range [0.4-1.3] TeV:

$$\begin{aligned} F_{\text{ErfPowExp}}(x) &= \frac{1 + \text{Erf}((x - a)/b)}{2} \cdot e^{-c_0 s} \cdot s^{-c_1 \log(s)} \\ F_{\text{ErfPowPow}}(x) &= \frac{1 + \text{Erf}((x - a)/b)}{2} \cdot s^{-(c_0 + c_1 \log(s))} \\ F_{\text{ErfPow}}(x) &= \frac{(1 + \text{Erf}((x - A)/B))}{2} \cdot x^{\text{CLog}x} \\ F_{\text{ExpGaus}}(x) &= e^{c_0 x} \cdot e^{-(x - x_0)^2 / 2\sigma^2} \end{aligned} \quad (17)$$

- Functions used for fitting  $m_{lvj}$  spectrum in the range [0.7-3.0] TeV:

$$\begin{aligned} F_{\text{ExpN}}(x) &= e^{c_0 x + n/x} \\ F_{\text{ExpTail}}(x) &= e^{-x/(c_0 + c_1 x)} \\ F_{\text{Exp}}(x) &= e^{c_0 x} \\ F_{\text{PowPow}}(x) &= (1 - s)^{c_0} \cdot x^{c_1} \end{aligned} \quad (18)$$

481 where  $s = x/C$  and  $C$  is some constant, selected with different initial values depending if we  
 482 fit the  $m_j$  or the  $m_{lvj}$  distribution.

483 In the first step, the W+jets normalization in the signal region is extracted from a sideband fit,  
 484 using both the upper and the lower sideband regions,  $m_j = [40-65, 105-130]$  GeV.

485 Fits for the non-dominant background like  $t\bar{t}$ , single top, and diboson (WW/WZ) processes are  
 486 extracted from MC; their shapes are strongly dependent on the N-subjettines category and on  
 487 the chosen  $m_{lvj}$  range of fit, which are defined according to the is listed in Tab.5.

488 In Fig. 14, these fits are shown for muon channel high purity and low purity categories, con-  
 489 sidering only events with  $m_{lvj}$  in [0.4-1.3] TeV, while, in Fig. 15, the same fits are shown for the  
 490 events in the range [0.7-3.0] TeV.

Mass (TeV)	$m_{lvj}$ (TeV)	Category	W+Jets	$t\bar{t}$	Single Top	VV
[0.6-0.7]	[0.4-1.3]	HP	$F_{\text{ErfExp}}$	$F_{\text{ErfExp2Gaus}}$	$F_{\text{ExpGaus}}$	$F_{\text{4Gaus}}$
[0.6-0.7]	[0.4-1.3]	LP	$F_{\text{ErfExp}}$	$F_{\text{ExpGaus}}$	$F_{\text{ExpGaus}}$	$F_{\text{ExpGaus}}$
[0.8-2.5]	[0.7-3.0]	HP	$F_{\text{ErfExp}}$	$F_{\text{ErfExp2Gaus}}$	$F_{\text{ExpGaus}}$	$F_{\text{4Gaus}}$
[0.8-2.5]	[0.7-3.0]	LP	$F_{\text{ErfExp}}$	$F_{\text{ExpGaus}}$	$F_{\text{ExpGaus}}$	$F_{\text{ExpGaus}}$

Table 5: Summary of all the shapes used for fit the  $m_j$  spectra of each background component, taking into account: bulk graviton mass,  $m_{lvj}$  fit range and N-subjettines category.

491 Shapes and normalizations of the non-dominant backgrounds are fixed to what is obtained  
 492 from the MC; finally, the normalization of the W+jets contribution is extracted from the fit to the  
 493 data jet mass distribution in the sideband region. These fits are shown in Fig. 16, considering all  
 494 the events with  $m_{lvj}$  in [0.4-1.3] TeV, for the high purity and low purity muon categories (upper  
 495 line), for low purity and high purity electron channel (bottom line). On the contrary, the same  
 496 plots are replied in Fig. 17, taking into account high mass events, where  $m_{lvj}$  lies between [0.7-  
 497 3.0] TeV. The factor for correcting the simulated W-peak position and resolution to the observed  
 498 data, taken from the  $t\bar{t}$  control sample, are included in the plots of Fig. 16 and Fig.17.

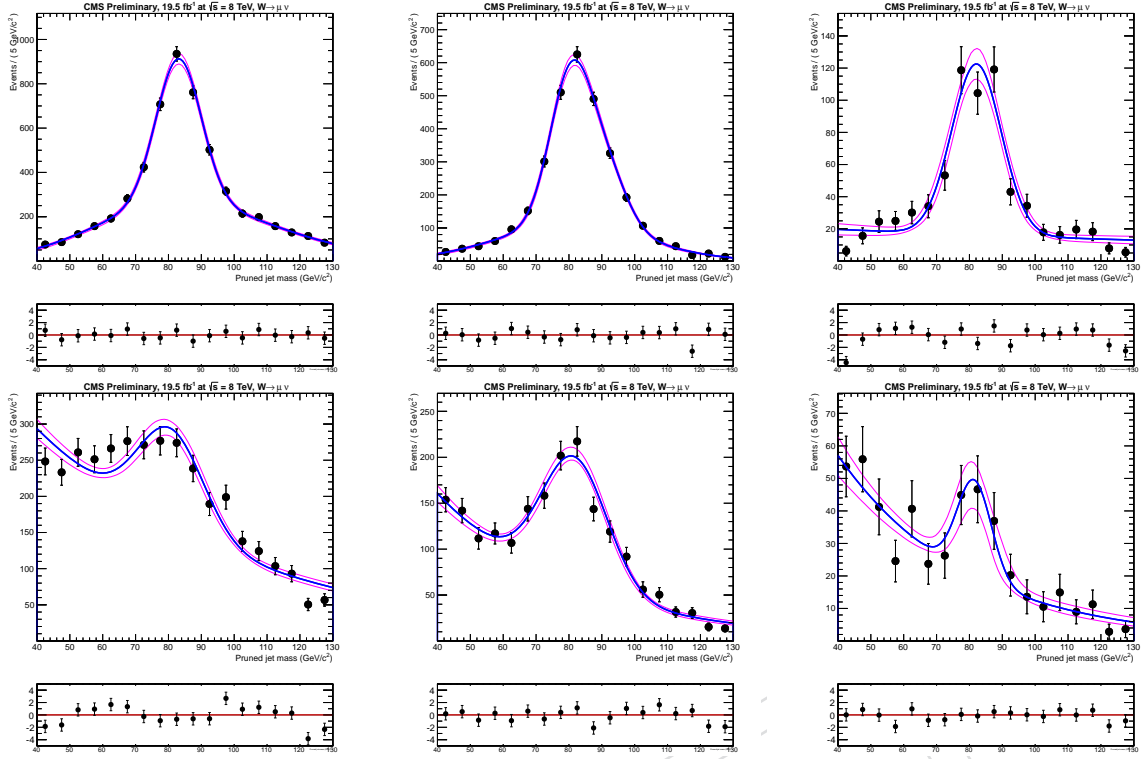


Figure 14: MC fits of non-dominant background  $m_j$  spectra for events with total invariant mass  $m_{lvj}$  in the range [0.4-1.3] TeV: on top (bottom) high purity (low purity) categories for the muon channel. Left to right are the  $t\bar{t}$ , diboson ( $WW/WZ$ ) and Single Top processes.

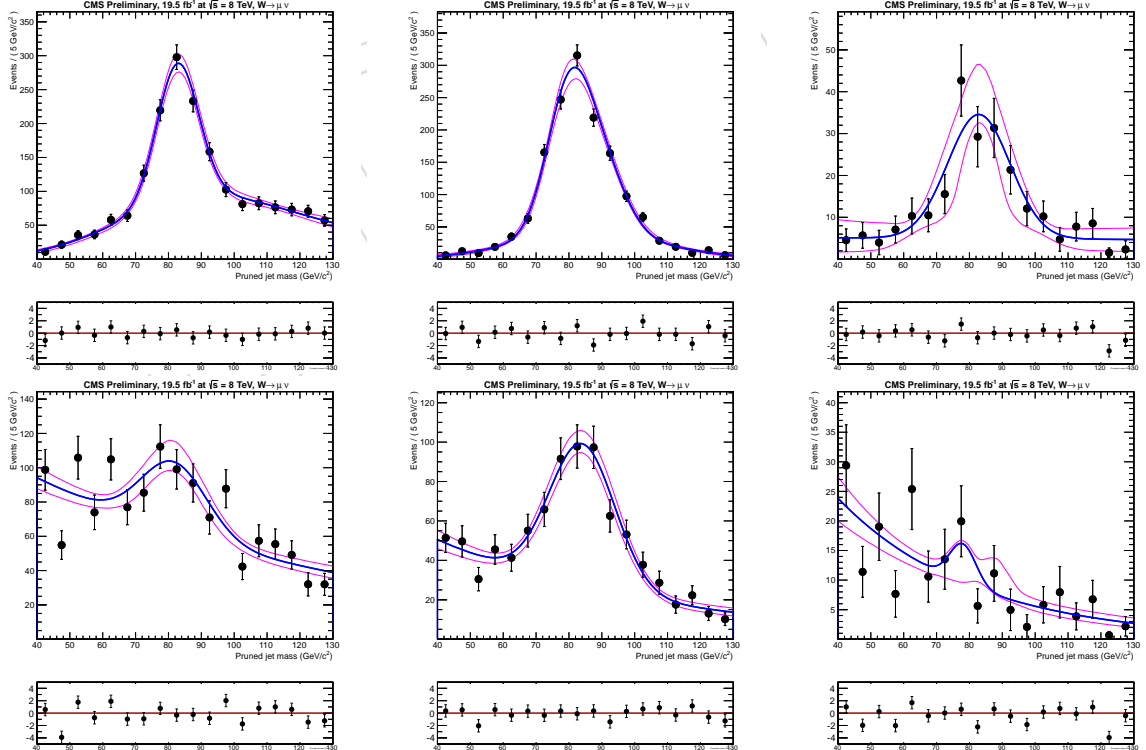


Figure 15: MC fits of non-dominant background  $m_j$  spectra for events with total invariant mass  $m_{lvj}$  in the range [0.7-3.0] TeV: on top (bottom) high purity (low purity) categories in muon channel. Left to right are the  $t\bar{t}$ , diboson ( $WW/WZ$ ) and single top processes.

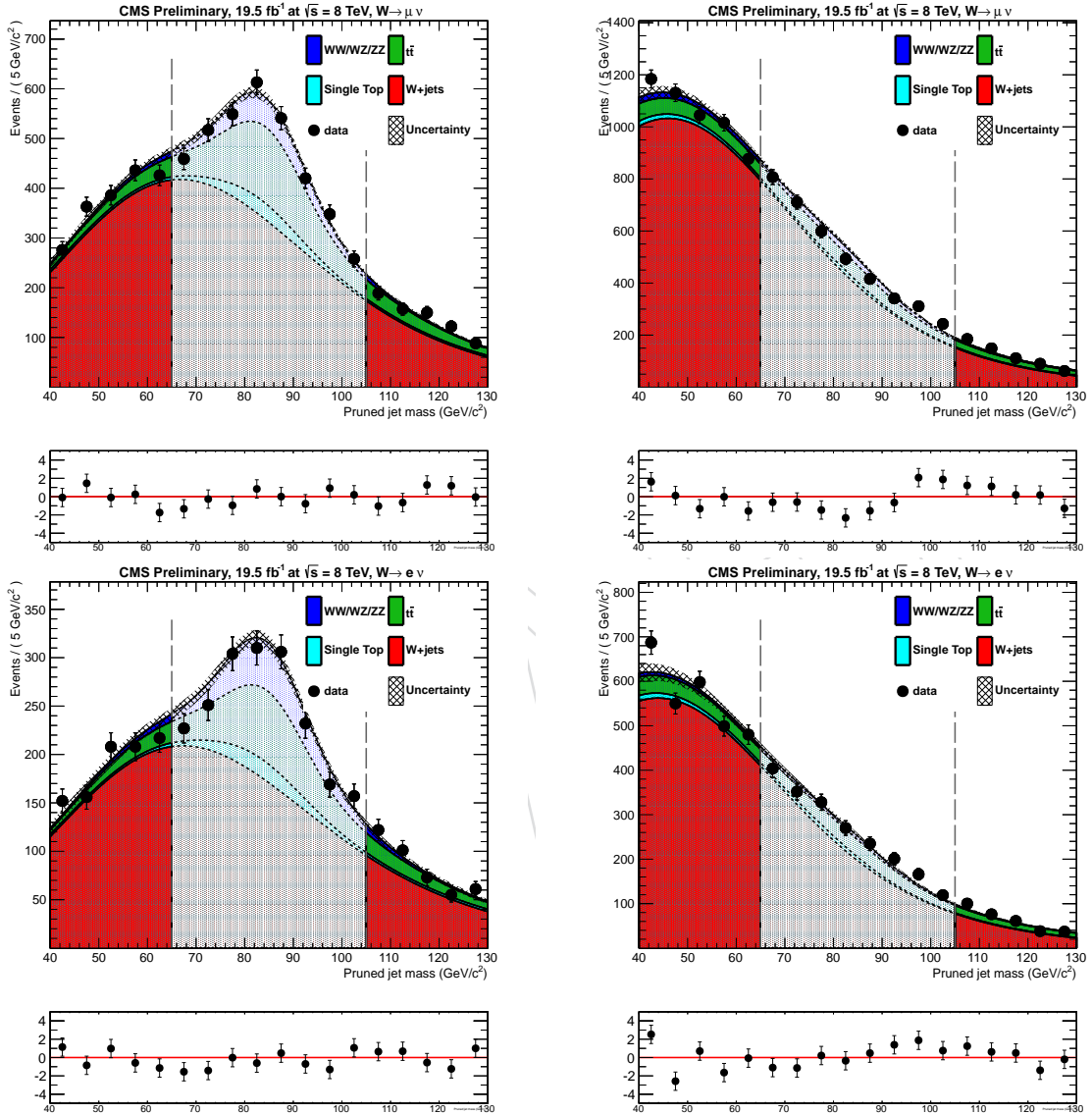


Figure 16: Fits to extract the relative shape and normalization of the  $W + \text{jets}$  contribution from the data in the jet mass distribution, taking only the events with  $m_{lj}$  in [0.4-1.3] TeV. Top line fits for the muon channel: high purity (left) and low purity (right) category. Bottom line fits for the electron channel: high purity (left) and low purity (right) category.

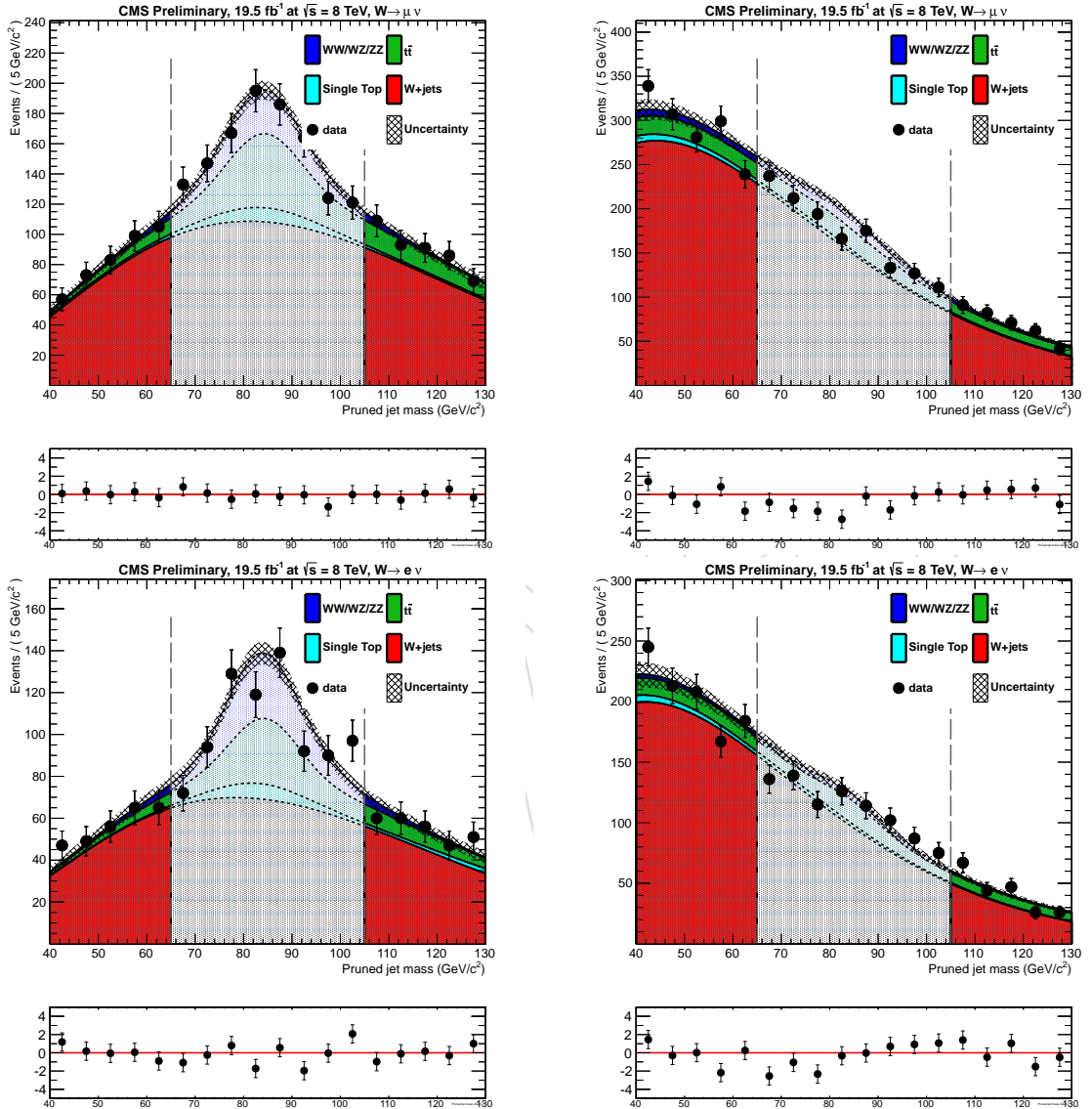


Figure 17: Fits to extract the relative shape and normalization of the  $W+\text{jets}$  contribution from the data in the jet mass distribution, taking only the events with  $m_{l\nu j}$  in [0.7-3.0] TeV. Top line fits for the muon channel: high purity (left) and low purity (right) category. Bottom line fits for the electron channel: high purity (left) and low purity (right) category.

499 In the next step, we calculate the extrapolation factor,  $\alpha_{\text{MC}}(m_{l\nu j})$ . The function  $\alpha$  is determined  
500 from MC, in order to account for the correlations between the jet mass and the mass of the three-  
501 body system. We use the Herwig++ determination of the function  $\alpha_{\text{MC}}(m_{l\nu j})$ , as Herwig++ is  
502 known to better describe the jet substructure [17]. The difference between the Herwig++ and  
503 Pythia6 determinations is used as a systematic effect on W+jets shape related to the adopted  
504 parton shower model; this will be described in more detail later.

505 For the  $m_{l\nu j}$  distribution, we use two different mass window as a function of the signal mass  
506 hypotheses:  $m_{l\nu j}$  in [0.4-1.3] TeV for  $m_G = 0.6, 0.7$  TeV and  $m_{l\nu j}$  in [0.7-3.0] TeV for  $m_G =$   
507 [0.8, 2.5] TeV (in steps of 100 GeV, as reported in Table 2). This is why, when you consider res-  
508 onance with low mass, even if the signal has been generated in narrow width approximation,  
509 you need to fit a total background which has a turn on between [0.4-0.6] TeV plus a falling tail,  
510 while for a narrow high mass resonance above 800 GeV, the background shape is expected to  
511 be a purely falling distribution; thus the chosen fit ranges and fit functions are taken to reflect  
512 this.

513 The lower limit for the  $m_{WW}$  fit at high mass, which is fixed at 700 GeV, has been chosen looking  
514 at the invariant mass shape variation applying a looser set of kinematic selections on MET and  
515 leptonic and hadronic W  $p_T$ .<sup>7</sup> In Fig. 18, a comparison between the  $m_{l\nu j}$  shapes in the signal  
516 region, obtained after the standard kinematic selection of the analysis (red points) and after a  
517 set of looser cuts ( $E_T^{\text{miss}} > 40(70)$  GeV for  $\mu$  (el) and  $p_T^{\text{Wlep}}, p_T^{\text{CA8}} > 150$  GeV), are shown for each  
518 channel and each category.

519 The turn on shapes, where  $m_{l\nu j}$  is between [0.4, 0.65] TeV, are clearly affected by the adopted  $p_T$   
520 thresholds, while starting from 700 GeV, the ratio of the two remains flat near to one in each  
521 channel and in each category. Thus, this value is chosen as lower limit for fitting the  $m_{WW}$   
522 spectrum with a simple failing model, since, above this point, there are no sculpting effects on  
523 the shapes due to missing transverse energy and W  $p_T$  cuts.

524 Finally, for the fit function, the  $F_{\text{ExpN}}(m_{l\nu j})$ , defined in Eq. 18, is taken as default shape when  
525 W+jets spectrum is fitted in the range between [0.7-3.0] TeV, while the  $F_{\text{ExpTail}}(m_{l\nu j})$  is used as  
526 alternative function to evaluate shape systematics. The reason of this choice is explained in the  
527 appendix A. On the contrary, for low mass resonances, the W+jets background is fitted in the  
528 range [0.4-1.3] TeV with a  $F_{\text{ExpPowErf}}(m_{l\nu j})$ , defined in Eq. 17, while the  $F_{\text{ErfPowPow}}(m_{l\nu j})$  is used  
529 as alternative function.

530

531 The shapes of the  $\alpha$  functions can be seen in Fig. 19 for both muon and electron channels, high  
532 and low purity categories, fitting the W+jets in the low mass range  $m_{l\nu j} \in [0.4-1.3]$  TeV, while,  
533 in Fig. 44, the same plots are reported for events in the high mass spectrum.

534 Using the fits in the lower  $m_j$  sideband region from Fig. 16 and Fig. 17, we can get the shape  
535 of the W+jets in  $m_{l\nu j}$  in the lower sideband region from data,  $F_{\text{data,LSB}}(m_{l\nu j})$ . We must also fit  
536 the contribution of the non-dominant backgrounds both in the sideband and signal regions in  
537  $m_{l\nu j}$ , as well again fixing their normalizations and shapes from MC. Since also the  $m_{WW}$  shape  
538 is dependent on both the  $m_j$  region of fit and on the  $m_{l\nu j}$  range of fit, the chosen shapes are  
539 listed in Table. 6.

540 In Fig. 21 and Fig. 22, these fits are shown respectively for muon and electron channel, both high  
541 purity and low purity categories, considering only events in the low sideband ( $m_j \in [40, 65]$  GeV)

<sup>7</sup>Selection on lepton  $p_T$  cannot be moved to lower values since they are designed to keep the analysis on the trigger plateau.

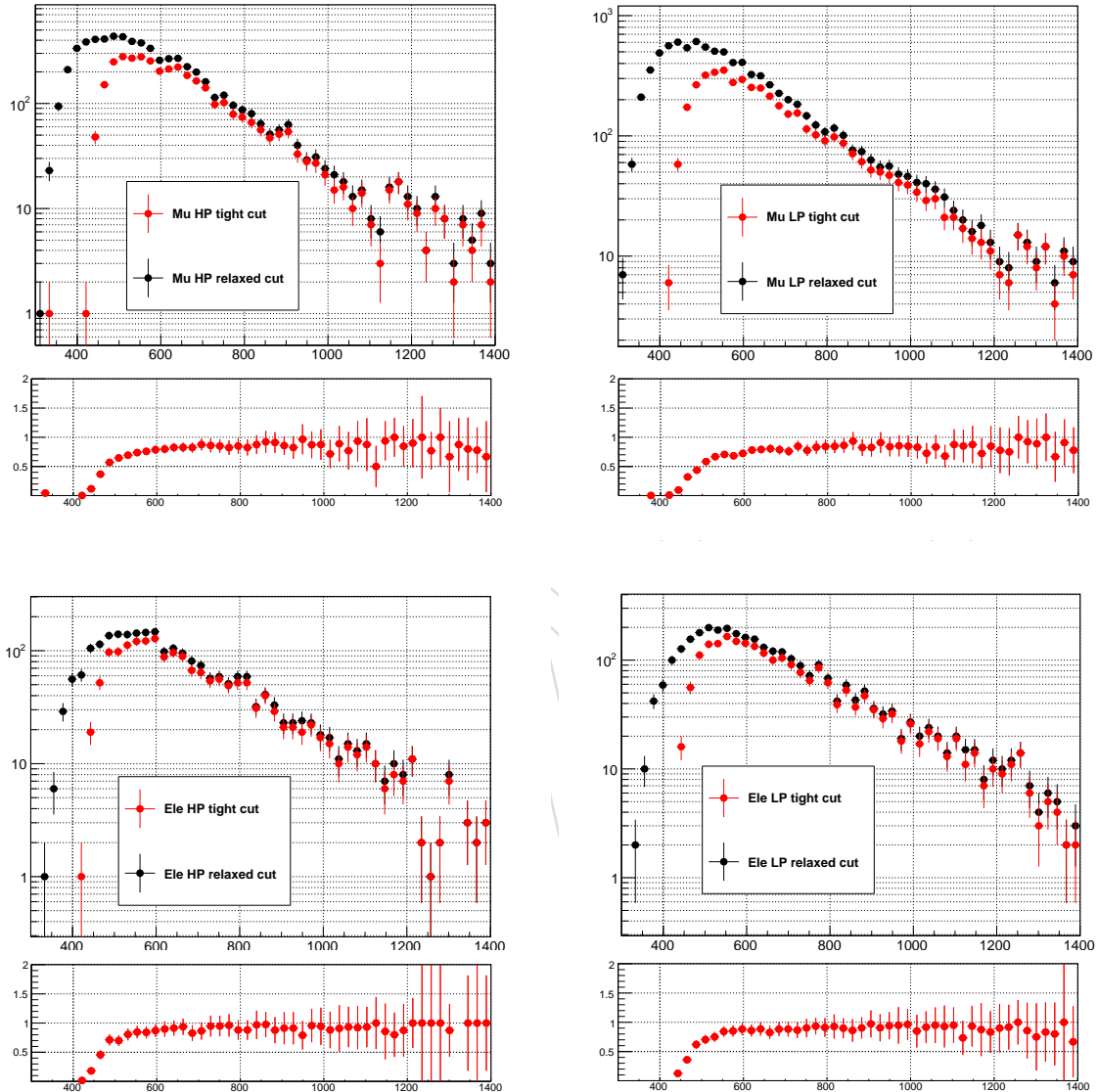


Figure 18:  $m_{lvj}$  shapes obtained after different set of kinematic selections on  $E_T^{miss}$  and hadronic and leptonic W  $p_T$ ; Red points refer to the usual event selection described in Sec. 5.1, while black ones to a set of relaxed cuts. (Top left) muon HP, (top right) muon LP, (bottom left) electron high purity and (bottom right) electron low purity. Red and black shapes are normalized to the same area.

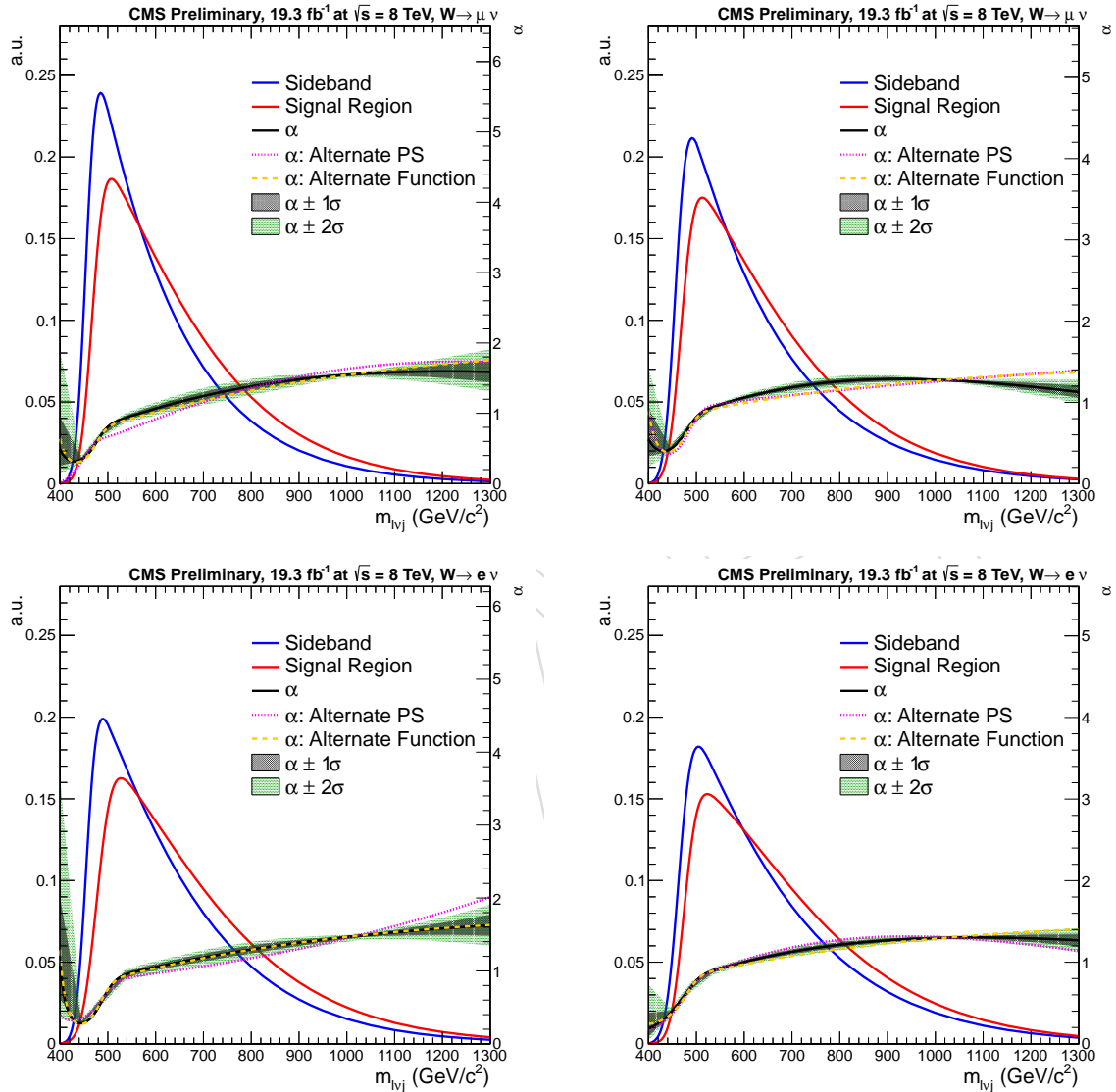


Figure 19: The functions  $\alpha_{MC}(m_{lvj})$  for the  $\mu$  high purity category (top left),  $\mu$  low purity (top right), electron high purity (bottom left) and electron low purity (bottom right), obtained fitting the MC  $W+jets$  background between [0.4-1.3] TeV.

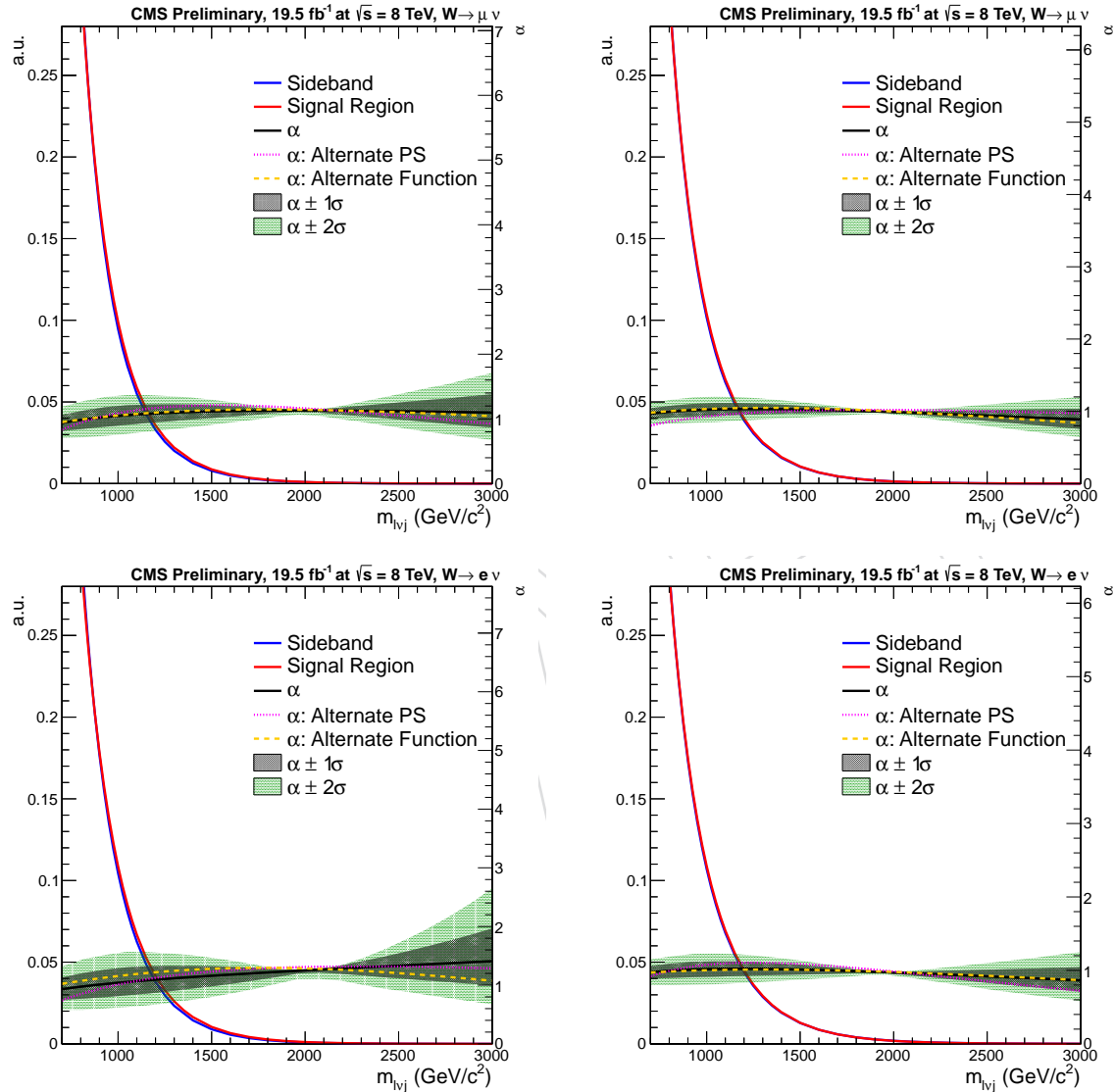


Figure 20: The functions  $\alpha_{MC}(m_{lvj})$  for the  $\mu$  high purity category (top left),  $\mu$  low purity (top right), electron high purity (bottom left) and electron low purity (bottom right), obtained fitting the MC W+jets background between [0.7-3.0] TeV.

Mass (TeV)	$m_{l\nu j}$ (TeV)	$m_j$	Region	$W+Jets$	$t\bar{t}$	Single Top	VV
[0.6-0.7]	[0.4-1.3]		SB	$F_{ErfPowExp}$	$F_{ErfExp}$	$F_{ErfExp}$	$F_{ErfExp}$
[0.6-0.7]	[0.4-1.3]		SR	$F_{ErfPowExp}$	$F_{ErfPowExp}$	$F_{ErfExp}$	$F_{ErfPowExp}$
[0.8-2.5]	[0.7-3.0]		SB	$F_{ExpN}$	$F_{Exp}$	$F_{Exp}$	$F_{Exp}$
[0.8-2.5]	[0.7-3.0]		SR	$F_{ExpN}$	$F_{Exp}$	$F_{Exp}$	$F_{ExpN}$

Table 6: Summary of all the shapes used for fit the  $m_{l\nu j}$  spectrum of each background component, taking into account: bulk graviton mass,  $m_{l\nu j}$  fit range and  $m_j$  region of fit (SB = sideband, SR = signal region).

542 with  $m_{l\nu j}$  in [0.4-1.3] TeV; on the contrary, in Fig. 23 and Fig. 24, the same fits are shown for  
543 events inside the signal region.

544 In Fig. 25 and Fig. 26, non-dominant MC background fits are shown, respectively, for muon  
545 and electron channel, both high purity and low purity categories, considering only events in  
546 the low sideband ( $m_j \in [40,65]$  GeV) with  $m_{l\nu j}$  in [0.7-3] TeV; on the contrary, in Fig. 27 and  
547 Fig. ??, the same fits are shown for events inside the signal region.

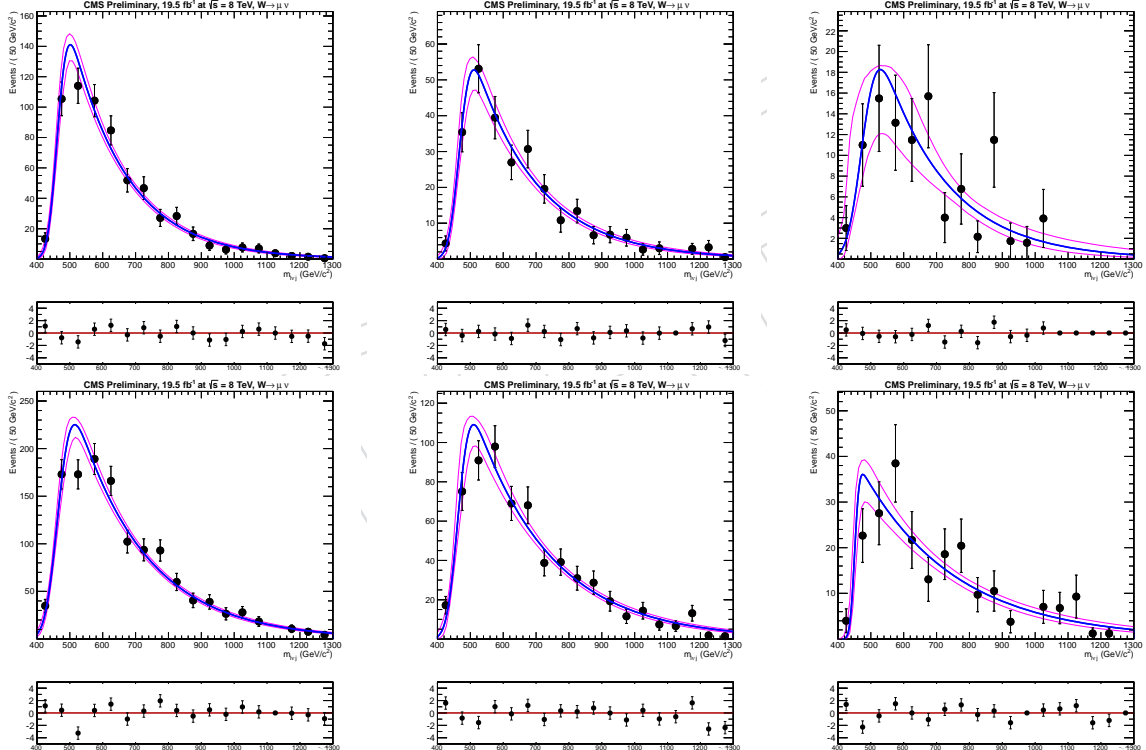


Figure 21: MC fits of non-dominant background  $m_{l\nu j}$  spectra for muon events, in the  $m_j$  sideband, with  $m_{l\nu j}$  in the range [0.4-1.3] TeV: on top (bottom) high purity (low purity) categories for the muon channel. Left to right are the  $t\bar{t}$ , diboson (WW/WZ) and Single Top processes.

548 The fits for  $F_{data,LSB}(m_{l\nu j})$  are shown in Fig. 29 and in Fig. 30; again upper line refers to the  
549 muon channel, high purity on the left, low purity on the right, while the bottom line shows the  
550 electron channel results. The uncertainties on the fits are also included in the plot, based on the  
551 parametric errors estimation.

552 To extrapolate the  $W+jet$  shape into the signal region, we use both the function  $\alpha_{MC}(m_{l\nu j})$ ,  
553 computed in Fig. 19 and Fig. 44, and the  $W+jet$  shapes extracted from data in the sideband,  
554 shown in Fig. 29 and Fig. 30. Combining MC fits of non-dominant backgrounds in the  $m_{l\nu j}$

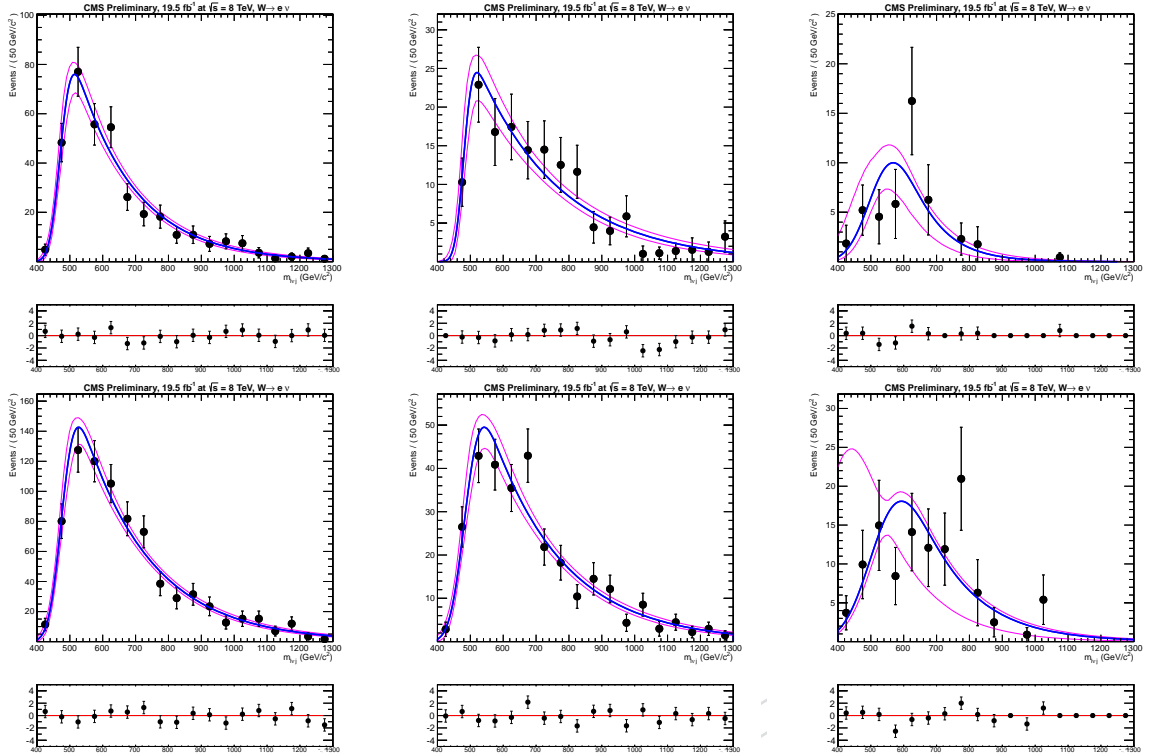


Figure 22: MC fits of non-dominant background  $m_{lvj}$  spectra for electron events, in the  $m_j$  sideband, with  $m_{lvj}$  in the range [0.4-1.3] TeV: on top (bottom) high purity (low purity) categories for the muon channel. Left to right are the  $t\bar{t}$ , diboson (WW/WZ) and Single Top processes.

555 signal region with the W+jet shapes, extrapolated from the sidebands, we have the final  $m_{lvj}$   
 556 distributions in the signal region. This is shown in Fig. 31 and in Fig. 32, for both electron  
 557 (bottom) and muon (top) channels, high purity (left) and low purity (right) categories. The  
 558 expected signal shapes for a Bulk graviton with  $m_G = 0.6$  TeV and 1 TeV are also shown; this  
 559 will be described in more detail in the next section.

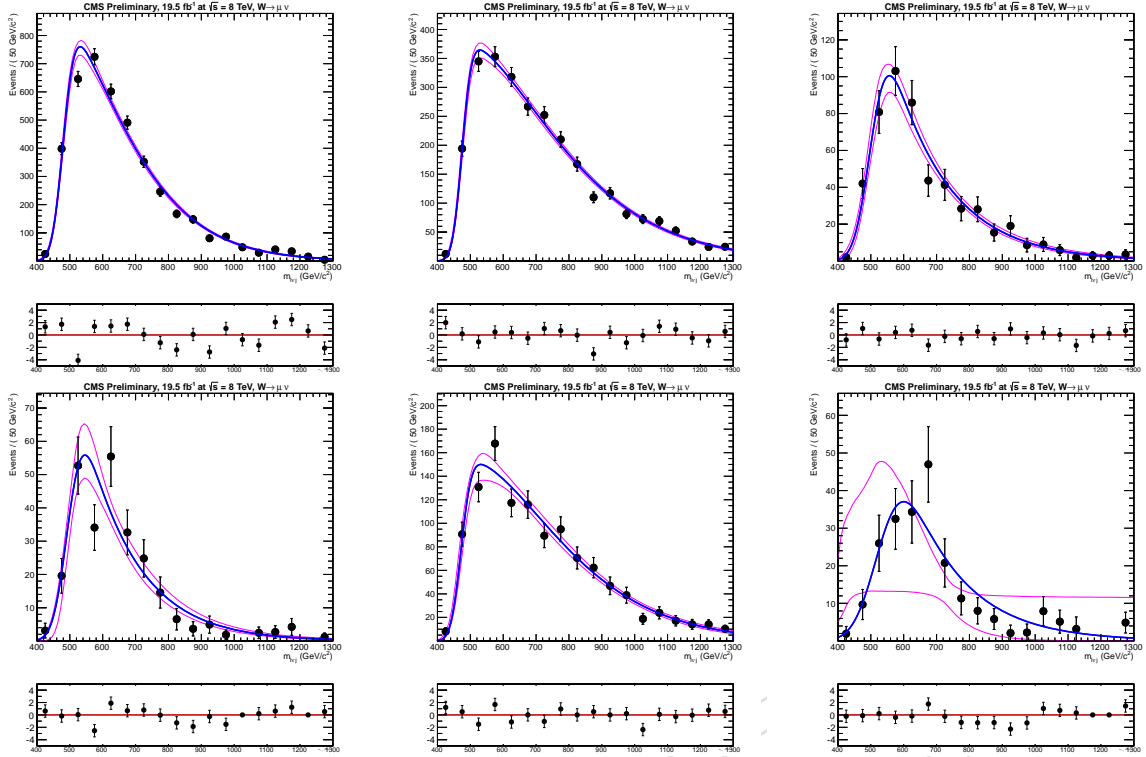


Figure 23: MC fits of non-dominant background  $m_{lvj}$  spectra for muon events, in the  $m_j$  signal region, with  $m_{lvj}$  in the range [0.4-1.3] TeV: on top (bottom) high purity (low purity) categories for the muon channel. Left to right are the  $t\bar{t}$ , diboson (WW/WZ) and Single Top processes.

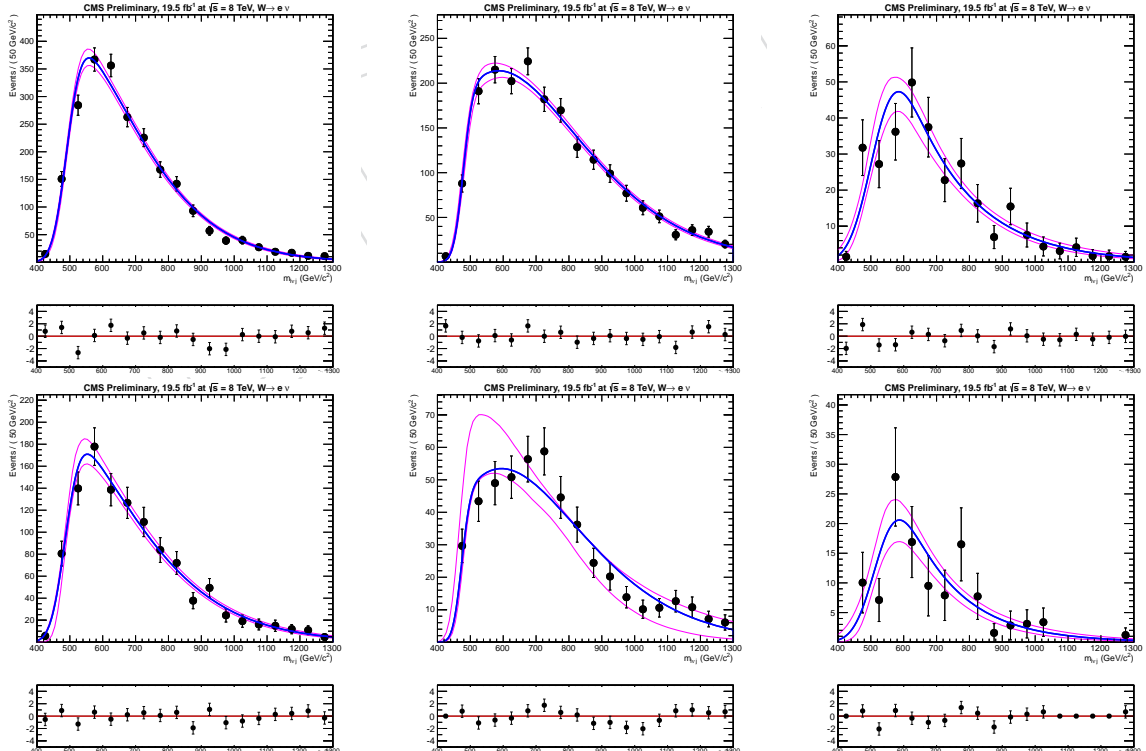


Figure 24: MC fits of non-dominant background  $m_{lvj}$  spectra for electron events, in the  $m_j$  signal region, with  $m_{lvj}$  in the range [0.4-1.3] TeV: on top (bottom) high purity (low purity) categories for the muon channel. Left to right are the  $t\bar{t}$ , diboson (WW/WZ) and Single Top processes.

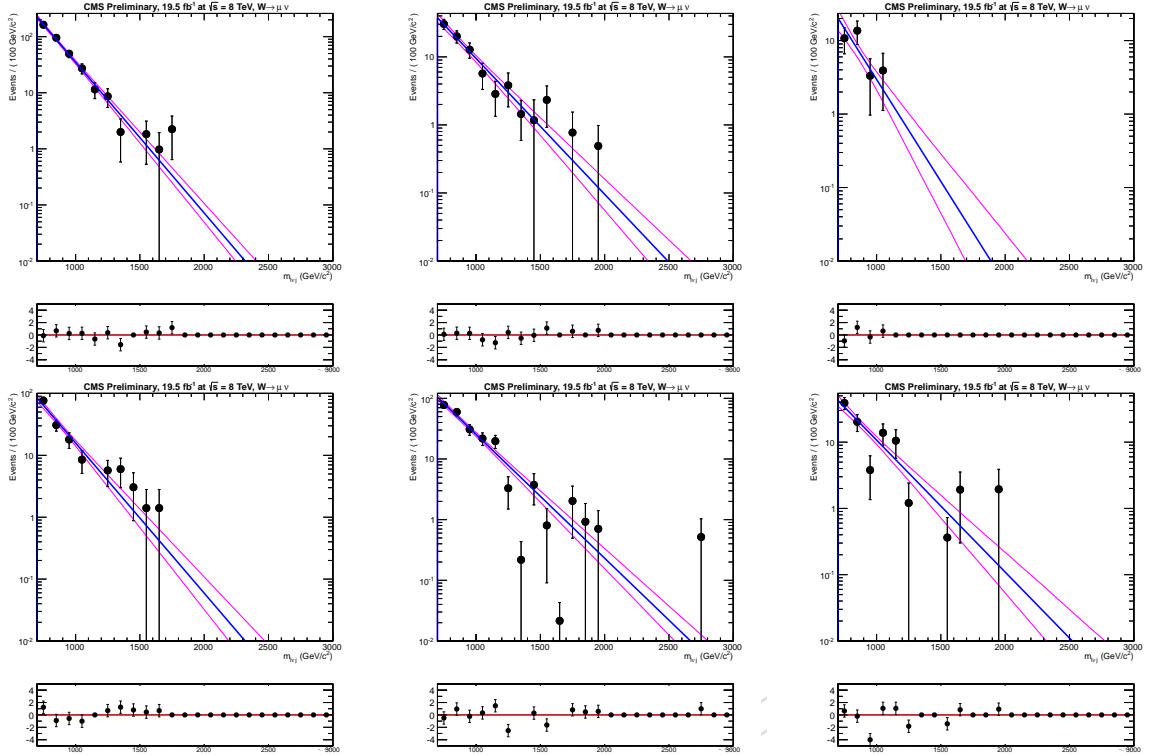


Figure 25: MC fits of non-dominant background  $m_{lvj}$  spectra for muon events, in the  $m_j$  sideband, with  $m_{lvj}$  in the range [0.7-3] TeV: on top (bottom) high purity (low purity) categories for the muon channel. Left to right are the  $t\bar{t}$ , diboson ( $WW/WZ$ ) and Single Top processes.

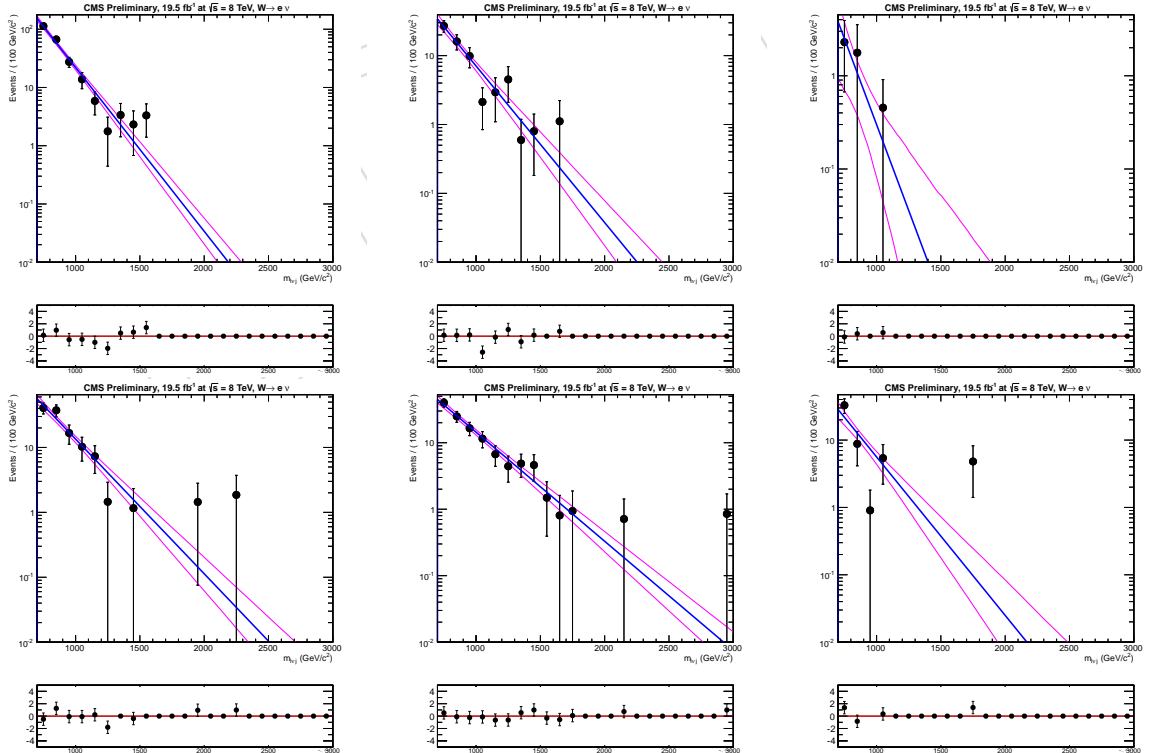


Figure 26: MC fits of non-dominant background  $m_{lvj}$  spectra for electron events, in the  $m_j$  sideband, with  $m_{lvj}$  in the range [0.7-3] TeV: on top (bottom) high purity (low purity) categories for the muon channel. Left to right are the  $t\bar{t}$ , diboson ( $WW/WZ$ ) and Single Top processes.

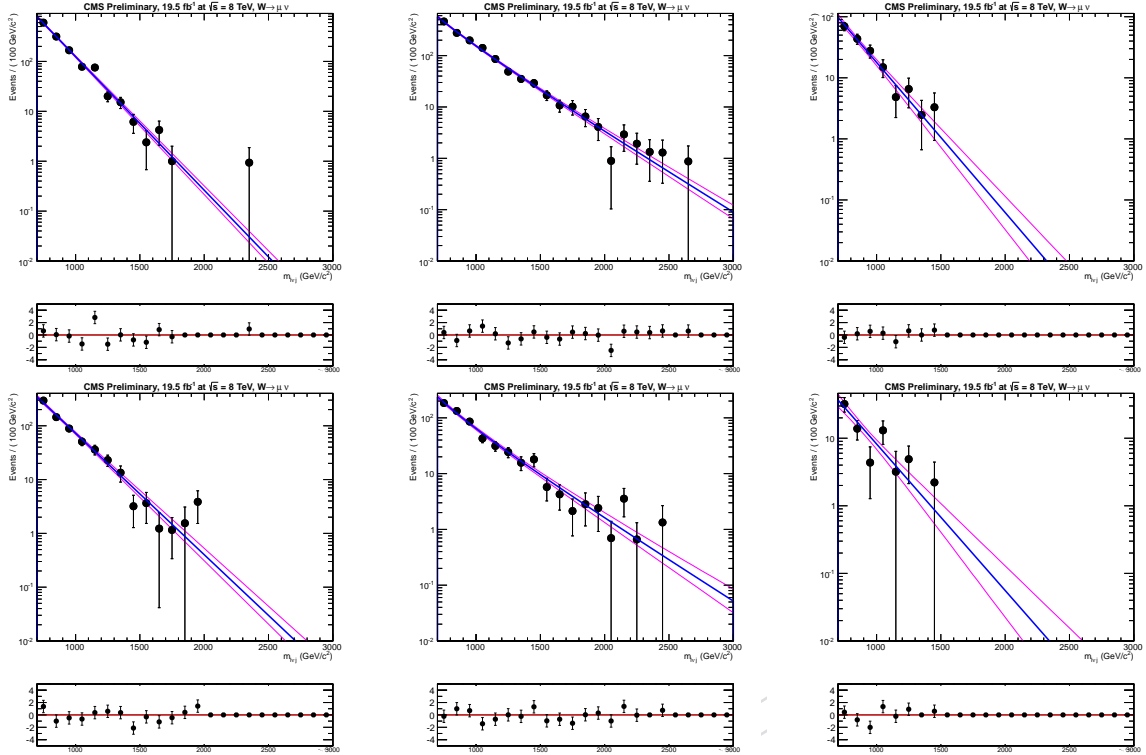


Figure 27: MC fits of non-dominant background  $m_{lvj}$  spectra for muon events, in the  $m_j$  signal region, with  $m_{lvj}$  in the range [0.7-3] TeV: on top (bottom) high purity (low purity) categories for the muon channel. Left to right are the  $t\bar{t}$ , diboson ( $WW/WZ$ ) and Single Top processes.

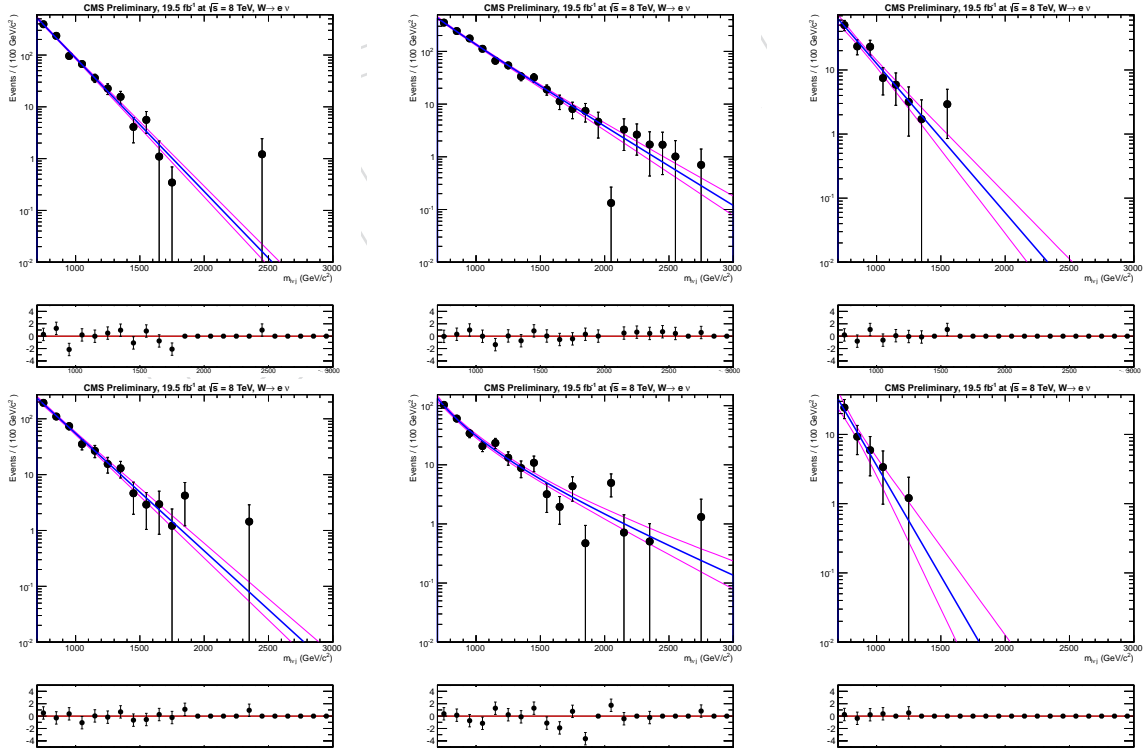


Figure 28: MC fits of non-dominant background  $m_{lvj}$  spectra for electron events, in the  $m_j$  signal region, with  $m_{lvj}$  in the range [0.7-3] TeV: on top (bottom) high purity (low purity) categories for the muon channel. Left to right are the  $t\bar{t}$ , diboson ( $WW/WZ$ ) and Single Top processes.

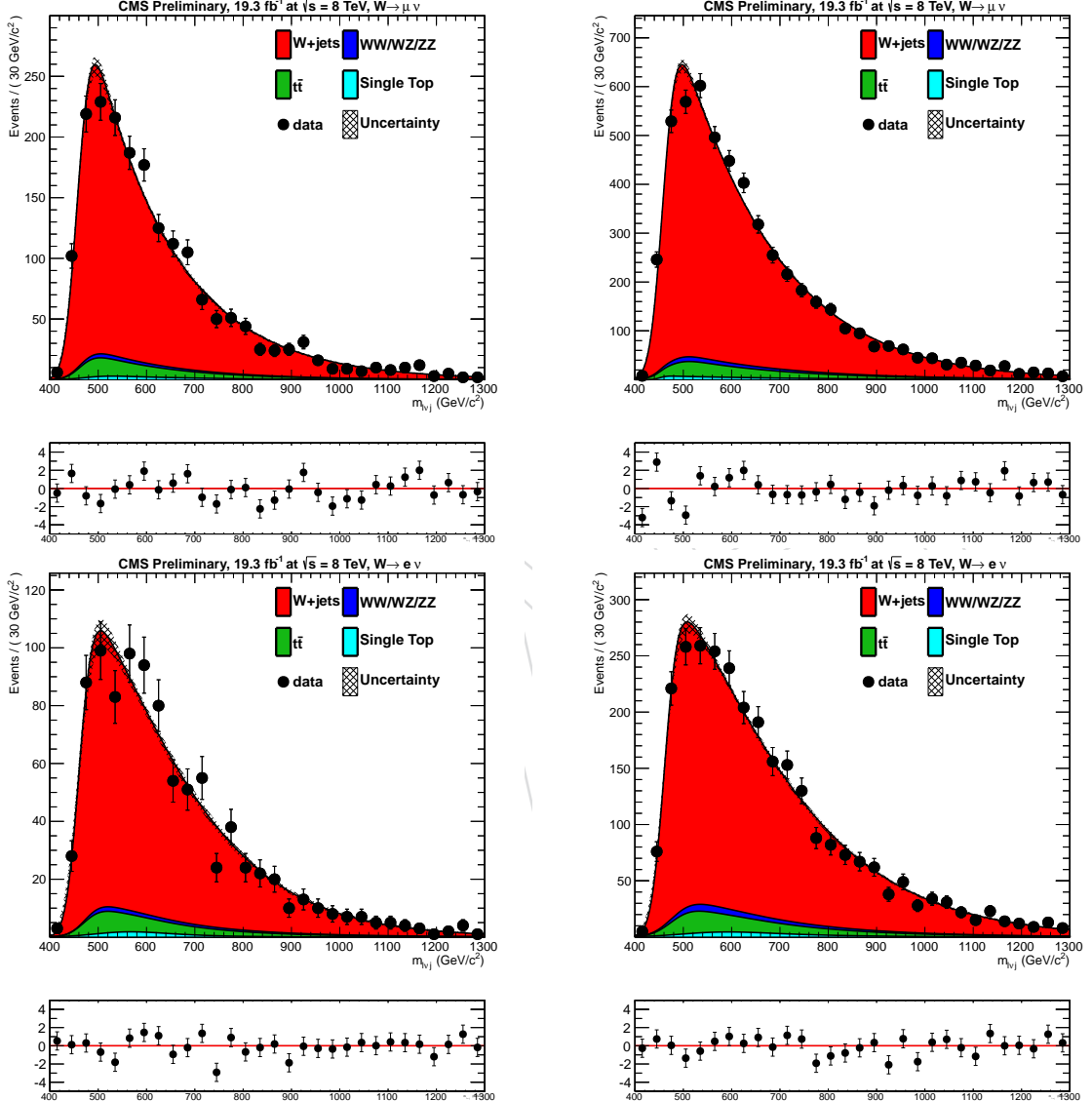


Figure 29: The fits for  $F_{\text{data},\text{LSB}}(m_{\nu j})$  for both electron (bottom) and muon (top) channels, high purity (left) and low purity (right) categories, taking into account events with  $m_{\nu j}$  between [0.4-1.3] TeV.

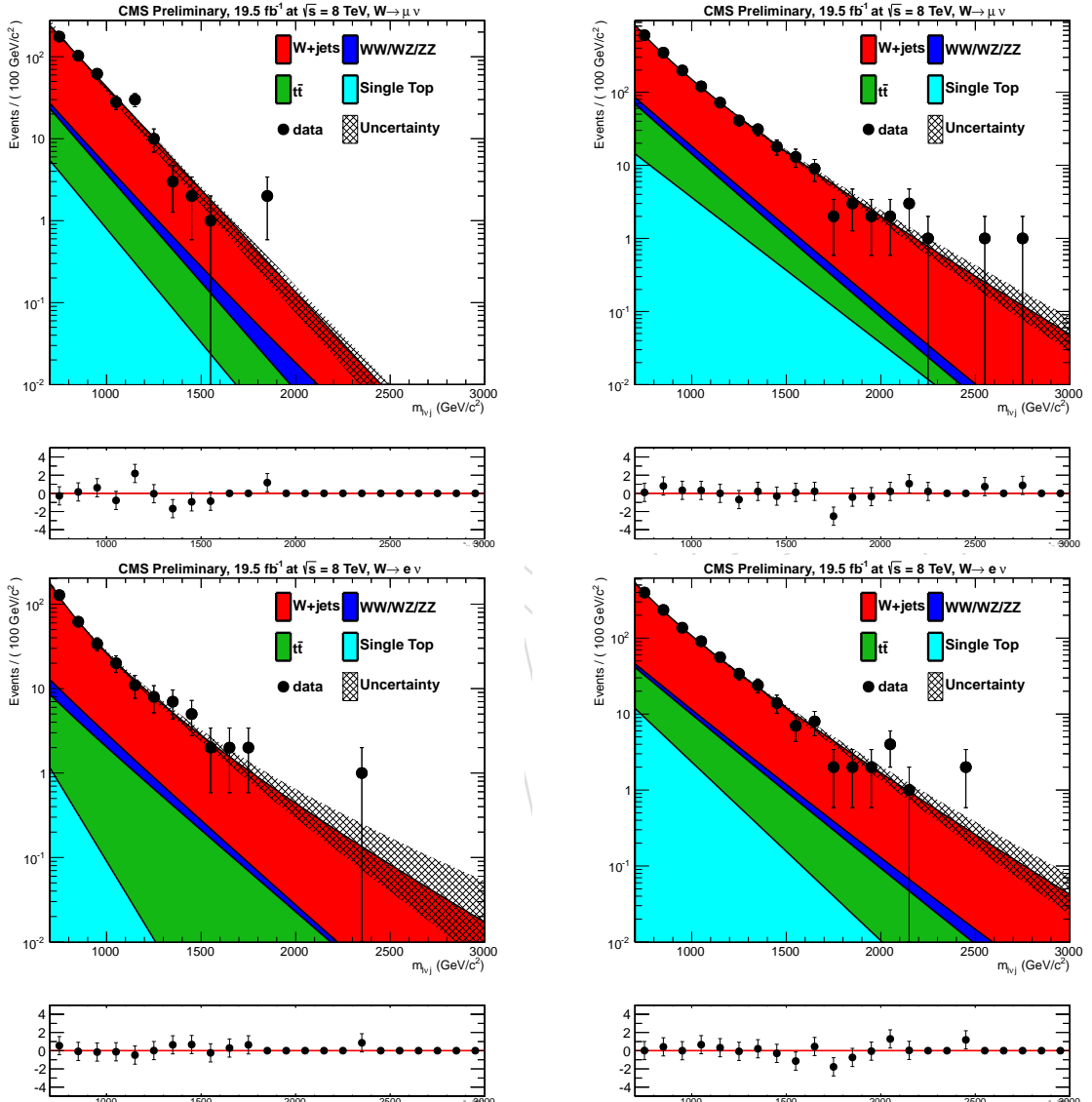


Figure 30: The fits for  $F_{\text{data},\text{LSB}}(m_{\nu j})$  for both electron (bottom) and muon (top) channels, high purity (left) and low purity (right) categories, taking into account events with  $m_{\nu j}$  between [0.7-3.0] TeV.

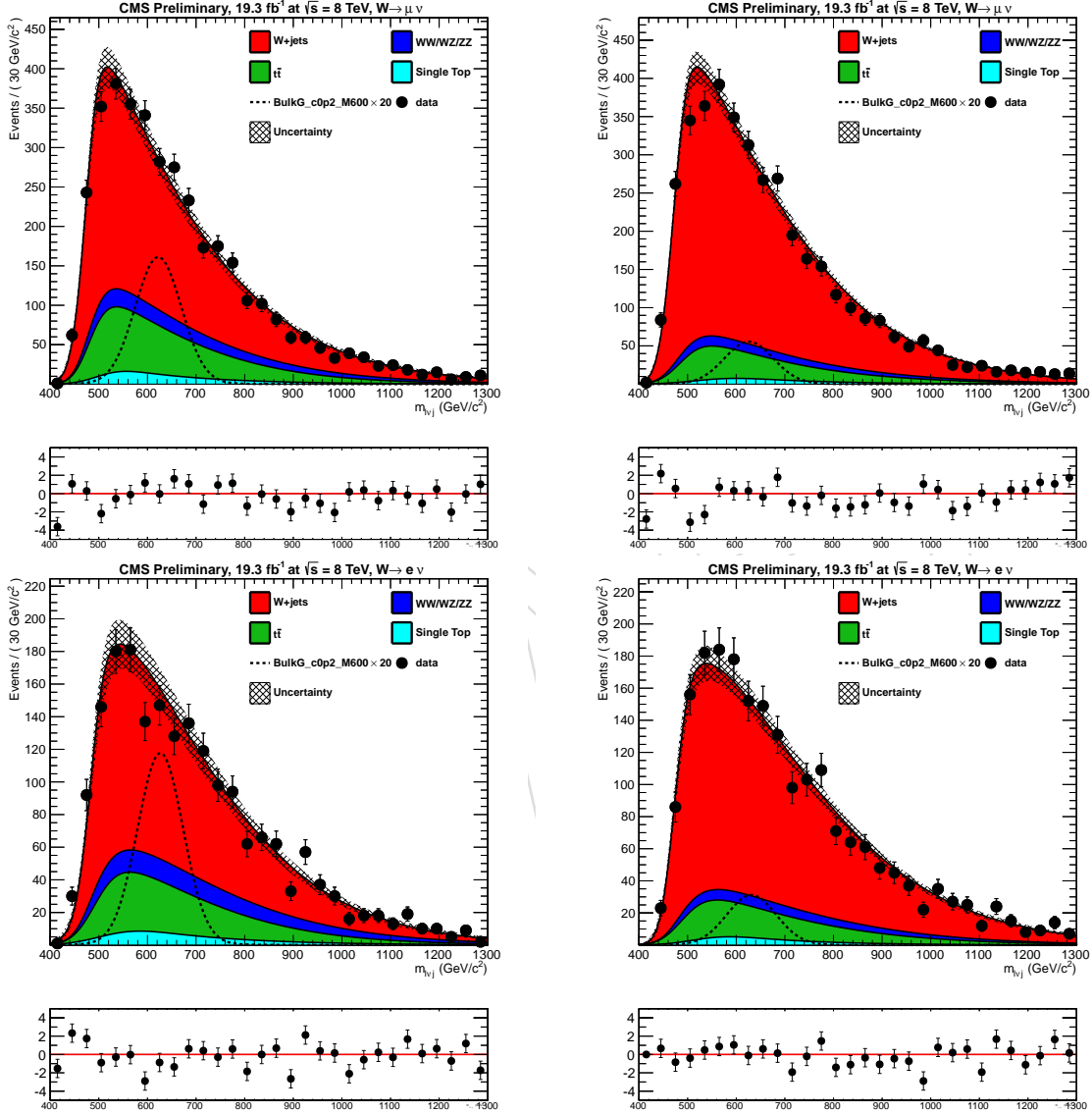


Figure 31: Final distributions in  $m_{lvj}$  for data and expected backgrounds in electron+jet final state (bottom) and muon (top) channel, for events with  $m_{lvj}$  between [0.4-1.3] TeV. Left, high purity category ( $\tau_2/\tau_1 < 0.5$ ); right, low purity category ( $\tau_2/\tau_1 \in [0.5, 0.75]$ ).

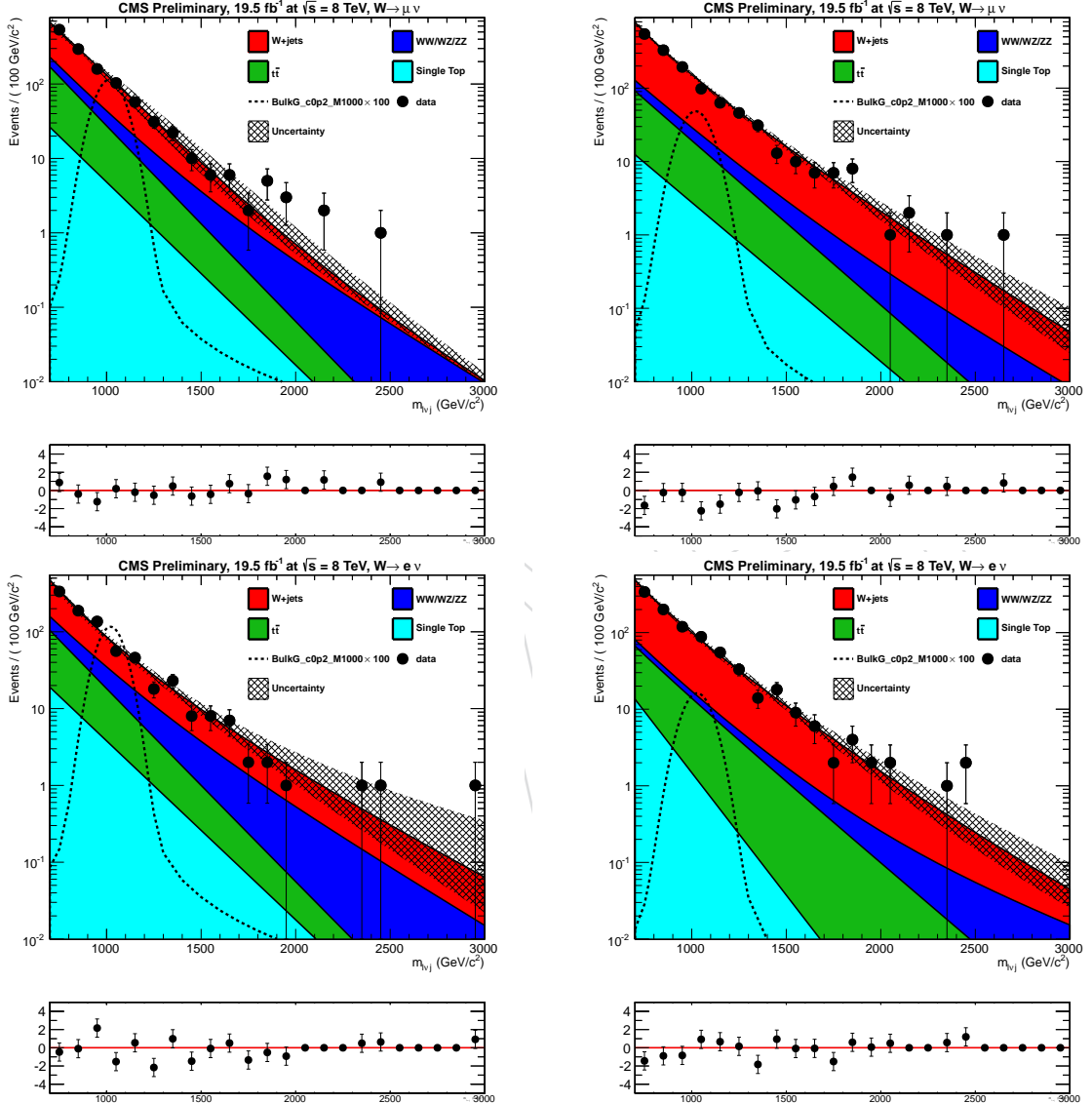


Figure 32: Final distributions in  $m_{lvj}$  for data and expected backgrounds in electron+jet final state (bottom) and muon (top) channel, for events with  $m_{lvj}$  between [0.7-3.0] TeV. Left, high purity category ( $\tau_2/\tau_1 < 0.5$ ); right, low purity category ( $\tau_2/\tau_1 \in [0.5, 0.75]$ ).

## 560 5.5 Signal Model

561 As stated in Sec 2.2.1, we consider bulk graviton samples with  $\tilde{k} = 0.2$  for modelling the signal  
 562  $m_{WW}$  shape. The intrinsic width of the resonance, obtained using this  $\tilde{k}$  value, is sufficiently  
 563 small when compared with the detector resolution for high mass samples ( $m_G > 1$  TeV). This  
 564 makes the model used for generating the events independent from the detector effects on the  
 565 signal shape, allowing a model independent search for narrow resonances at high mass. The  
 566 signal shapes are fitted with a Crystal-Ball function for all the graviton mass hypothesis above  
 567 1 TeV; as an example, fits for the muon channel categories are shown in the upper line of Fig. 33,  
 568 for a graviton mass of  $m_G = 1.5$  TeV, while, in the bottom line, the same results are reported for  
 569 the electron case.

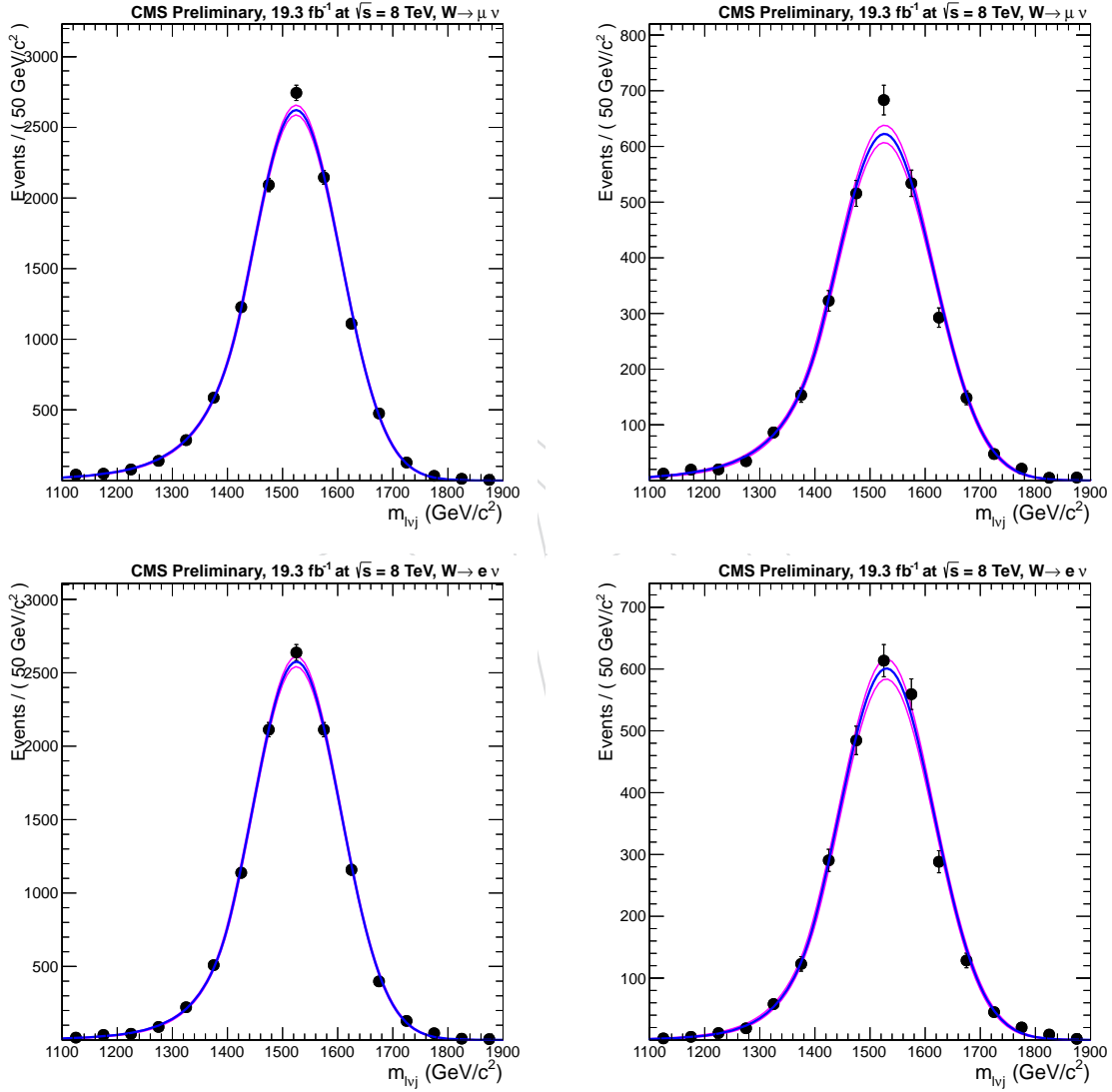


Figure 33: Modelling of the signal shape with a Crystal Ball function: top muon channel high purity (left), low purity category (right); bottom electron channel high purity (left), low purity category (right).

570 On the contrary, for masses below 1 TeV, this assumption is not valid anymore, so the model  
 571 considered for the signal shape is a Voigtian function, which is defined as the convolution  
 572 between a Breit-Wigner core and a gaussian resolution function. Since we are interested in

573 extract the experimental resolution, the intrinsic width of the Breit-Wigner is constrained in the  
 574 fit to what is generated in the narrow width approximation. As an example, fits for the muon  
 575 channel categories are shown in the upper line of Fig. 34, for a graviton mass of  $m_G = 0.6$  TeV,  
 576 while, in the bottom line, the same results are reported for the electron case.

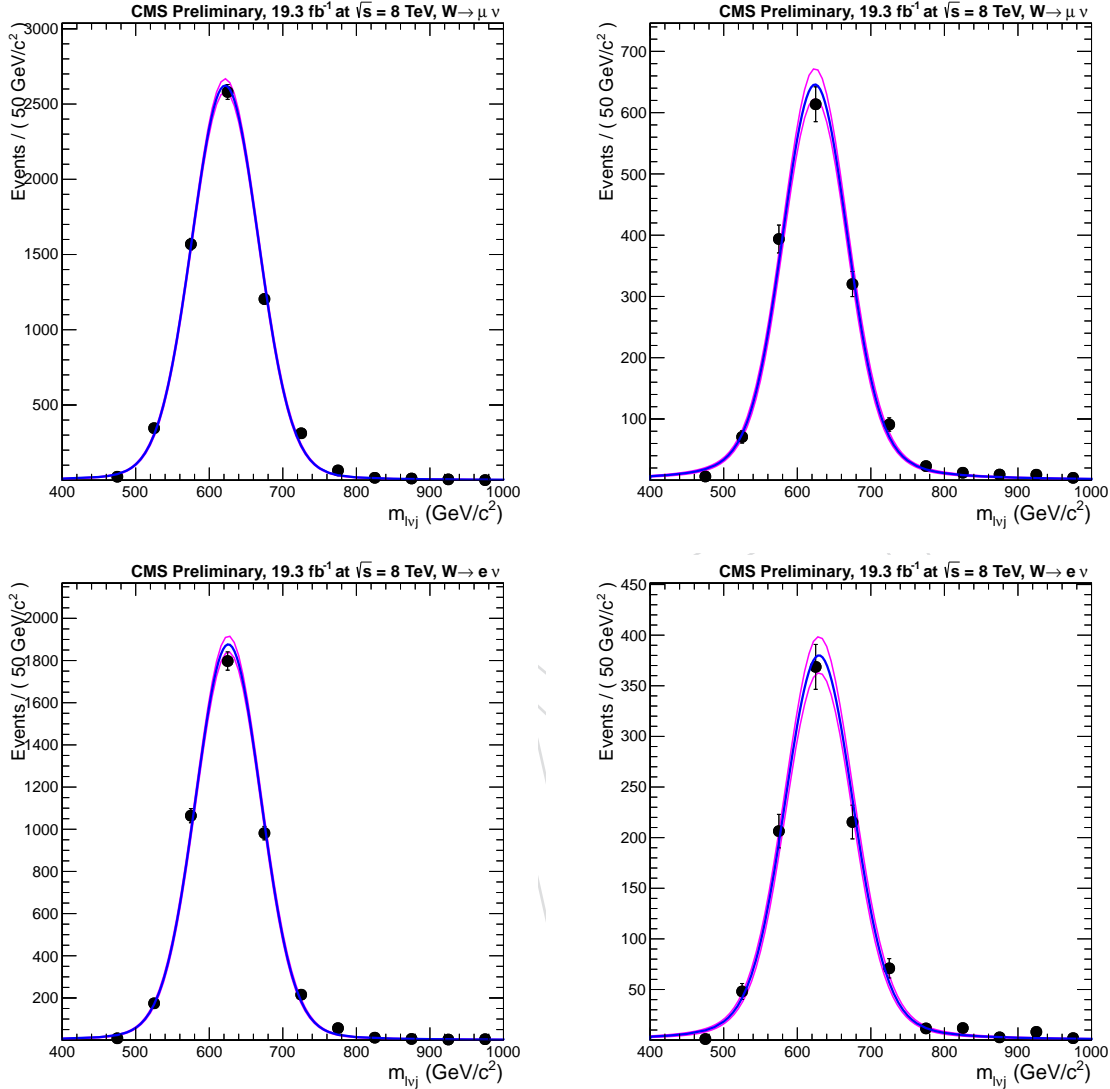


Figure 34: Modelling of the signal shape with Voigtian function at low mass: top muon channel high purity (left), low purity category (right); bottom electron channel high purity (left), low purity category (right).

577 A summary of the fitted peak position and width of the gaussian core are presented in Tab. 7  
 578 for different mass points, both for electron and muon channels, high and low purity categories.  
 579 The electron and muon shapes are similar also at high invariant mass, since the resolution is  
 580 dominated by the missing energy contribution. No significant dependence on the V-tag purity  
 581 is found in the presented analysis.

Mass (TeV)	Fit Model	Intrinsic Width $\Gamma$ (GeV)	Mean (TeV)	Peak Width (GeV)
Muon Channel High Purity				
0.6	Voig	2.5 (13.0)	0.622	$\sigma_{Voig}=47$
1	Voig	2.5 (13.0)	1.016	$\sigma_{Voig}=68$
1.5	CB	3.75 (19.5)	1.522	$\sigma_{CB}=91$
2	CB	5.0 (26.0)	2.024	$\sigma_{CB}=105$
2.5	CB	6.25 (32.5)	2.525	$\sigma_{CB}=114$
Muon Channel Low Purity				
0.6	Voig	2.5 (13.0)	0.626	$\sigma_{Voig}=50$
1	Voig	2.5 (13.0)	1.021	$\sigma_{Voig}=74$
1.5	CB	3.75 (19.5)	1.524	$\sigma_{CB}=98$
2	CB	5.0 (26.0)	2.025	$\sigma_{CB}=115$
2.5	CB	6.25 (32.5)	2.520	$\sigma_{CB}=136$
Electron Channel High Purity				
0.6	Voig	2.5 (13.0)	0.626	$\sigma_{Voig}=46$
1	Voig	2.5 (13.0)	1.021	$\sigma_{Voig}=65$
1.5	CB	3.75 (19.5)	1.524	$\sigma_{CB}=86$
2	CB	5.0 (26.0)	2.024	$\sigma_{CB}=99$
2.5	CB	6.25 (32.5)	2.530	$\sigma_{CB}=112$
Electron Channel Low Purity				
0.6	Voig	2.5 (13.0)	0.631	$\sigma_{Voig}=50$
1	Voig	2.5 (13.0)	1.029	$\sigma_{Voig}=72$
1.5	CB	3.75 (19.5)	1.529	$\sigma_{CB}=104$
2	CB	5.0 (26.0)	2.029	$\sigma_{CB}=112$
2.5	CB	6.25 (32.5)	2.528	$\sigma_{CB}=120$

Table 7: The main parameters (mean and sigma) extracted from the signal shape fits for muon and electron channels. The intrinsic width  $\Gamma$  is quoted for bulk gravitons with  $\tilde{k} = 0.2$  ( $\tilde{k} = 0.5$ ) taken from [1].

### 5.5.1 Signal Efficiency

The signal reconstruction efficiency in each four category is defined as:

$$\epsilon = \frac{N_{sel}^{cat}}{N_{gen}} \quad (19)$$

where  $N_{sel}^{cat}$  is the number of signal events after the whole analysis selection in a chosen category, while  $N_{gen}$  is the number of generated events, including both electron and muon final states ( $X \rightarrow WW \rightarrow l\nu q\bar{q}$ ,  $l = e, \mu$ ).

The signal efficiencies are evaluated inside the signal region ( $m_j \in [65, 105]$  GeV) and they are listed in Table 8. The HP efficiency drops at high values of the resonance mass due to the inefficiency of the N-subjettiness selection; this is partially recovered in the LP category. At high mass, also the  $m_j$  cut reduces the efficiency, due to a degradation of the pruned jet mass distribution as proved in [17].

Graviton Mass (TeV)	$\epsilon_{\mu}^{HP}$ (%)	$\epsilon_{\mu}^{LP}$ (%)	$\epsilon_e^{HP}$ (%)	$\epsilon_e^{LP}$ (%)
0.6	14.1	2.5	9.5	1.7
0.7	17.2	3.1	13.3	2.4
0.8	19.4	3.8	16.7	3.1
0.9	20.4	4.3	18.1	3.3
1.0	22.0	4.6	19.5	4.0
1.1	22.1	5.1	20.1	4.6
1.2	23.0	4.9	20.6	4.8
1.3	23.0	5.0	21.4	5.7
1.4	23.1	5.4	21.8	5.3
1.5	22.5	5.8	21.4	5.3
1.6	21.8	5.9	21.6	5.7
1.7	21.6	5.9	21.4	6.1
1.8	20.7	6.5	20.8	6.3
1.9	20.6	6.6	20.2	6.4
2.0	20.1	6.3	19.8	6.6
2.1	19.7	6.6	19.7	6.8
2.2	18.6	6.8	18.0	7.0
2.3	17.5	7.3	16.5	6.7
2.4	16.3	6.9	16.6	6.9
2.5	14.9	7.1	16.5	7.1

Table 8: Expected signal efficiency for high-purity (HP) and low-purity (LP) categories, in electron and muon channel separately, for several resonance mass hypothesis.

## 591 6 Systematic Uncertainties

592 Systematic uncertainties are detailed in this section, we divide them into two sub-groups: back-  
 593 ground normalization and shape, signal normalization and shape.

### 594 6.1 Background Normalization and Shape

#### 595 6.1.1 Normalization and shape uncertainties on W+jets contribution

596 As discussed in Section 5.4, we fit the  $m_j$  spectrum in lower and upper sideband regions to  
 597 extract the W+jets normalization in the signal one. The shape uncertainty of the non-dominant  
 598 backgrounds are ignored (unless the  $t\bar{t}$ ), while the yield uncertainties are included in the final  
 599 limit setting.

600 The W+jets normalization uncertainty comes from three contributions:

- 601 • The uncertainties on the fit parameters.
- 602 • Differences in the parton shower models (Herwig++ and Pythia6).
- 603 • Differences coming from alternative shape functions.

604 Data in the low sideband region are fitted fixing the shape parameters, coming from different  
 605 parton shower models in the MC, while the high mass tail is floated in data. The uncertainty  
 606 related to the fitting function choice is defined by taking the normalization uncertainty between  
 607 using the default function  $F_{\text{ErfExp}}$ , and an alternate function  $F_{\text{PowPow}}$ .

608 The procedure for extracting the shape of the W+jets background contribution is described in  
 609 Sec. 5.4. Eq. 16 shows the components which are inputed to the background shape:  $F_{\text{data,SR}}(m_{lvj})$   
 610 and  $\alpha_{\text{MC}}$ . Thus, the shape uncertainty comes from uncertainties related to the function  $\alpha_{\text{MC}}$  and  
 611 the W+jets  $m_{lvj}$  shape uncertainty, obtained fitting data in  $m_j$  lower sideband region.

612 In Fig. 19 and Fig. 44, the black (green) shadow shows the 1 (2)  $\sigma$  bands from parameter un-  
 613 certainties. The magenta and yellow dashed lines denote, respectively, the  $\alpha_{\text{MC}}$  derived from  
 614 alternative parton shower models and alternative fitting functions. The variation from alterna-  
 615 tive fitting functions is small compared to the one coming from the alternative parton shower  
 616 model. To account for the additional shape variation from these two effects, for simplicity, we  
 617 inflate the parameter errors to cover this systematic uncertainty by a factor 2 for high mass  
 618 points  $m_G \in [0.8, 2.8]$  TeV, while, for low masses  $m_g = [0.6, 0.7]$  GeV, we use  $\sqrt{2}$ . It can be seen  
 619 in Fig. 19 and in Fig. 44 that this is sufficiently conservative to cover the shape variations.

620 The W+jets  $m_{lvj}$  shape uncertainty comes directly from the fit, which can be seen in Fig. 29  
 621 and in Fig. 30. The shape comes from the data and is not subject to MC deficiencies such as  
 622 the parton shower model, so we only need to consider the parameter uncertainties and fitting  
 623 function uncertainty. As in the case of the  $\alpha_{\text{MC}}$ , we decided to inflate the parameters uncertainty  
 624 in order to include the one coming from the fitting function alternate shapes.

### 625 6.2 Shape uncertainty on the $t\bar{t}$ shape

626 The  $t\bar{t}$  background shape comes from simulation. This is found to be reasonable given the  
 627 agreement between data and simulation we saw in the  $t\bar{t}$  control region, as shown in Sec 5.3.  
 628 In addition, we assign parametric errors from these fits on MC as systematic uncertainties.  
 629 Further, we attempt to assess the size of systematic shape difference by comparing the fitted  
 630 shape in the MC against alternative simulation samples. We compare the fitted shapes obtained  
 631 by means of different generators and normalization/factorization scale choices:

- 632     • Powheg  
 633     • MadGraph  
 634     • MadGraph, scale up  
 635     • MadGraph, scale down  
 636     • MadGraph, matching up  
 637     • MadGraph, matching down

638 The various shapes can be seen in Fig. 35 and in Fig. 36, respectively they show the shape  
 639 variation for fits performed in the low mass range ( $m_{l\nu j} \in [0.4\text{-}1.3] \text{ TeV}$ ) and in the high mass  
 640 one ( $m_{l\nu j} \in [0.8\text{-}2.8] \text{ TeV}$ ) in the  $m_j$  signal region. In order to cover the multiple shape variations,  
 641 we inflated the  $t\bar{t}$  uncertainties by a factor of two.

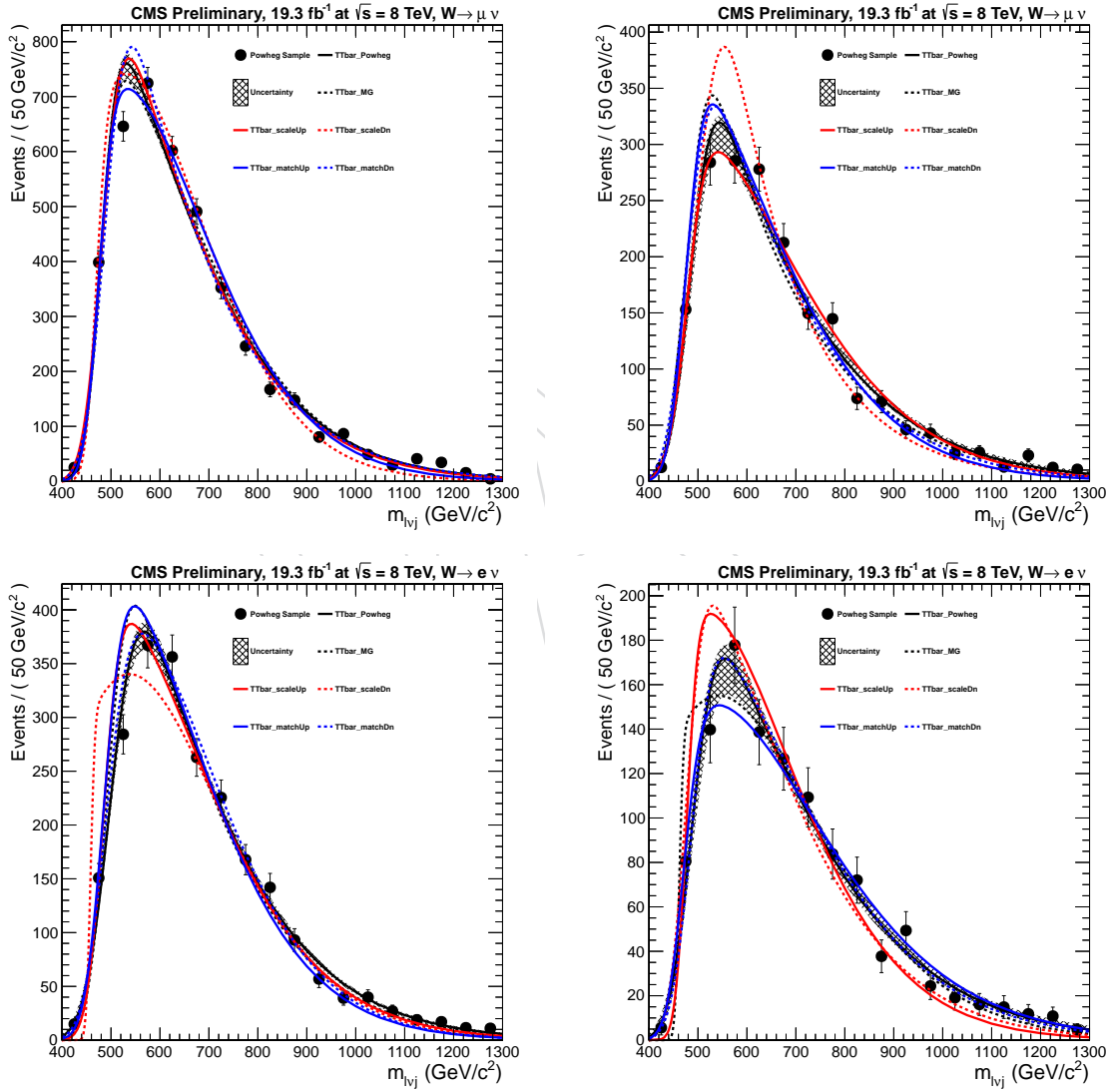


Figure 35: Shape variations in the  $t\bar{t}$  for events with  $m_{l\nu j} \in [0.4\text{-}1.3] \text{ TeV}$ . Top plot refer to the muon channel: left high purity category, right low purity one. Bottom plot refer to electron channel: left high purity category, right low purity one.

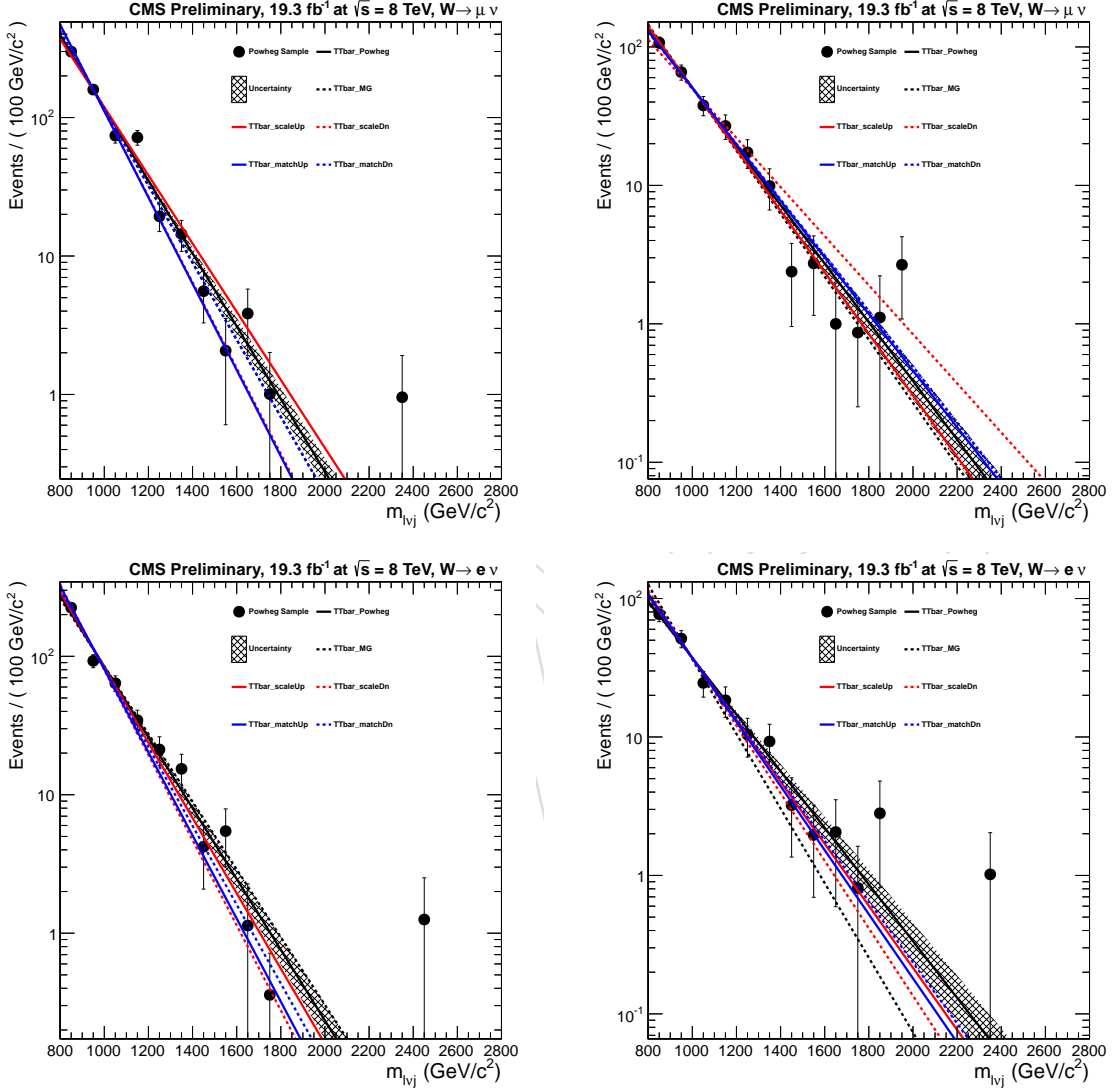


Figure 36: Shape variations in the  $t\bar{t}$  for events with  $m_{lvj} \in [0.7-2.8]$  TeV. Top plots refer to the muon channel: left high purity category  $m_{lvJ}$ , right low purity one. Bottom plots refer to electron channel: left high purity category  $m_{lvJ}$ , right low purity one.

### 6.2.1 Parton Shower Model Uncertainty

The parton shower model used in the simulation is known to not agree well with data [17]. In particular, this affects in a different way the  $W$ -tagging efficiency measured in data and MC; for this reason this is corrected using a scale factor between data and MC, as reported in Sec. 5.3. Thus, the Monte Carlo yields are corrected for this difference. Remaining residual uncertainties are added in quadrature to the efficiency uncertainty, both in data and MC. For the  $W$ -tag working point used to define the high purity category ( $\tau_2/\tau_1 < 0.5$ ), the uncertainty is approximately 9–12% and is reflected in Table 9.

### 6.2.2 Jet Energy Scale Effect on Background Normalization

The CA8 jets are corrected using the AK7 dedicated corrections. The systematic uncertainty is estimated by varying up and down the jet energy uncertainties and computing the effect on the mean jet mass in the  $t\bar{t}$  control sample.

Additional uncertainties are added in quadrature to the AK7 jet uncertainties in order to account for the CA8 jets. In order to compute this additional uncertainty, we take signal MC samples and matching AK7 jets to CA8 jets, the fractional difference between them can be taken as an additional uncertainty. The matching is done for AK7 and CA8 collections for events passing pre-selection criteria and matched within  $\Delta R < 0.3$ . The fractional difference is computed as a function of  $p_T$  and  $\eta$  and it is fitted with a Gaussian function. In the top left and right plots of Fig. 37, we show the fitted mean and sigma of the fractional difference between matched AK7 and CA8 jets as a function of the jet  $\eta$ . In the bottom left and right of Fig. 37, we show the fitted mean and sigma of the fractional difference between the matched AK7 and CA8 jets as a function of the jet  $p_T$ .

From the plots reported in Fig. 37, we find that an additional 2% on the jet energy scale uncertainty, added in quadrature with the computed AK7 corrections, are enough to cover scale differences due to not having dedicated corrections for CA8 jets.

The changing of the expected background yield in the signal region is evaluated separately for each background contribution and is listed in Table 9 for high purity categories, while in Table 10 for low purity ones.

## 6.3 Other systematic on Background Normalization

Additional systematics related to the normalization of expected background yields are:

- The uncertainty from the luminosity is consistent throughout CMS and is taken to be 4.4%.
- The normalization uncertainty for the  $W$ +jet comes from the sideband  $m_j$  fit:

1. Considering  $m_j$  fits for events with  $m_{lvj} \in [0.4-1.3]$  TeV, it is 6.1% (4.2%) for  $\mu$  HP (LP) and 8.7% (5.5%) for el HP (LP).
2. Considering  $m_j$  fits for events with  $m_{lvj} \in [0.7-2.8]$  TeV, it is 4.3% (6.6%) for  $\mu$  HP (LP) and 12.3% (8%) for el HP (LP).

- The normalization uncertainty on the  $t\bar{t}$  comes from the scale factors derived from the  $t\bar{t}$  control sample.
- The normalization uncertainties on the VV and single top are taken from the VHbb analysis [22] fixed at 20% for all the categories.
- In addition, we apply the  $W$ -tagging scale factor to the VV and signal yields, as discussed in Sec. 5.3; its uncertainty is taken as systematic.

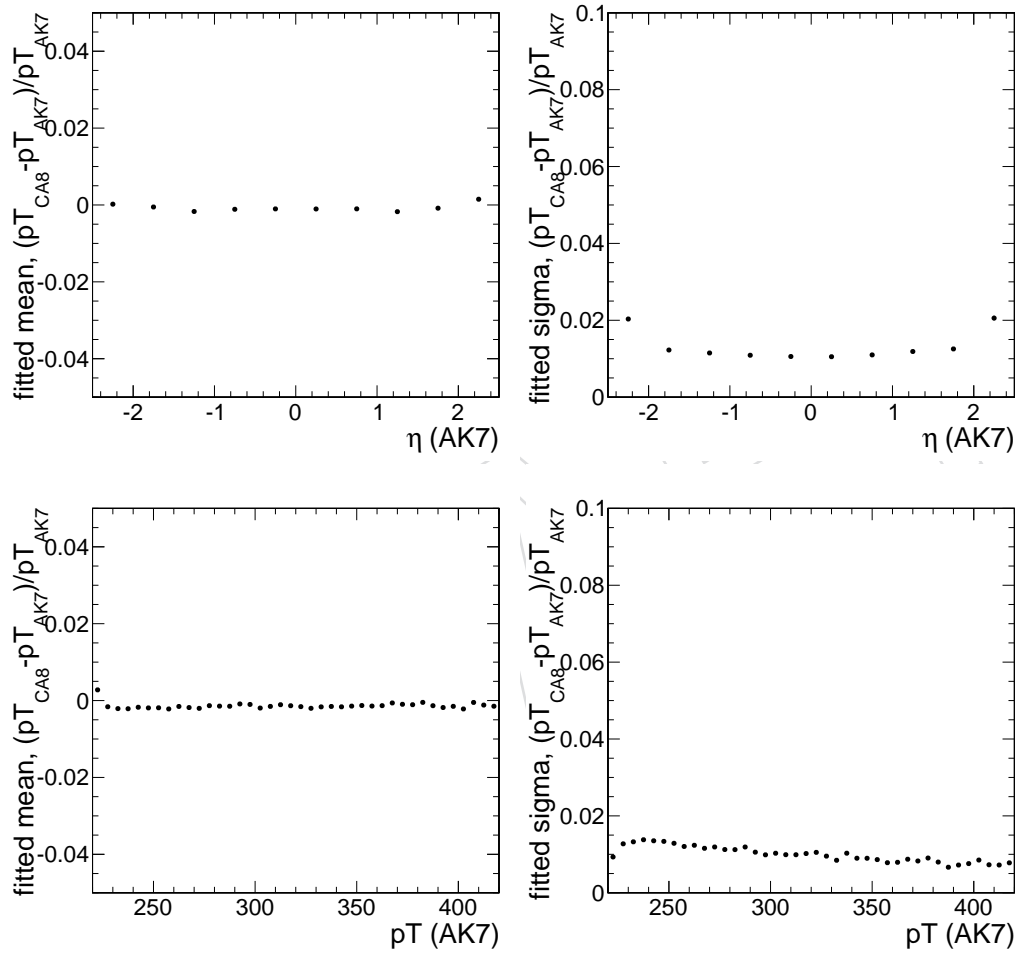


Figure 37: Fitted mean and sigma of the fractional difference between the matched AK7 and CA8 jet  $p_T$ , as a function of jet  $\eta$  (top) and  $p_T$  (bottom).

- 685 • The lepton trigger and identification scale factors are taken from Sec. 3.3. An uncer-  
 686 tainty respectively of 1% (1%) and 1% (3%) is taken for all the background coming  
 687 from simulation for muon (electron) channel.

### 688 6.3.1 Summary of Background Systematics

689 A final summary of all the background systematics considered in the analysis are listed in  
 690 Table 9 and in Table 10, respectively for high purity and low purity category, considering only  
 691 the background extrapolation for events with  $m_{l\nu j} \in [0.7\text{-}2.8] \text{ TeV}$ .

Systematic uncertainty	$W+\text{jets}$	$t\bar{t}$	single top	diboson
Luminosity	-	4.4%	4.4%	4.4%
Background MC cross-section	-	-	20.0%	20%
W-tagging	-	-	-	9% (9%)
$W+\text{jets}$ normalization	4.3% (12.3%)	-	-	-
$t\bar{t}$ normalization	-	3.4% (6%)	3.4% (6%)	-
$W+\text{jets}$ shape	See Sec. 6.1.1	-	-	-
$t\bar{t}$ shape	-	See Sec. 6.2	-	-
Trigger	-	1% (1%)	1% (1%)	1% (1%)
Lepton Selection	-	1% (3%)	1% (3%)	1% (3%)
Jet Energy Scale (JES)	-	1.9% (1.3%)	1% (3.8%)	0.1% (0.9%)

Table 9: Summary of the systematic uncertainties related to the normalization of the expected background yields for muon and (electron) HP categories.

Systematic uncertainty	$W+\text{jets}$	$t\bar{t}$	single top	diboson
Luminosity	-	4.4%	4.4%	4.4%
Background MC cross-section	-	-	20.0%	20%
W-tagging	-	-	-	27% (27%)
$W+\text{jets}$ normalization	5.5% (8%)	-	-	-
$t\bar{t}$ normalization	-	6% (8.2%)	6% (8.2%)	-
$W+\text{jets}$ shape	See Sec. 6.1.1	-	-	-
$t\bar{t}$ shape	-	See Sec. 6.2	-	-
Trigger	-	1% (1%)	1% (1%)	1% (1%)
Lepton Selection	-	1% (3%)	1% (3%)	1% (3%)
Jet Energy Scale (JES)	-	2.3% (1.3%)	7.2% (8.4%)	0.8% (1.2%)

Table 10: Summary of the systematic uncertainties related to the normalization of the expected background yields for muon and (electron) LP categories.

## 692 6.4 Signal Normalization and Shape

693 There are a lot of possible systematic uncertainty sources affecting the number of expected sig-  
 694 nals events, as well as the signal lineshape, after the whole set of the analysis selection. These un-  
 695 certainties are evaluated taking together high purity and low purity signal events; this should  
 696 not introduce any bias since the HP category is the dominant one in the expected sensitivity.

697 Three systematic sources, affecting just the signal normalization, are in common with the back-  
 698 ground ones:

- 699 • Luminosity: is taken to be 4.4%.
- 700 • Trigger and lepton identification: an uncertainty of 1% is assigned to the trigger effi-  
701 ciency for both  $\mu$  and electron channels, while, for the lepton id, the systematic is set  
702 to 1% (3%) for  $\mu$  (el).
- 703 • W-tagger: the uncertainty on the W-tagging efficiency is propagating to the signal  
704 one, as already done for the WW/WZ background.

#### 705 6.4.1 Lepton Energy Scale

706 The uncertainty on lepton energy scale is correlated with the obtained signal efficiency. Muon  
707 energy is scaled up and down by 0.2%, while the electron one is scaled by 0.6%, according to  
708 what indicated by muon and egamma POG. This change in the lepton momentum is prop-  
709 agated to the reconstructed  $E_T^{\text{miss}}$ , and finally the entire analysis is re-run on this new signal  
710 sample. The relative variation in the number of the selected signal events is taken as systematic  
711 uncertainty on signal normalization; for the muon case it is equal to 0.7%, while it is 0.2% for  
712 the electron one.

713 In addition, fitting the nominal signal lineshape and the scaled ones, the observed variation of  
714 the peak position (mean of the  $m_{WW}$  distribution) and its width (RMS of the  $m_{WW}$  distribution)  
715 is added as systematic uncertainty on the fitted signal shape. For the muon case, the uncertain-  
716 ties on the mean and on the width are inflated, respectively, by 0.1% and 0.5%, while, for the  
717 electron channel, they are enlarged both by 0.1%.

#### 718 6.4.2 Lepton Energy Resolution

719 The uncertainty on lepton energy resolution affects the measured signal efficiency. In particular,  
720 muon energy is smeared by 0.6%, while the electron one by 1.4% according to the HEEP team  
721 recommendations. Again, this change is propagated to the  $E_T^{\text{miss}}$  and then the entire analysis is  
722 re-run on this new signal sample. The relative variation in the number of selected signal events  
723 is taken as systematic uncertainty on signal normalization; for both electron and muon cases, it  
724 is equal to 0.1%.

725 In addition, fitting the nominal signal lineshape and the smeared ones, the observed variation  
726 of the peak position (mean of the  $m_{WW}$  distribution) and its width (RMS of the  $m_{WW}$  distribu-  
727 tion) is added as systematic uncertainty on the fitted signal shape. For both electron and muon  
728 cases, the uncertainty on the mean and on the width are inflated by 0.1%.

#### 729 6.4.3 Jet Energy Scale

730 As we already explain for the lepton case, the effect of the uncertainty on the jet energy scale  
731 must be evaluated on the signal efficiency. Thus, CA8 jet energy is scaled up and down accord-  
732 ing to the uncertainty of the JEC set contained in the considered global tag. At the same time,  
733 also AK5 jets are scaled coherently in the same direction; the changes are propagated to the  
734  $E_T^{\text{miss}}$  and then the entire analysis is re-run on this new signal sample. The relative variation in  
735 the number of the selected signal events is taken as systematic uncertainty on signal normal-  
736 ization. The resulting uncertainty depends linearly on the resonance mass [21] for both muon  
737 and electron channels.

738 In addition, fitting the nominal signal lineshape and the scaled ones, the observed variation of  
739 the peak position (mean of the  $m_{WW}$  distribution) and its width (RMS of the  $m_{WW}$  distribution)  
740 is added as systematic uncertainty on the fitted signal shape. For both electron and muon cases,

741 the uncertainty on the mean is flat at 1.3% wrt the resonance mass, while the uncertainty on the  
 742 width is strongly mass dependent (between 1% and 3%).

#### 743 6.4.4 Jet Energy Resolution

744 The uncertainty on jet energy resolution affects the measured signal efficiency. CA8 jet energy is  
 745 smeared according to data/MC scale factors for the jet energy resolution, following the recom-  
 746 mendations of the JetMet group<sup>8</sup>. Also the energy of all the jets in the AK5 collection is smeared  
 747 and these changes are propagated to the  $E_T^{\text{miss}}$ ; finally the entire analysis is re-run on this new  
 748 signal sample. The relative variation in the number of the selected signal events is taken as  
 749 systematic uncertainty on the signal normalization; for both muon and electron channel, this is  
 750 equal to 0.3%.

751 In addition, fitting the nominal signal lineshape and the smeared ones, the observed variation  
 752 of the peak position (mean of the  $m_{WW}$  distribution) and its width (RMS of the  $m_{WW}$  distribu-  
 753 tion) is added as systematic uncertainty on the fitted signal shape. For both electron and muon  
 754 cases, the uncertainty on the mean is at 0.1% level, while the uncertainty on the width is around  
 755 3% for all the mass hypotheses.

#### 756 6.4.5 $E_T^{\text{miss}}$ Scale and Resolution

Uncertainties on energy/momentum scale and resolution for leptons (electron and muon) and jets are propagated to the measured missing energy for each event, introducing an uncertainty on the signal efficiency. The formula used for the  $E_T^{\text{miss}}$  variation is:

$$\vec{E}_T^{\text{miss}}(\text{corr}) = \vec{E}_T^{\text{miss}} + \sum_i^{\text{objects}} [\vec{p}_T^i - \vec{p}_T^i(\text{corr})] \quad (20)$$

757 where `corr` stands for the new missing energy obtained after the objects, lepton or jets, correc-  
 758 tion.

759 In this way, the effect of missing energy scale and resolution has been already taken into ac-  
 760 count when we studied the effect on the signal yield and  $m_{WW}$  shape of each independent  
 761 source, as described in the previous sub-sections.

#### 762 6.4.6 b-tag identification efficiency

763 B-tag scale factors for CSV algorithm medium working point are used in the analysis in order  
 764 to calculate an event weight for each simulated event. These weights can be scaled up and  
 765 down according to scale factor uncertainties, depending on jet  $p_T$ ,  $\eta$  and flavour. The relative  
 766 variation in the number of the selected signal events is taken as systematic uncertainty on signal  
 767 normalization; for both muon and electron channel, this is equal to 0.2%.

768 No significant effect is seen on the signal lineshape; the mean and the width of the  $m_{WW}$  distri-  
 769 bution are not affected varying the b-tag weights.

#### 770 6.4.7 Theoretical Uncertainty on Bulk Graviton Cross Section

771 For the moment, the uncertainty on the expected signal yield, taking into account cross section  
 772 dependence on QCD renormalization/factorization scales and on the proton set of PDFs, are  
 773 still not calculated and not included in the limit procedure.

<sup>8</sup><https://twiki.cern.ch/twiki/bin/view/CMS/JetResolution>.

<sup>774</sup> **6.4.8 Summary of Signal Systematics**

<sup>775</sup> A summary of all the signal systematics are listed in Table 11, taking into account that they are  
<sup>776</sup> evaluated summing together HP and LP events.

Systematic uncertainty	Signal Normalization	Mean $m_{WW}$ Shape	Width $m_{WW}$ Shape
Muon Energy Scale	0.7%	0.1%	0.5%
Electron Energy Scale	0.2%	0.1%	0.1%
Jet Energy Scale	[1%-3%]	1.3%	[2%-3%]
Muon Energy Resolution	0.1%	0.1%	0.1%
Electron Energy Resolution	0.1%	0.1%	0.1%
Jet Energy Resolution	0.3%	0.1%	3%
Unclustered Energy Scale	0.1%	0.%	[1%-3%]
Luminosity	4.4%	-	-
Trigger	1% (1%)	-	-
Lepton Selection	1% (3%)	-	-
W-tagging	HP: 9% LP: (27%)	-	-
b-tag selection	0.2%	-	-
Pile-Up modelling	0.5%	-	-

Table 11: Summary of the signal systematic uncertainties and their impact on the event yield in the signal region and on the reconstructed  $m_{WW}$  shape (mean and width) for both muon and electron channels.

## 7 Statistical Interpretation

### 7.1 Blinding Policy

In order to remain unbiased, we adopt the policy to blind the jet mass distribution in the signal region as well as the  $m_{\ell\nu J}$  distribution. *We have unblinded the analysis on May 6, 2013.*

### 7.2 Upper Limits for Bulk Graviton Production

Upper limits are produced via an unbinned shape analysis, using the Higgs combination tool [24]; a cross-check is performed using a cut-and-count analysis.

The adopted signal shapes are described in Sec. 5.5, while background shapes are described in Sec. 5.4. We have tested 19 different mass point scanning the mass range  $m_G \in [0.6, 2.5]$  TeV at regular steps of 100 GeV. For signal masses where there was no generated MC sample, we estimated signal shape and efficiency interpolating the corresponding quantities from the neighbouring points. Systematic effects are given in Sec. 6, they are treated as nuisance parameters and profiled in the statistical interpretation. The input shapes going into the unbinned shape analysis are shown in Fig. 31 and in Fig. 32.

To extract cut-and-count limits, a loosely optimized window in the four-body mass  $m_{\ell\nu j}$  is selected and all the input shapes are integrated to get the expected yields. For all the mass point listed in Table 2, a mass window of 100 GeV around the nominal value has been chosen.

#### 7.2.1 Limits for full 2012 dataset

The presented limits are obtained processing all the samples with our own framework, as well as all the results shown in the previous sections. On the contrary, the final result of this analysis will be presented in the PAS using group 1 trees [21] in order to be fully synchronized. An extract of the result that will be presented in the pas are presented in the Sec. 8.2.

Expected upper limits are presented for  $19.3 \text{ fb}^{-1}$ , representing the full dataset for 2012. Cut-and-count limits are not shown but, as already said, they have been used to cross check the unbinned shape results.

Since non significant excess is observed, we first set 95% C.L. exclusion limits on the Graviton production cross section times the branching ratio fraction of  $G \rightarrow WW$ , fixing the coupling strength  $\tilde{k} = 0.2$  and  $0.5$ .

Unbinned upper limits are shown in Fig. 38, obtained using Asymptotic  $CL_s$  method [25], for the electron (bottom line) and muon (top line) channels and independently for each category: high purity category on the left column, low purity on the right. Finally, in Fig. 39, the combined limit using all the four categories is presented. The achieved sensitivity is sufficient to exclude the bulk graviton production, in narrow width approximation, below 700 GeV with  $\tilde{k} = 0.5$ .

In order to assess quantitatively the significance of possible excesses above 700 GeV, observed in the  $m_{WW}$  spectrum, one can look at the p-value as a function of the graviton mass. The p-value is defined as the probability for the background-only hypothesis to fluctuate by the same amount, or more, of the observed data. Low p-values indicate large incompatibilities with the background-only hypothesis.

In Fig. 41, observed p-values are presented independently for each channel (muon on top, electron on bottom) and each category (HP left column, LP right one), while, in Fig. 40, the p-value related to the combination among all the categories is shown. The most significant excess is at  $2.56 \sigma$  located only in the muon HP channel, in the range  $1.8 \text{ TeV} < m_{WW} < 2 \text{ TeV}$ . An

excess at 1.8 TeV of  $1.61\sigma$  is also present in the muon LP category, as shown again in Fig. 41. At low mass, there are two excesses located at 600 GeV respectively of  $1.60\sigma$  in the electron LP channel and of  $2.05\sigma$  in the muon HP one. Considering the combined p-value, there are three interesting local excesses: at 600 GeV there is a local excess of  $2.20\sigma$ , at 1.9 TeV there is an excess of  $1.50\sigma$ , as shown by Fig. 40, while, between 2.3 and 2.4 TeV, it is at the level of  $1.91\sigma$ .

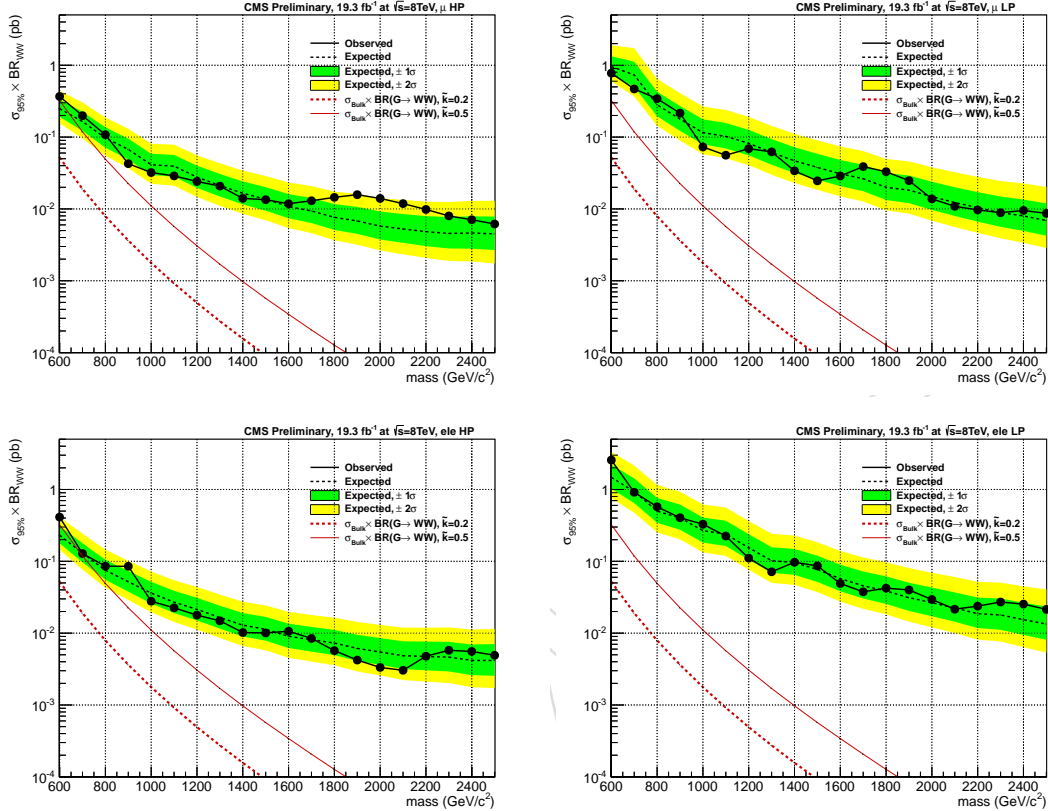


Figure 38: Observed (solid) and expected (dashed) 95% CL upper limit on graviton production cross section times the branching fraction of  $G \rightarrow WW$  using  $19.3 \text{ fb}^{-1}$  of data. The limit is obtained with the Asymptotic  $CL_s$  technique. The 68% and 95% ranges of expectation are also shown with green and yellow bands. The expected product between the Bulk graviton production cross section and the branching fraction is shown as a red dashed (solid) curve for  $\tilde{k} = 0.2$  ( $\tilde{k} = 0.5$ ). Top panel: results for muon channel, HP category on the left, LP on the right. Bottom panel: results for electron channel, HP category on the left, LP on the right.

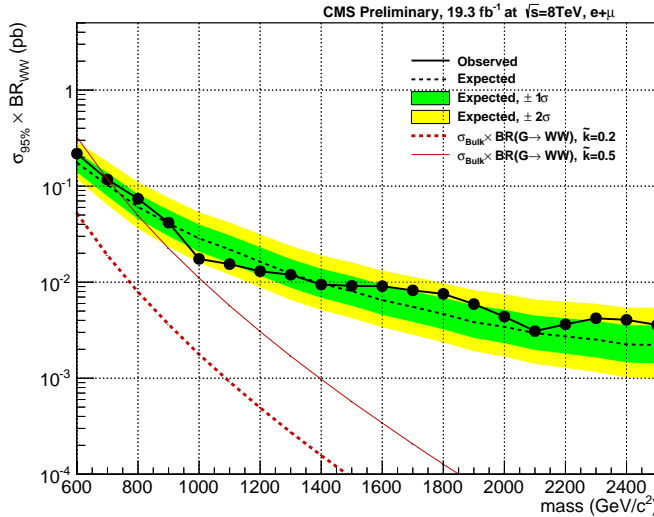


Figure 39: Observed (solid) and expected (dashed) 95% CL upper limit on the graviton production cross section times the branching fraction of  $G \rightarrow WW$  using  $19.3 \text{ fb}^{-1}$  of data. The limit is obtained with the Asymptotic  $CL_s$  technique. The 68% and 95% ranges of expectation are also shown with green and yellow bands. The expected product between the Bulk graviton production cross section and the branching fraction is shown as a red dashed (solid) curve for  $\tilde{k} = 0.2$  ( $\tilde{k} = 0.5$ ).

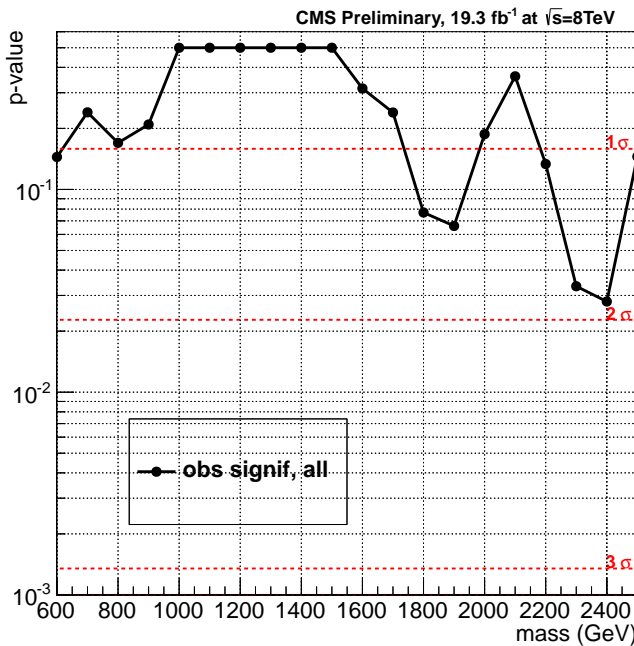


Figure 40: Observed p-values as a function of the nominal signal mass (black dots and solid black line) using  $19.3 \text{ fb}^{-1}$  of data. Conversions of the p-value to number of standard deviations of a two-tail Gaussian are drawn as dashed horizontal red lines.

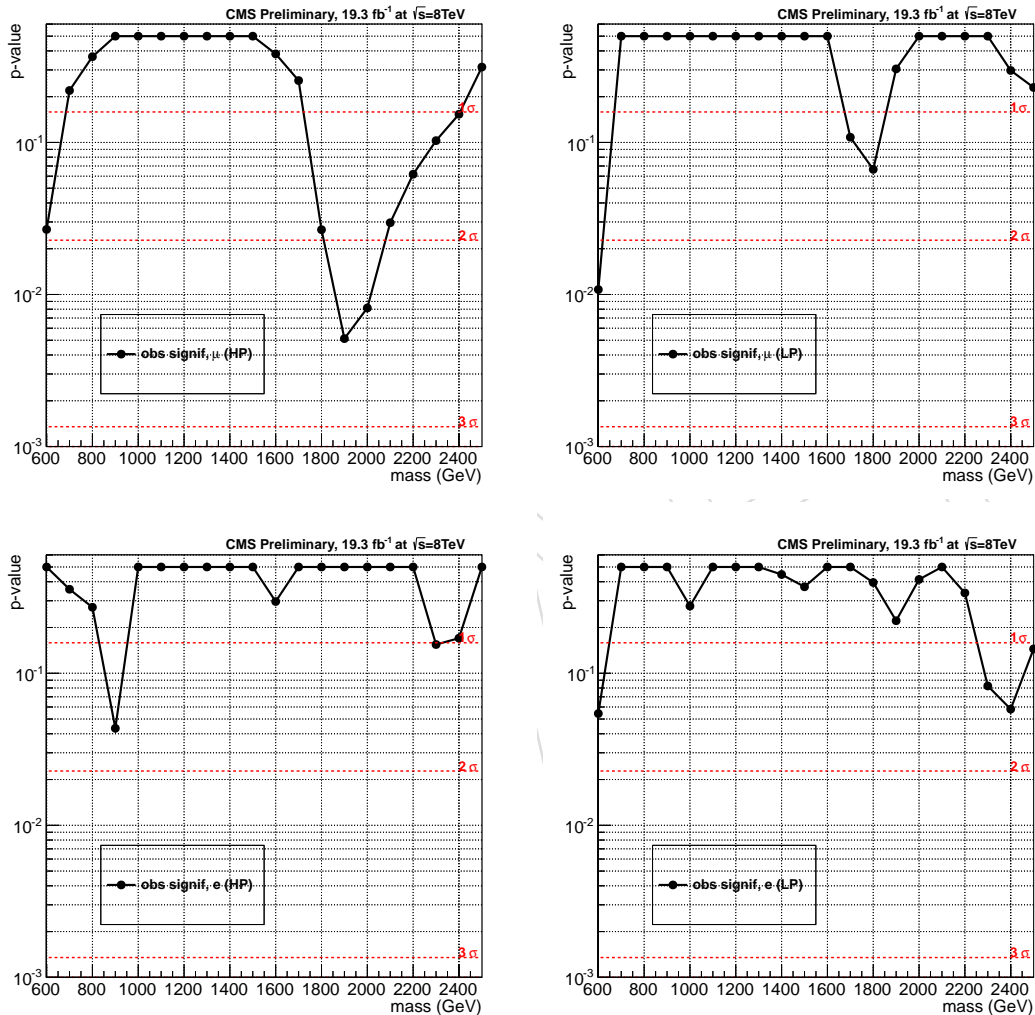


Figure 41: Observed p-values as a function of the nominal signal mass (black dots and solid black line) using  $19.3 \text{ fb}^{-1}$  of data presented individually for the categories muon HP (top left), muon LP (top right), electron HP (bottom left) and electron LP (bottom right).

## 8 Final Result Reported in the PAS

In this section, we present the final result obtained processing the samples provided by group1 framework [21], that are used to derive the results that will be reported in the final official PAS (**EXO-12-021**).

The analysis strategy is exactly the same of the one exposed in the previous chapters; the only difference between the two frameworks, which brings to a difference of 5% in the event yield in the signal region, stands in the type-I correction applied to the  $E_T^{miss}$ . This creates a bias in both the missing transverse energy absolute value, in its direction  $\phi$  in the transverse plane and in the final invariant mass  $m_{l\nu j}$ .

### 8.1 Control Region $t\bar{t}$

In this section, we report the scale factors obtained in the  $t\bar{t}$  control region, following the same procedures described in Sec.5.3, running the analysis on the ntuples provided by group1.

As already explained, in order to fix the normalization for  $t\bar{t}$  and single top contributions in the analysis signal region, we apply all the cuts used to define the  $t\bar{t}$  control region, stated in Sec. 5.3.1. Then, looking only inside the jet mass signal region ( $m_j \in [65-105]$  GeV) and applying the N-subjettiness  $\tau_2/\tau_1$  selection, we account for the difference after the  $\tau_2/\tau_1$  cut, to get the data/MC scale factor for both low purity ( $\tau_2/\tau_1 \in [0.5, 0.75]$ ) and high purity category ( $\tau_2/\tau_1 < 0.5$ ). Results are listed given in Table 12.

Signal window	$\mu$ SF High Purity	$e$ SF High Purity	$\mu$ SF low Purity	$e$ SF Low Purity
65-105 GeV	$0.96 \pm 0.02$	$0.97 \pm 0.03$	$1.23 \pm 0.05$	$1.30 \pm 0.07$

Table 12:  $t\bar{t}$  and single top data/MC scale factor "SF" for both muon and electron channel, low purity and high purity category.

For the W-tagger efficiency, replying the same procedure described in Sec. 5.3.2, we get for the high purity working point:

$$\begin{cases} \epsilon(dat, \mu) = 0.657 \pm 0.056 \\ \epsilon(sim, \mu) = 0.736 \pm 0.049 \end{cases} \Rightarrow SF_{HP}(\mu) = 0.892 \pm 0.097 \quad (21)$$

$$\begin{cases} \epsilon(dat, el) = 0.759 \pm 0.074 \\ \epsilon(sim, el) = 0.756 \pm 0.065 \end{cases} \Rightarrow SF_{HP}(el) = 1.004 \pm 0.131 \quad (22)$$

which are fully compatible, within the statistical uncertainty, with the ones reported in Eq.8. Since we are interested in a scale factor just for real hadronic Ws, assuming that the leptons don't have a big impact on the SF measurement, we can combine muon and electron channel results into one single scale factor through a weighted average:

$$SF_{HP}(\text{combined}) = 0.93 \pm 0.08 \quad (23)$$

Fit results are shown in Fig. 42. In the upper line muon channel results are reported: (left) pass sample, (right) fail one; while, in the bottom line, the same plots are replied for the electron case.

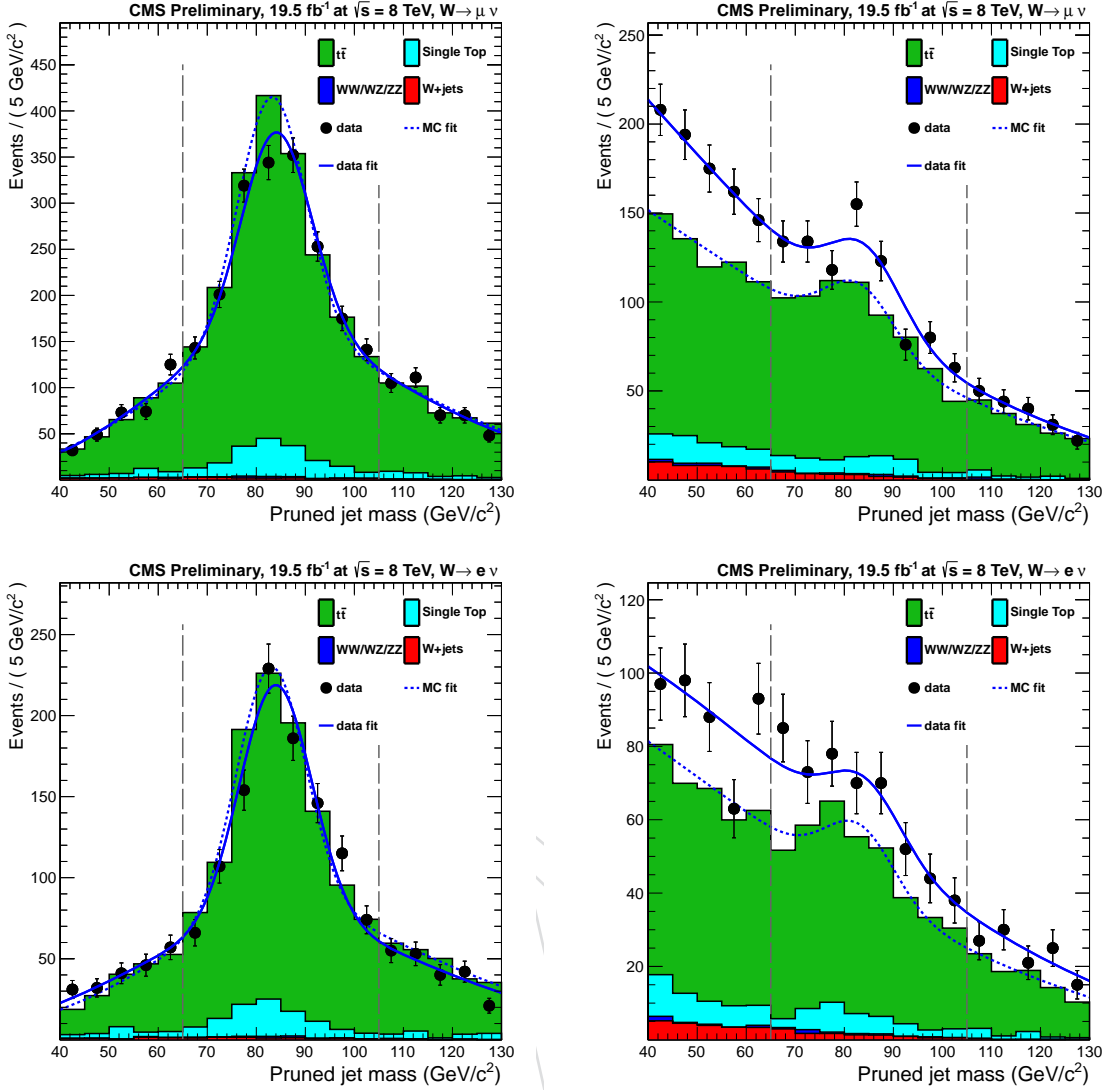


Figure 42: Pruned jet mass distribution in the  $t\bar{t}$  control sample passing(left) and failing (right) the high purity  $W$ -tag cut. Upper line the muon channel fits, bottom line the electron ones.

848 Fitting the failing samples ( $\tau_2/\tau_1 > 0.75$ ) with a pdf given by the sum of two exponential, one  
 849 for the fail-matched sample and another for the fail-unmatched one, we get:

$$\begin{cases} \epsilon_{fail}(dat, \mu) = 0.001 \pm 0.046 \\ \epsilon_{fail}(sim, \mu) = 0.000 \pm 0.028 \end{cases} \quad \begin{cases} \epsilon_{fail}(dat, el) = 0.031 \pm 0.054 \\ \epsilon_{fail}(sim, el) = 0.000 \pm 0.029 \end{cases} \quad (24)$$

850 Finally, thanks to Eq. 10, the LP scale factors can be extracted:

$$\begin{cases} \epsilon_{LP}(data, \mu) = 0.343 \pm 0.078 \\ \epsilon_{LP}(MC, \mu) = 0.263 \pm 0.056 \end{cases} \Rightarrow SF_{LP}(\mu) = 1.302 \pm 0.405 \quad (25)$$

$$\begin{cases} \epsilon_{LP}(data, el) = 0.209 \pm 0.088 \\ \epsilon_{LP}(MC, el) = 0.243 \pm 0.072 \end{cases} \Rightarrow SF_{LP}(el) = 0.863 \pm 0.442 \quad (26)$$

Again, these values for LP category are compatible, within the statistical uncertainty, with the

ones reported in Eq.12. The weighted mean between electron and muon channel is given by:

$$SF_{LP}(\text{combined}) = 1.10 \pm 0.30 \quad (27)$$

851 The extracted W mass peak position and resolution are:

$$\langle m \rangle_{\text{sim}} = 83.2 \pm 0.3 \text{ GeV}, \sigma_{\text{sim}} = 7.1 \pm 0.4 \text{ GeV} \quad (28)$$

$$\langle m \rangle_{\text{dat}} = 84.4 \pm 0.4 \text{ GeV}, \sigma_{\text{dat}} = 7.4 \pm 0.6 \text{ GeV} \quad (29)$$

852 We find that both the W-jet mass scale and resolution in data are greater than the one coming  
 853 from the simulation. We will shift the MC mean by +1.16 GeV and enlarge the MC sigma by  
 854 4.2% in the analysis to correct for this observed difference between data and MC.

## 855 8.2 W+Jets Background Extraction

856 As already described in Sec.5.4, considering the  $m_j$  spectrum, shapes and normalizations of the  
 857 non-dominant backgrounds are fixed to what is obtained from the MC; while, the normalization  
 858 of the W+jets contribution is extracted from the fit to the data jet mass distribution in the  
 859 sideband region. These fits are shown in Fig. 43, considering all the events with  $m_{lvj}$  in [0.7-3.0]  
 860 TeV, for the high purity and low purity muon categories (upper line), for low purity and high  
 861 purity electron channel (bottom line). The factor for correcting the simulated W-peak position  
 862 and resolution to the observed data, taken from the  $t\bar{t}$  control sample, are included in the plots  
 863 of Fig.43.

864 The function  $\alpha$  is determined from MC, in order to account for the correlations between the  
 865 jet mass and the mass of the three-body system. We use the Herwig++ determination of the  
 866 function  $\alpha_{\text{MC}}(m_{lvj})$ , as Herwig++ is known to better describe the jet substructure [17]. The  
 867 difference between the Herwig++ and Pythia6 determinations is used as a systematic effect on  
 868 W+jets shape related to the adopted parton shower model; this will be described in more detail  
 869 later.

870 For the fit function, the  $F_{\text{ExpN}}(m_{lvj})$ , defined in Eq. 18, is taken as default shape when W+jets  
 871 spectrum is fitted in the range between [0.7-3.0] TeV, while the  $F_{\text{ExpTail}}(m_{lvj})$  is used as alter-  
 872 native function to evaluate shape systematics. The reason of this choice is explained in the  
 873 appendix A.

874 The shapes of the  $\alpha$  functions can be seen in Fig. 44 for both muon and electron channels, high  
 875 and low purity categories, fitting the W+jets in the mass range  $m_{lvj} \in [0.7-3.0]$  TeV.

876 Using the fit in the lower  $m_j$  sideband region from Fig. 43, we can get the shape of the W+jets in  
 877  $m_{lvj}$  in the lower sideband region from data,  $F_{\text{data,LSB}}(m_{lvj})$ . We must also fit the contribution of  
 878 the non-dominant backgrounds both in the sideband and signal regions in  $m_{lvj}$ , as well again  
 879 fixing their normalizations and shapes from MC. Since also the  $m_{WW}$  shape is dependent on  
 880 both the  $m_j$  region of fit and on the  $m_{lvj}$  range of fit, the chosen shapes are listed in Table 6.

881 The fits for  $F_{\text{data,LSB}}(m_{lvj})$  is shown in Fig. 45; again upper line refers to the muon channel, high  
 882 purity on the left, low purity on the right, while the bottom line shows the electron channel  
 883 results. The uncertainties on the fits are also included in the plot, based on the parametric  
 884 errors estimation.

885 In in Fig.46, the extrapolated background in the  $m_{lvj}$  spectrum, inside the signal region, is  
 886 shown for both electron (bottom) and muon (top) channels, high purity (left) and low purity  
 887 (right) categories, considering the extrapolation for events with  $m_{lvj} \in [0.7-3.0]$  TeV.

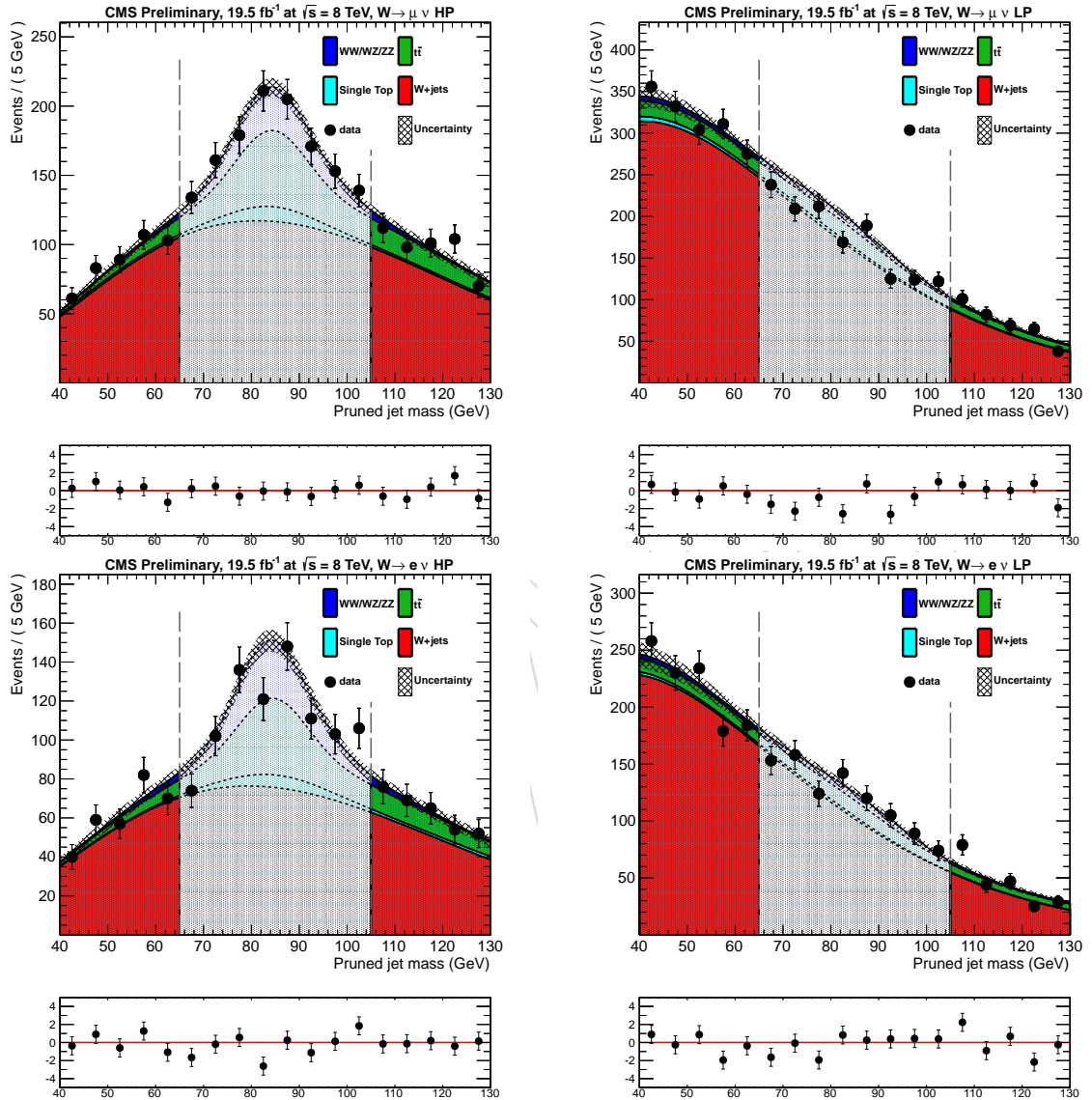


Figure 43: Fits to extract the relative shape and normalization of the  $W+jets$  contribution from the data in the jet mass distribution, taking only the events with  $m_{l\nu j}$  in [0.7-3.0] TeV. Top line fits for the muon channel: high purity (left) and low purity (right) category. Bottom line fits for the electron channel: high purity (left) and low purity (right) category.

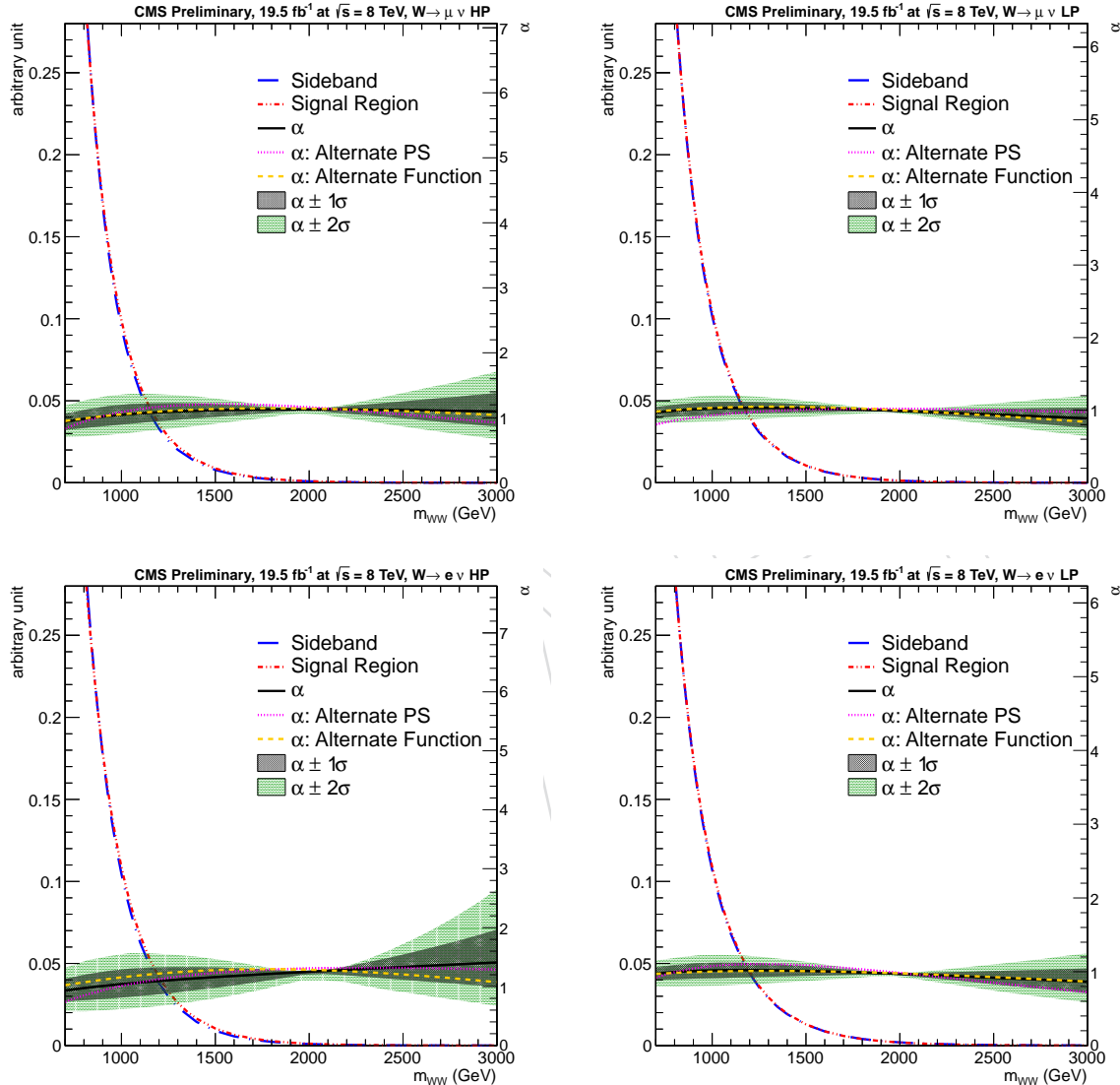


Figure 44: The functions  $\alpha_{MC}(m_{Wj})$  for the  $\mu$  high purity category (top left),  $\mu$  low purity (top right), electron high purity (bottom left) and electron low purity (bottom right), obtained fitting the MC  $W+jets$  background between [0.7-3.0] TeV.

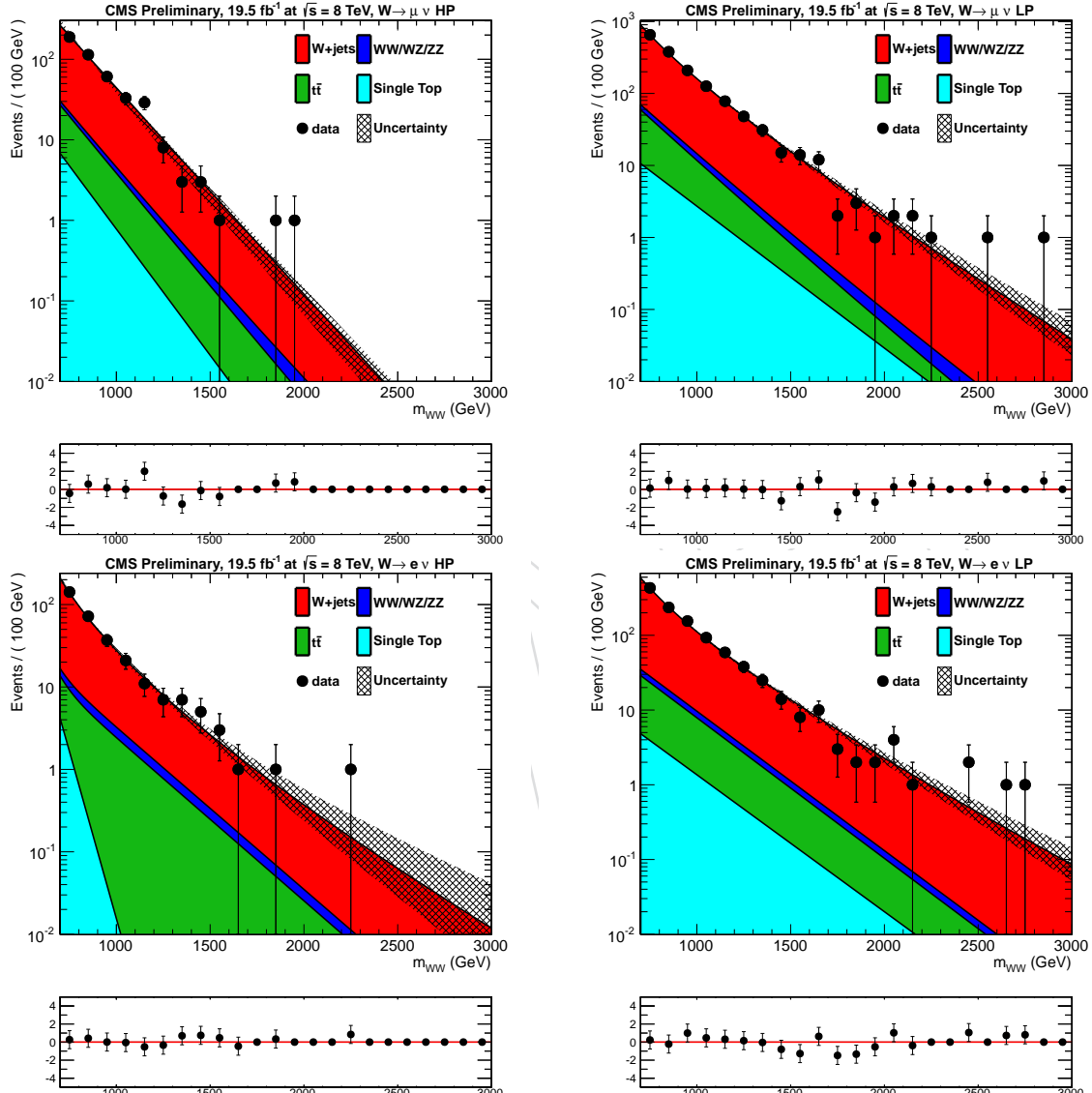


Figure 45: The fits for  $F_{\text{data},\text{LSB}}(m_{lvj})$  for both electron (bottom) and muon (top) channels, high purity (left) and low purity (right) categories, taking into account events with  $m_{lvj}$  between [0.7-3.0] TeV.

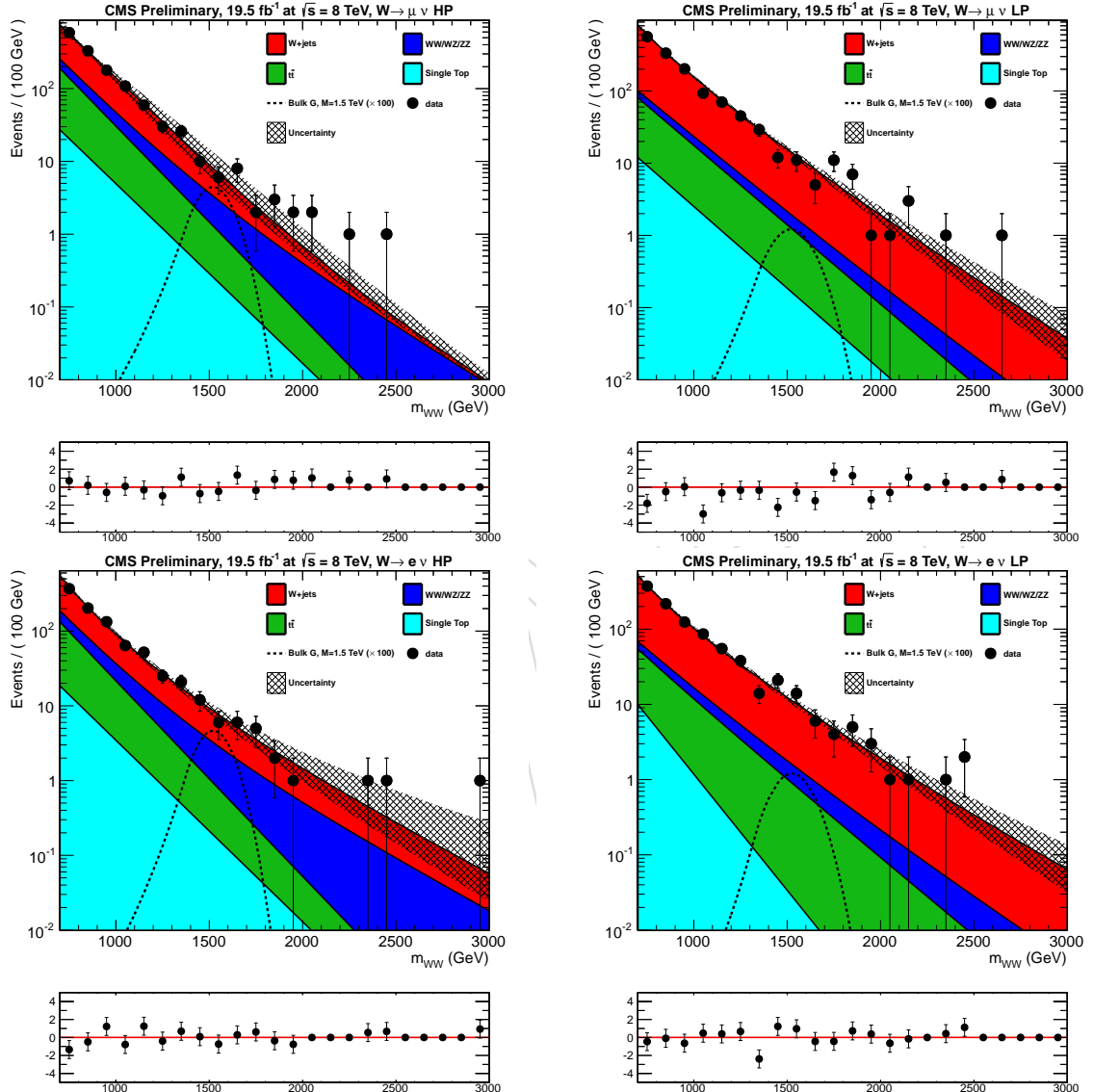


Figure 46: Final distributions in  $m_{l\nu j}$  for data and the expected backgrounds in electron+jet final state (bottom) and muon (top) channel, for events with  $m_{l\nu j}$  between [0.7-3.0] TeV. Left, high purity category ( $\tau_2/\tau_1 < 0.5$ ); right, low purity category ( $\tau_2/\tau_1 \in [0.5, 0.75]$ ).

- 888 Unbinned upper limits are shown in Fig. 47, obtained using Asymptotic  $CL_s$  method [25], for  
889 the electron (bottom line) and muon (top line) channels and independently for each category:  
890 high purity category on the left column, low purity on the right. Finally, in Fig. 48, the com-  
891 bined limit using all the four categories is presented. The achieved sensitivity is not sufficient  
892 to exclude the bulk graviton production, in narrow width approximation, above 800 GeV with  
893  $\tilde{k} = 0.5$  or  $\tilde{k} = 0.2$ .
- 894 In order to assess quantitatively the significance of possible excesses above 800 GeV, observed  
895 in the  $m_{WW}$  spectrum, one can look at the p-value as a function of the mass. The p-value is de-  
896 fined as the probability for the background-only hypothesis to fluctuate by the same amount, or  
897 more, of the observed data. Low p-values indicate large incompatibilities with the background-  
898 only hypothesis.
- 899 In Fig. 50, observed p-values are presented independently for each channel (muon on top,  
900 electron on bottom) and each category (HP left column, LP right one), while, in Fig. 49, the p-  
901 value related to the combination among all the categories is shown. The most significant excess  
902 at  $2.11\sigma$  is located in the muon HP channel, in the range  $1.8 \text{ TeV} < m_{WW} < 2 \text{ TeV}$ . However,  
903 it reduced to  $1.42\sigma$  when we combine all the categories, as shown in Fig. 49. Looking at the  
904 combined p-value, a broad excess of  $1.76\sigma$  is placed in the very high mass region, between 2.2  
905 and 2.5 TeV. In addition, there is a sharp excess of  $0.99\sigma$  at 800 GeV in the combined p-value,  
906 mainly driven an excess in the muon HP channels.
- 907 Finally, in Appedix C, a different set of tests for the limit and p-value extraction have been done,  
908 in order to check: the importance of all the systematics uncertainties and of alpha systematic,  
909 due to alternative parton shower and fitting function models, on the final cross section upper  
910 limit, and robustness of the final analysis results (full  $CL_s$  limit extraction and signal injection).

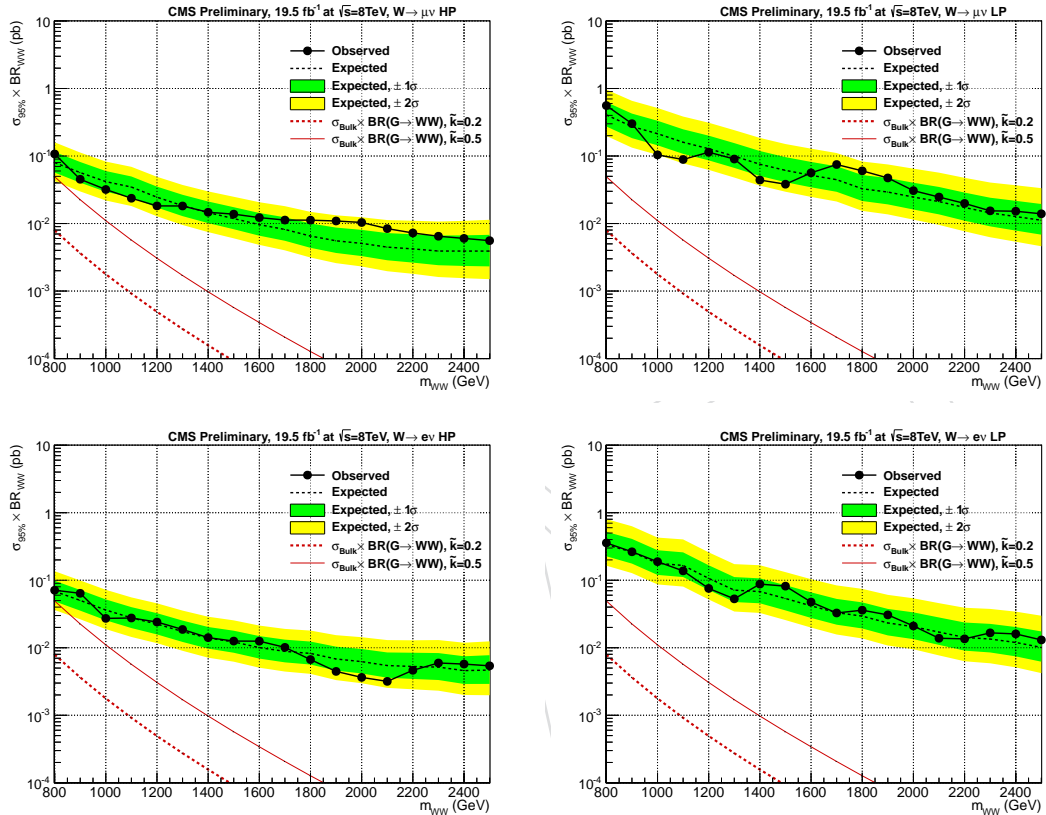


Figure 47: Observed (solid) and expected (dashed) 95% CL upper limit on graviton production cross section times the branching fraction of  $G \rightarrow WW$  using  $19.3 fb^{-1}$  of data. The limit is obtained with the Asymptotic  $CL_s$  technique. The 68% and 95% ranges of expectation are also shown with green and yellow bands. The expected product between the Bulk graviton production cross section and the branching fraction is shown as a red dashed (solid) curve for  $\tilde{k} = 0.2$  ( $\tilde{k} = 0.5$ ). Top panel: results for muon channel, HP category on the left, LP on the right. Bottom panel: results for electron channel, HP category on the left, LP on the right.

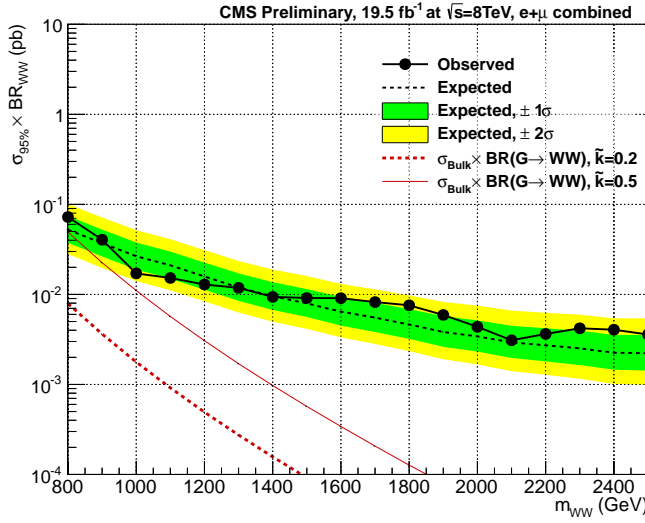


Figure 48: Observed (solid) and expected (dashed) 95% CL upper limit on the graviton production cross section times the branching fraction of  $G \rightarrow WW$  using  $19.3 fb^{-1}$  of data. The limit is obtained with the Asymptotic  $CL_s$  technique. The 68% and 95% ranges of expectation are also shown with green and yellow bands. The expected product between the Bulk graviton production cross section and the branching fraction is shown as a red dashed (solid) curve for  $\bar{k} = 0.2$  ( $\bar{k} = 0.5$ ).

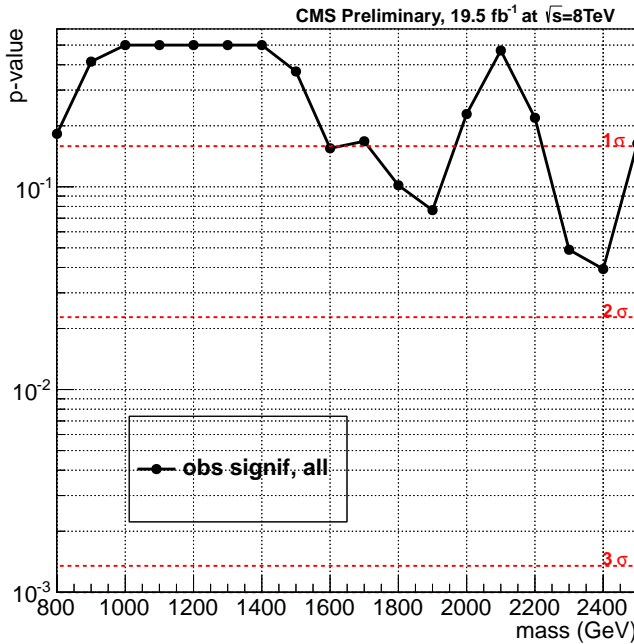


Figure 49: Observed p-values as a function of the nominal signal mass (black dots and solid black line) sing  $19.3 fb^{-1}$  of data. Conversions of the p-value to number of standard deviations of a two-tail Gaussian are drawn as dashed horizontal red lines.

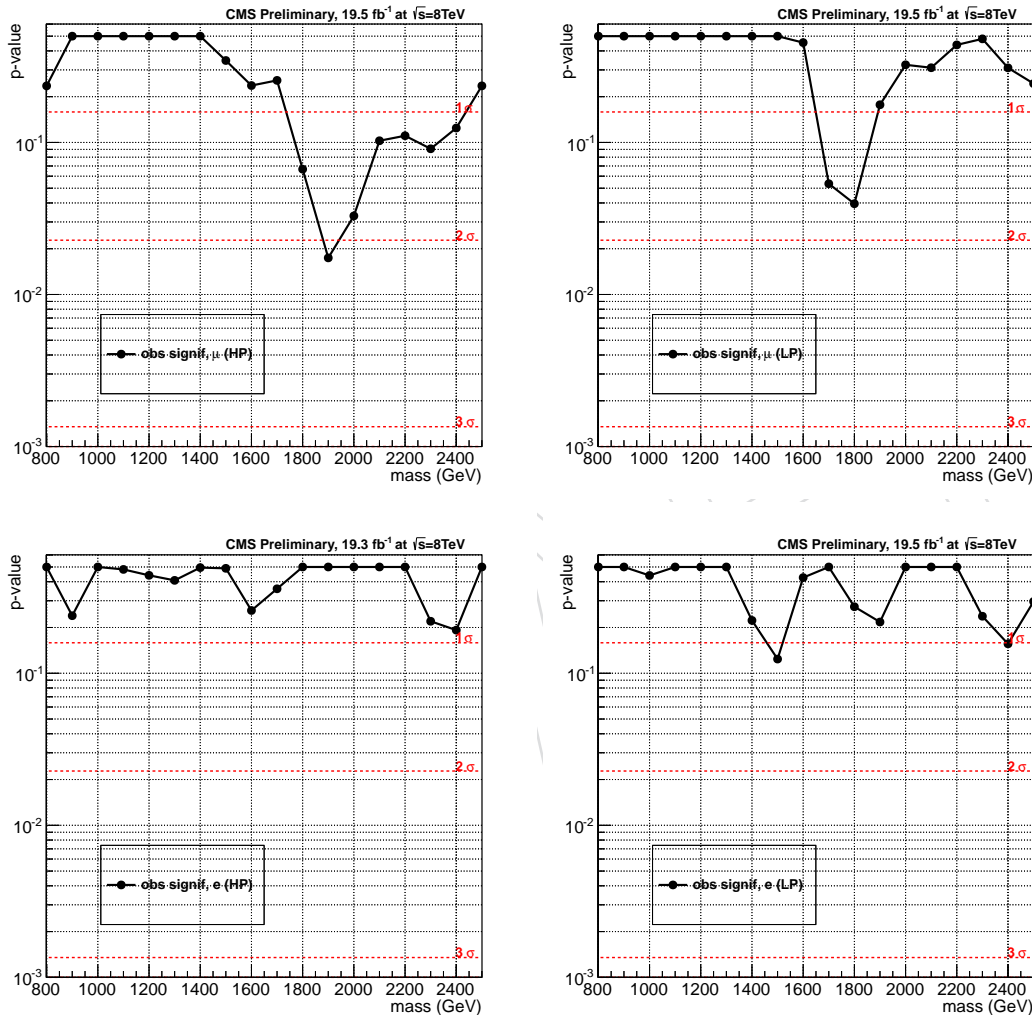


Figure 50: Observed p-values as a function of the nominal signal mass (black dots and solid black line) using  $19.3 \text{ fb}^{-1}$  of data presented individually for the categories muon HP (top left), muon LP (top right), electron HP (bottom left) and electron LP (bottom right).

---

**911 9 Conclusions**

- 912 We performed a search for a graviton decaying to a pair of W bosons in the semi-leptonic final  
913 state, exploiting jet substructure techniques in order to keep high signal efficiency in the W  
914 boosted regime. A categorization based on a kinematic quantity sensitive to the substructure  
915 inside the jet is adopted, in order to enhance the sensitivity of this search. A detailed simula-  
916 tion is used for modelling non-leading backgrounds, as well as the specific benchmark model  
917 for the signal. A data-driven technique is used for estimating the W+jets background in the  
918 signal region, which is the main source of background for the considered topology. A precise  
919 assessment of the systematic uncertainties has been performed.
- 920 No significant excess above the expected background is found in the explored mass range  
921  $0.8 \text{ TeV} < m_G < 2.5 \text{ TeV}$ ; the achieved sensitivity does not allow to exclude the production  
922 of bulk gravitons above 800 GeV, with coupling  $\tilde{k}$  between 0.2 and 0.5.

A large, faint watermark is printed diagonally across the page. It contains the word "DRAFT" in a bold, sans-serif font, with each letter's top stroke pointing towards the bottom-left corner of the page. The watermark is light gray and serves as a draft indicator.

## 923 A Choice of W+jets Fit Function

924 In this section, the studies concerning the choice of the fit function for W+jets background  
 925 estimation, when we look at the  $m_{WW}$  spectrum in the ranges [0.4-1.3] TeV and [0.7-3.0] TeV,  
 926 are reported.

927 This study is performed taking the pure W+jets MC sample (MadGraph+Pythia6), after merging  
 928 the W+jet sample with  $p_T > 100$  GeV and the one with  $p_T > 180$  GeV. Taking the  $m_{lvj}$   
 929 distributions in both the sideband and signal region, after the full analysis selection, we fit  
 930 with different models the W+jets shape for each of the 4 categories (electron HP/LP, muon  
 931 HP/LP). Different models have been tested:

- 932 • In the  $m_{lvj}$  range [0.4-1.3] TeV:  $F_{\text{ErfPowExp}}(m_{lvj})$ ,  $F_{\text{ErfPowPow}}(m_{lvj})$ ,  $F_{\text{ErfExp}}(m_{lvj})$  and  
 933  $F_{\text{ErfPow}}(m_{lvj})$  as defined in Sec. 5.4.
- 934 • In the  $m_{lvj}$  range [0.7-3.0] TeV: two different levelled-exponential functions  $F_{\text{ExpN}}(m_{lvj})$   
 935 and  $F_{\text{ExpTail}}(m_{lvj})$ , defined in Sec. 5.4, a simple exponential function  $F_{\text{Exp}}(m_{lvj})$  and a  
 936 power law  $F_{\text{Pow}}(m_{lvj})$ .

937 The goodness of each fit is evaluated looking at the pull distribution, which is used as discriminant  
 938 to choose which is the best shape for fitting data in the sideband and to extract the  $\alpha$   
 939 function. For simplicity, in the next plots, results for only muon channel are shown, both in the  
 940 sideband and in the signal region and for each fitting function choice.

### 941 A.1 Result in the [0.4-1.3] TeV Range

942 In Fig. 51, results of the W+jets shape fit in the sideband region, for high purity category,  
 943 are shown: top left plot refers to  $F_{\text{ErfPowExp}}(m_{lvj})$  fit, top right to  $F_{\text{ErfExp}}(m_{lvj})$ , bottom left to  
 944  $F_{\text{ErfPowPow}}(m_{lvj})$  and finally, bottom right the  $F_{\text{ErfPow}}(m_{lvj})$  one.

945 On the contrary, in Fig. 52, results of W+jets shape fit in the sideband region, for low purity  
 946 category, are reported: again top left plot refers to  $F_{\text{ErfPowExp}}(m_{lvj})$  fit, top right to  $F_{\text{ErfExp}}(m_{lvj})$ ,  
 947 bottom left to  $F_{\text{ErfPowPow}}(m_{lvj})$  and finally, bottom right the  $F_{\text{ErfPow}}(m_{lvj})$  one.

948 Looking at these results, obtained in the low  $m_{lvj}$  sideband, it is clear that, considering both  
 949 low purity and high purity categories,  $F_{\text{ErfPow}}(m_{lvj})$  and  $F_{\text{ErfExp}}(m_{lvj})$  are not enough to predict  
 950 the W+jets shape. While, the other two with one more degree of freedom ( $F_{\text{ErfPowExp}}(m_{lvj})$  and  
 951  $F_{\text{ErfPowPow}}(m_{lvj})$ ), adopted in the left row plots of Fig. 51 and Fig. 52, reproduce better the  $m_{WW}$   
 952 spectrum in particular around the peak.

953 The same study is performed also fitting the W+jets  $m_{lvj}$  spectrum in the signal region, for both  
 954 high purity (HP) and low purity (LP) categories. Results are shown in Fig. 53 for HP, and in  
 955 Fig. 54 for LP.

956 Also for the signal region, comparing the pull plots, the choice of  $F_{\text{ErfPowExp}}(m_{lvj})$  or  $F_{\text{ErfPowPow}}(m_{lvj})$   
 957 is more consistent with the shape expected from the MC simulation.

### 958 A.2 Result in the [0.7-3.0] TeV Range

959 In Fig. 55, results of W+jets shape fit in the sideband region, for high purity category, are pre-  
 960 sented: top left plot refers to  $F_{\text{ExpN}}(m_{lvj})$  fit, top right to  $F_{\text{ExpTail}}(m_{lvj})$ , bottom left to the single  
 961 exponential  $F_{\text{Exp}}(m_{lvj})$  and finally, bottom right to the power law fit.

962 On the contrary, in Fig. 56, results of W+jets shape fit in the sideband region for low purity  
 963 category: again top left plot refers to  $F_{\text{ExpN}}(m_{lvj})$  fit, top right to  $F_{\text{ExpTail}}(m_{lvj})$ , bottom left to the  
 964 single exponential  $F_{\text{Exp}}(m_{lvj})$  and finally, bottom right to the power law fit.

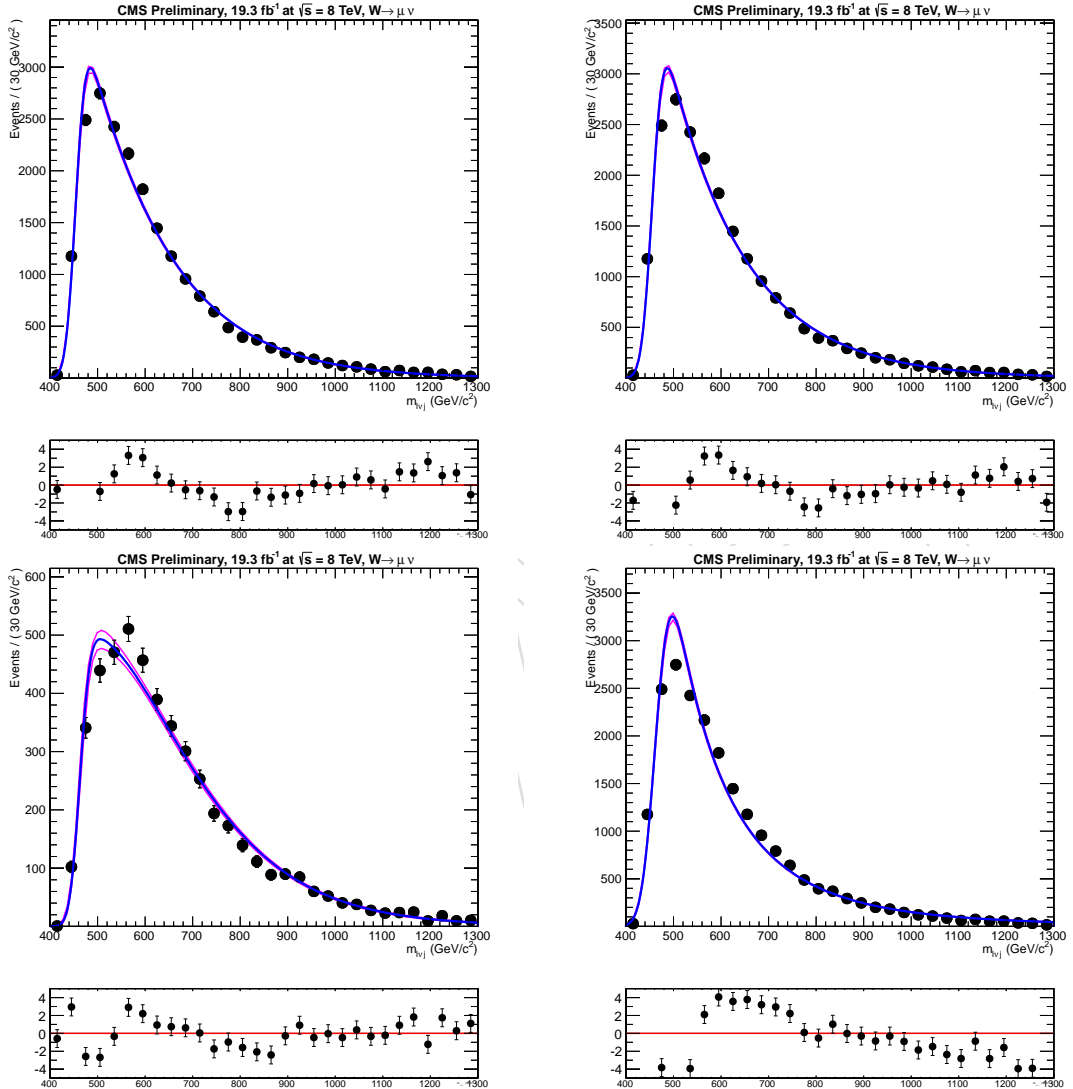


Figure 51:  $m_{lvj}$  fit in the sideband of  $W+jets$  for different shapes, high purity category only: top left plot refers to  $F_{\text{ErfPowExp}}(m_{lvj})$ , top right to  $F_{\text{ErfExp}}(m_{lvj})$ , bottom left to the  $F_{\text{ErfPowPow}}(m_{lvj})$  and bottom right to the  $F_{\text{ErfPow}}(m_{lvj})$ .

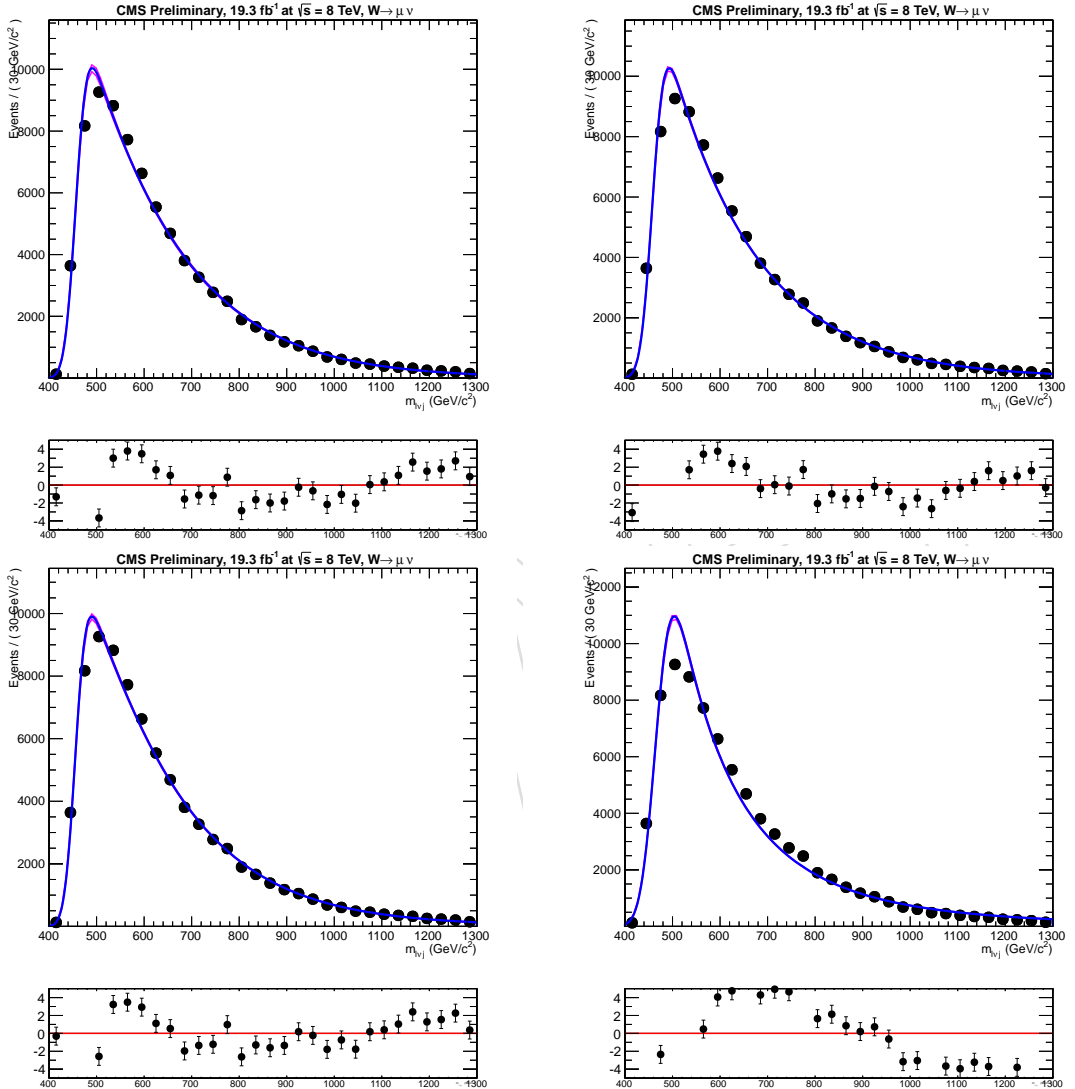


Figure 52:  $m_{\text{lvj}}$  fit in the sideband of W+jets for different shapes, low purity category only: top left plot refers to  $F_{\text{ErfPowExp}}(m_{\text{lvj}})$ , top right to  $F_{\text{ErfExp}}(m_{\text{lvj}})$ , bottom left to the  $F_{\text{ErfPowPow}}(m_{\text{lvj}})$  and bottom right to the  $F_{\text{ErfPow}}(m_{\text{lvj}})$

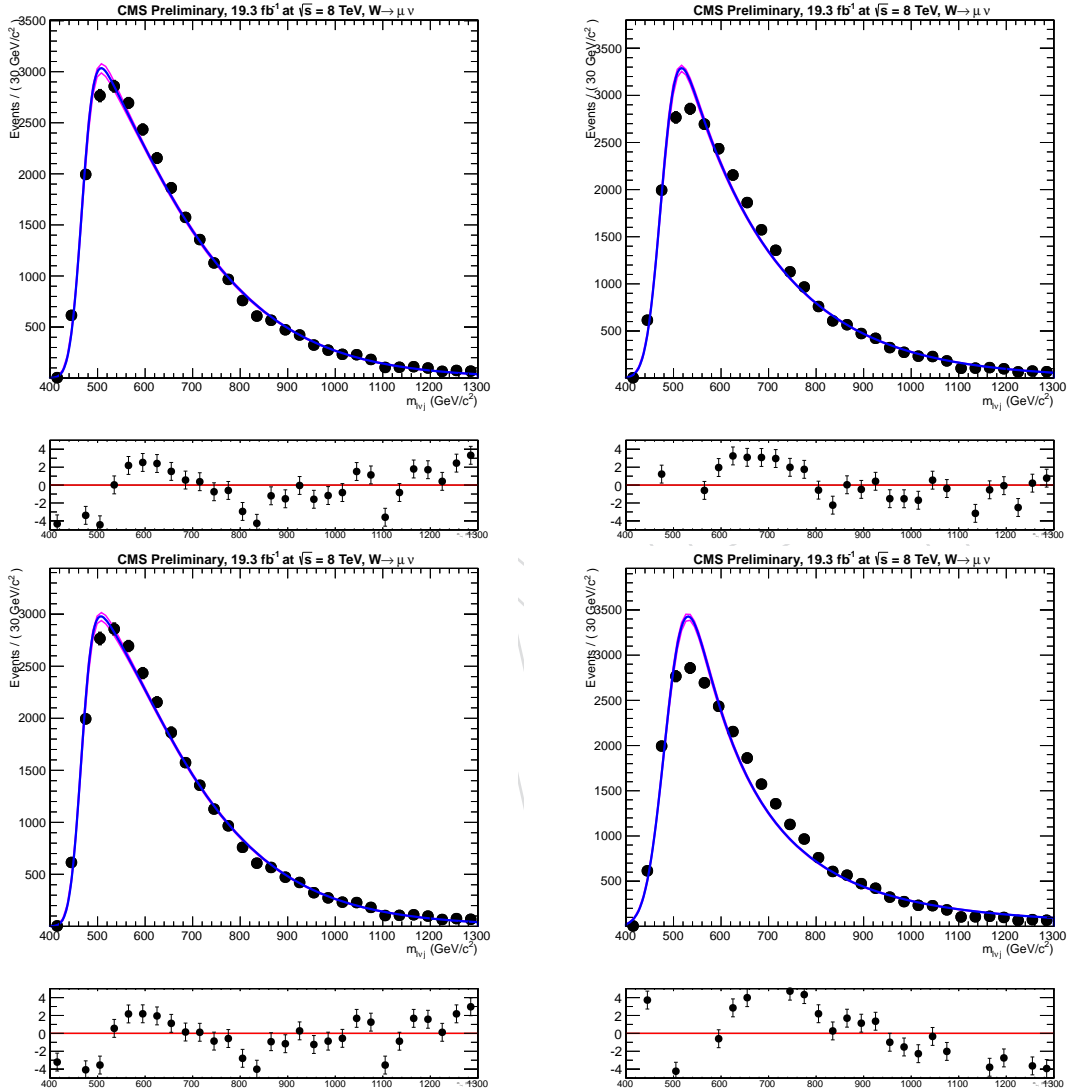


Figure 53:  $m_{lvj}$  fit in the signal region of  $W+jets$  for different shapes, high purity category only: top left plot refers to  $F_{\text{ErfPowExp}}(m_{lvj})$ , top right to  $F_{\text{ErfExp}}(m_{lvj})$ , bottom left to the  $F_{\text{ErfPowPow}}(m_{lvj})$  and bottom right to the  $F_{\text{ErfPow}}(m_{lvj})$

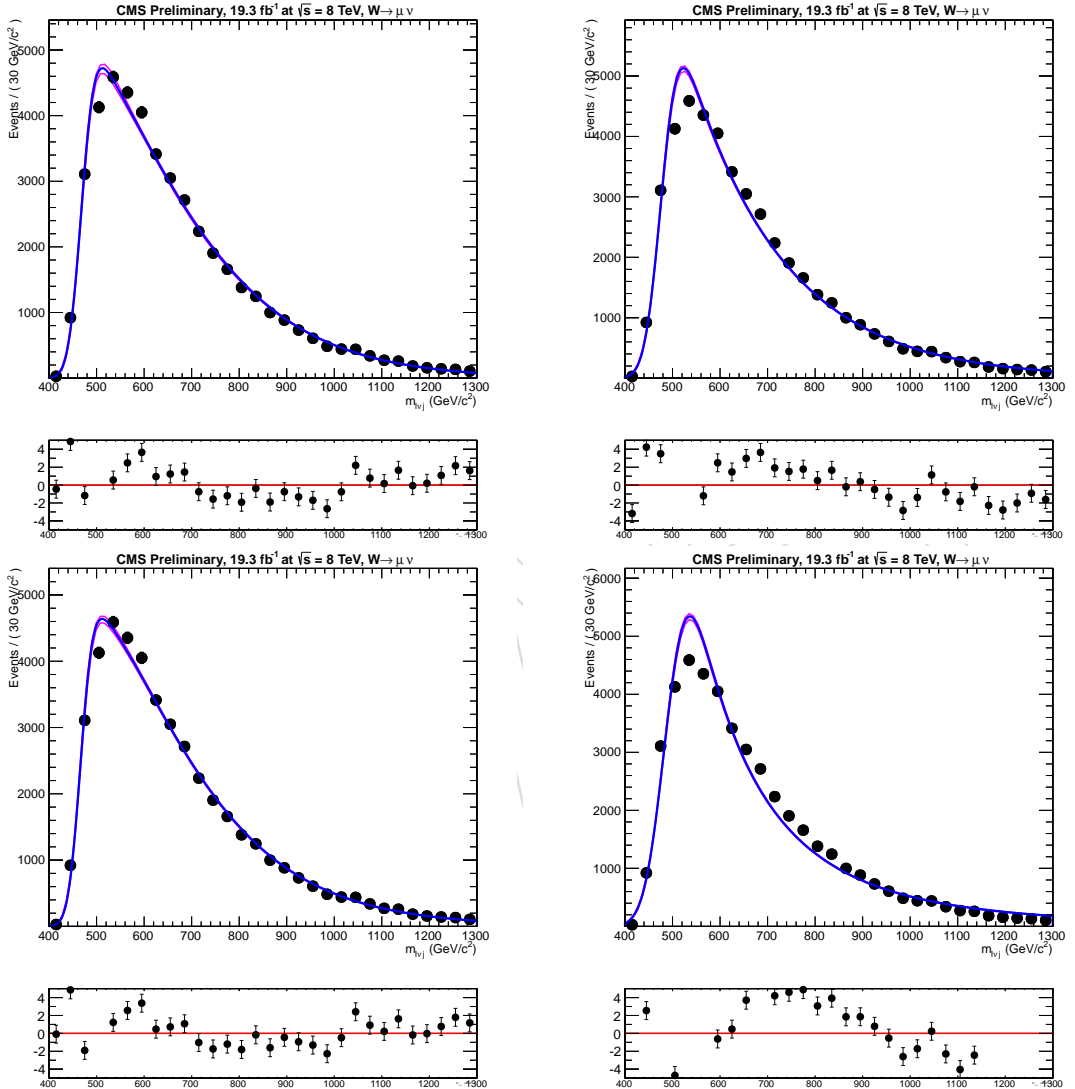


Figure 54:  $m_{l\nu j}$  fit in the signal region of W+jets for different shapes, low purity category only: top left plot refers to  $F_{\text{ErfPowExp}}(m_{l\nu j})$ , top right to  $F_{\text{ErfExp}}(m_{l\nu j})$ , bottom left to the  $F_{\text{ErfPowPow}}(m_{l\nu j})$  and bottom right to the  $F_{\text{ErfPow}}(m_{l\nu j})$

Looking at these results, obtained in the low  $m_{l\nu j}$  sideband, it is clear that, in particular considering the low purity category, a single exponential function or a simple power law are not enough to predict the W+jets shape. While, the levelled exponential functions, adopted in the upper plots of Fig.55 and Fig. 56, reproduce better the  $m_{WW}$  spectrum in particular at high mass.

The same study is performed also fitting the W+jets  $m_{l\nu j}$  spectrum in the signal region, for both high purity (HP) and low purity (LP) categories. Results are shown in Fig. 57 for HP, and in Fig. 58 for LP.

Also for the signal region, comparing the pull plots, the choice of a levelled exponential function,  $F_{\text{ExpN}}(m_{l\nu j})$  or  $F_{\text{ExpTail}}(m_{l\nu j})$ , is more consistent with the shape expected from the MC simulation.

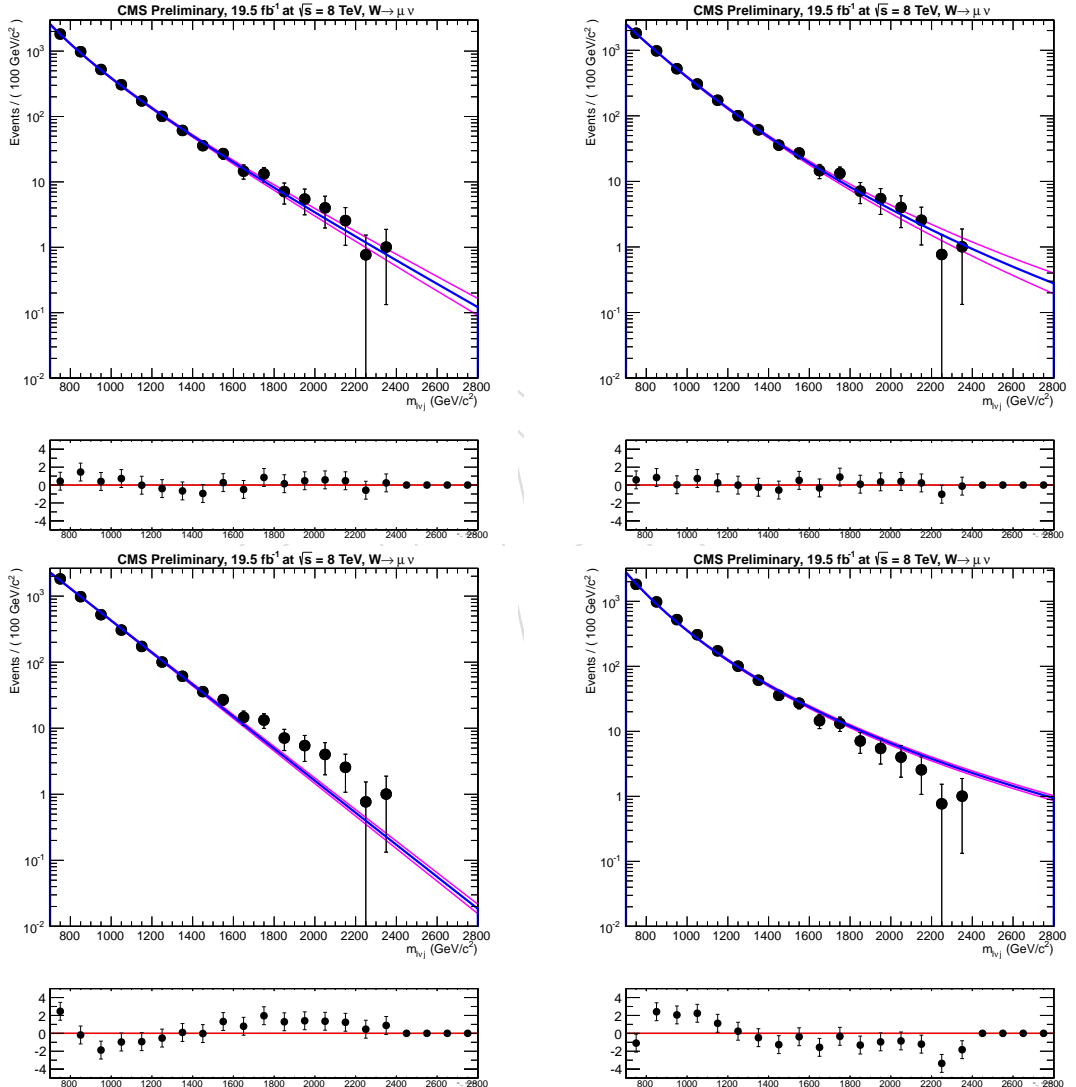


Figure 55:  $m_{l\nu j}$  fit in the sideband of W+jets for different shapes, high purity category only: top left plot refers to  $F_{\text{ExpN}}(m_{l\nu j})$ , top right to  $F_{\text{ExpTail}}(m_{l\nu j})$ , bottom left to the single exponential  $F_{\text{Exp}}(m_{l\nu j})$  and bottom right to the power law fit.

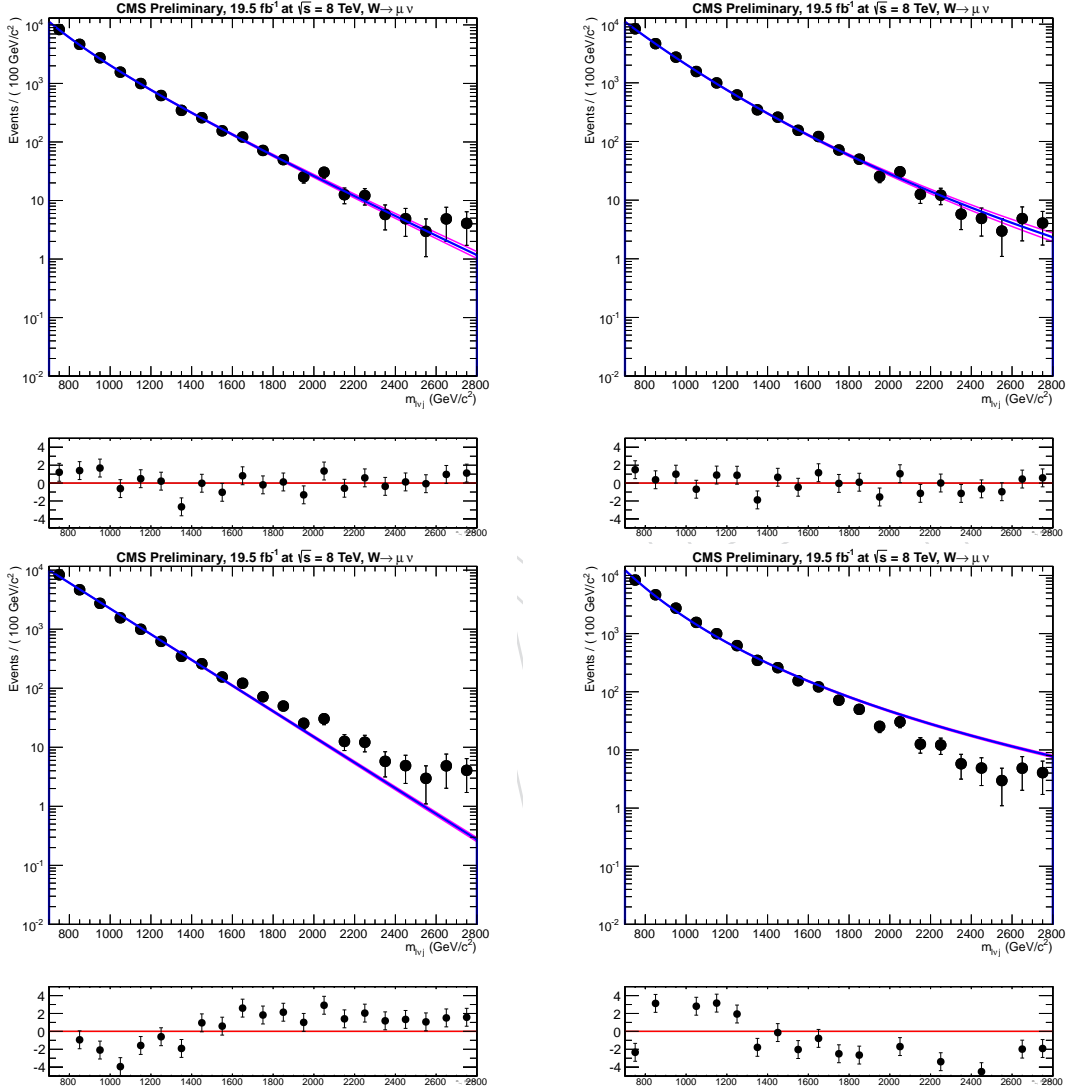


Figure 56:  $m_{\text{lvj}}$  fit in the sideband of W+jets for different shapes, low purity category only: top left plot refers to  $F_{\text{ExpN}}(m_{\text{lvj}})$ , top right to  $F_{\text{ExpTail}}(m_{\text{lvj}})$ , bottom left to the single exponential  $F_{\text{Exp}}(m_{\text{lvj}})$  and bottom right to the power law fit.

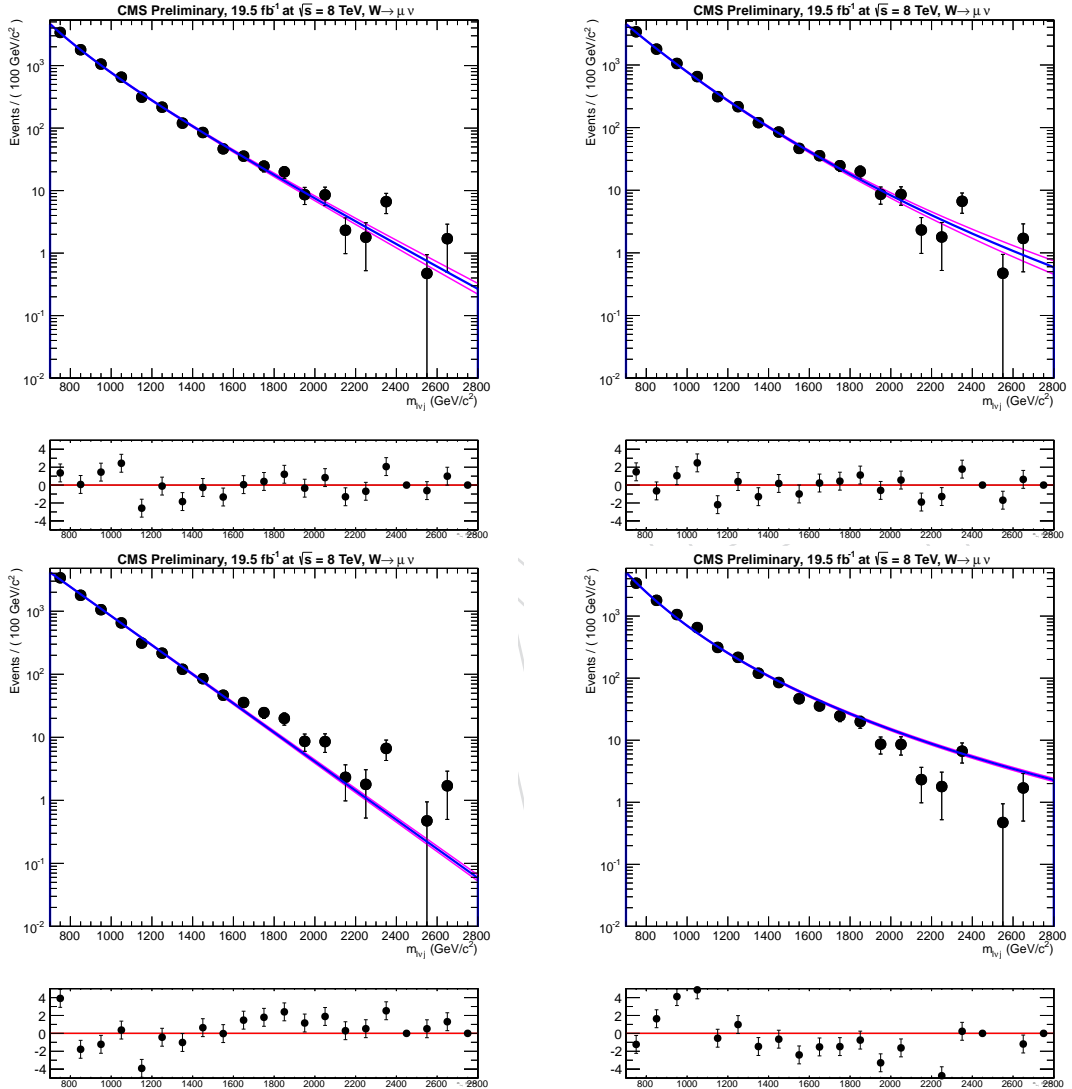


Figure 57:  $m_{lvj}$  fit in the signal region of  $W+\text{jets}$  for different shapes, high purity category only: top left plot refers to  $F_{\text{ExpN}}(m_{lvj})$ , top right to  $F_{\text{ExpTail}}(m_{lvj})$ , bottom left to the single exponential  $F_{\text{Exp}}(m_{lvj})$  and bottom right to the power law fit.

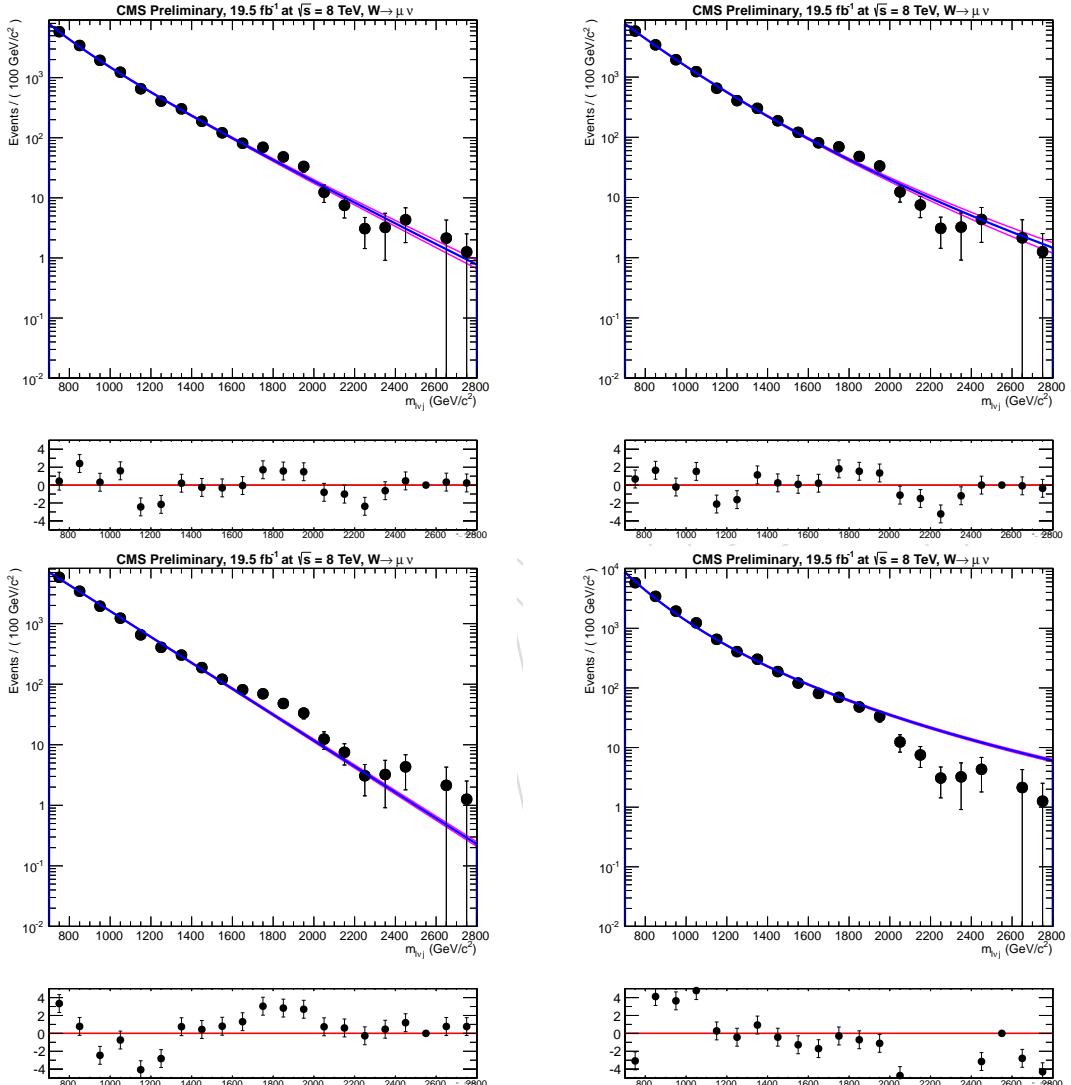


Figure 58:  $m_{lvj}$  fit in the signal region of W+jets for different shapes, low purity category only: top left plot refers to  $F_{\text{ExpN}}(m_{lvj})$ , top right to  $F_{\text{ExpTail}}(m_{lvj})$ , bottom left to the single exponential  $F_{\text{Exp}}(m_{lvj})$  and bottom right to the power law fit.

## 976 **B Closure test for alpha method**

977 We can define two scenarios for closure test the data driven method for W+jets background  
 978 estimation:

- 979 • **A1→A2:**  $m_j \in [40, 55]$  GeV (**A1**) is taken as lower sideband,  $m_j \in [105, 130]$  GeV as  
 980 upper sideband and  $m_j \in [55, 65]$  GeV (**A2**) as signal region.
- 981 • **A →B:**  $m_j \in [40, 65]$  GeV (**A**) is taken as lower sideband,  $m_j \in [115, 130]$  GeV as  
 982 upper sideband and  $m_j \in [100, 115]$  GeV (**B**) as signal region.

983 In the second case, because we need to fit  $M_j$  in lower sideband and upper sideband to extract  
 984 the W+jets yield in signal region, we choose 115 GeV as signal region upper limit. Moreover,  
 985 in order to get more statistics, we set the signal region lower limit to 100 GeV.

### 986 **B.1 Closure Test A1 → A2**

987 In Fig. 59 and Fig. 60, the  $m_j$  fits for the W+jets normalization in the signal region, respectively  
 988 for events with  $m_{l\nu j}$  in [0.4-1.3] TeV and [0.7-3.0] TeV, are presented for both muon (top) and  
 989 electron (bottom) case, high purity (left) and low purity (right) categories.

990 In Fig. 61 and in Fig. 62, the data  $m_{l\nu j}$  fits in the low sideband are reported for each channel and  
 991 each category, respectively for events in the  $m_{l\nu j}$  mass range [0.4-1.3] TeV and [0.7-3.0] TeV. The  
 992 agreement between data and the extracted background shape is consistent for each category  
 993 and for both muon and electron channel.

994 In Fig. 63 and in Fig. 64, the extrapolation function  $\alpha(m_{l\nu j})$ , obtained fitting the W+jet MC in  
 995 both the defined lower sideband and in the signal region, is shown for each channel ( $\mu$  and  $e$ )  
 996 and each category. Again, in Fig. 63 only events with  $m_{l\nu j} \in [0.4-1.3]$  TeV are considered while,  
 997 in Fig. 64,  $m_{l\nu j}$  has to be within [0.7-3.0] TeV.

998 Finally, using the extracted W+jet normalization from fitting data in the  $m_j$  sideband (A1) and  
 999 the shape, derived from fitting data in the sideband of  $m_{l\nu j}$  times the alpha function, in Fig. 65  
 1000 and in Fig. 66, the extracted background prediction can be compared with data in the consid-  
 1001 ered signal region (A2) for each channel ( $\mu$  and  $e$ ) and each category (HP/LP).

1002 Looking at the pull distributions attached to each plot shown in Fig. 65 and in Fig. 66, we  
 1003 can state that a good agreement is found, in each category, between data and the extracted  
 1004 background in a completely signal-free region (A2). Thus, the test closes and the background  
 1005 extraction via the  $\alpha$ -method is validated.

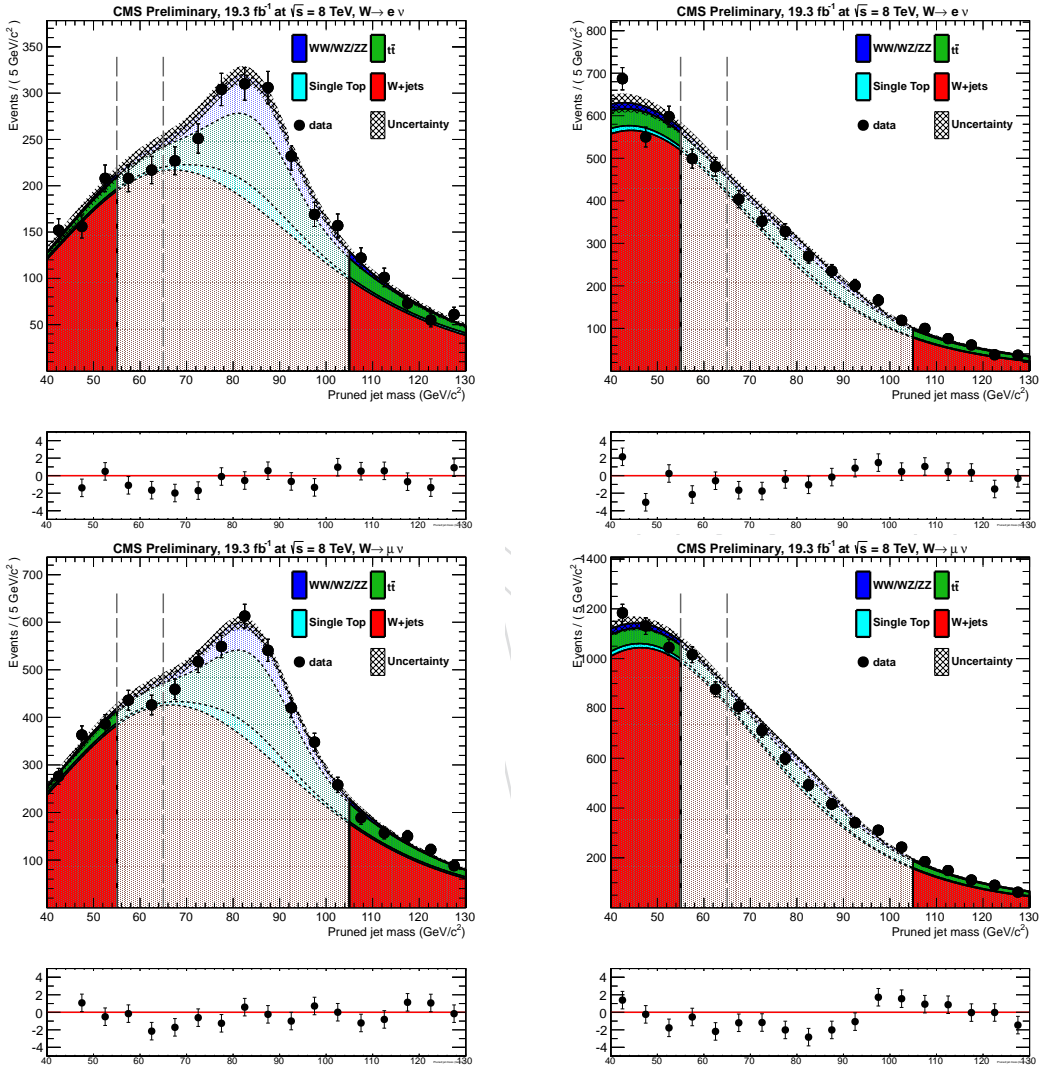


Figure 59: Jet mass  $m_j$  fit in A1→A2 extrapolation for events with  $m_{l\nu j}$  between [0.6-1.3] TeV: (top) muon case, (bottom) electron channel. Left column high purity category, right low purity one.

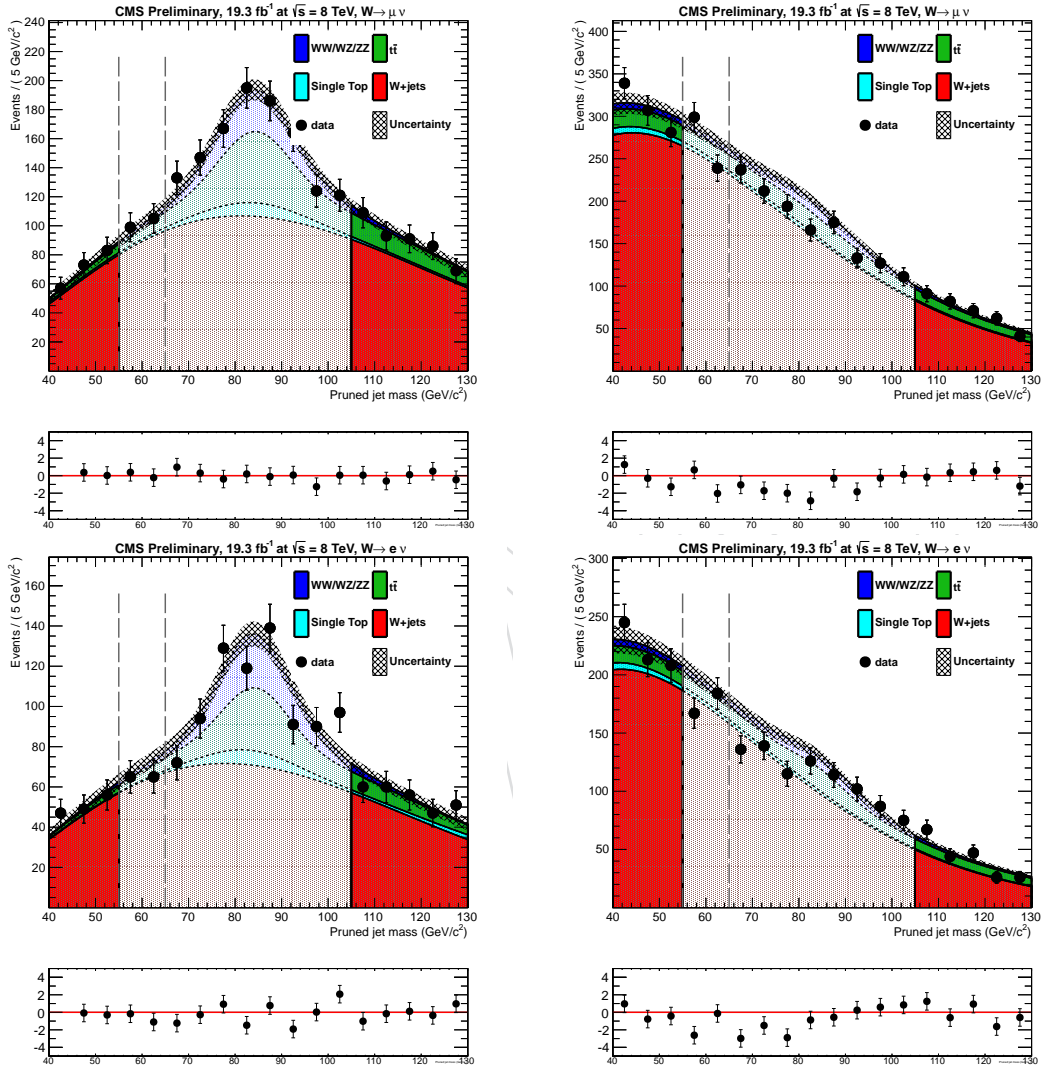


Figure 60: Jet mass  $m_j$  fit in A1  $\rightarrow$  A2 extrapolation for events with  $m_{l\nu j}$  between [0.7-3.0] TeV: (top) muon case, (bottom) electron channel. Left column high purity category, right low purity one.

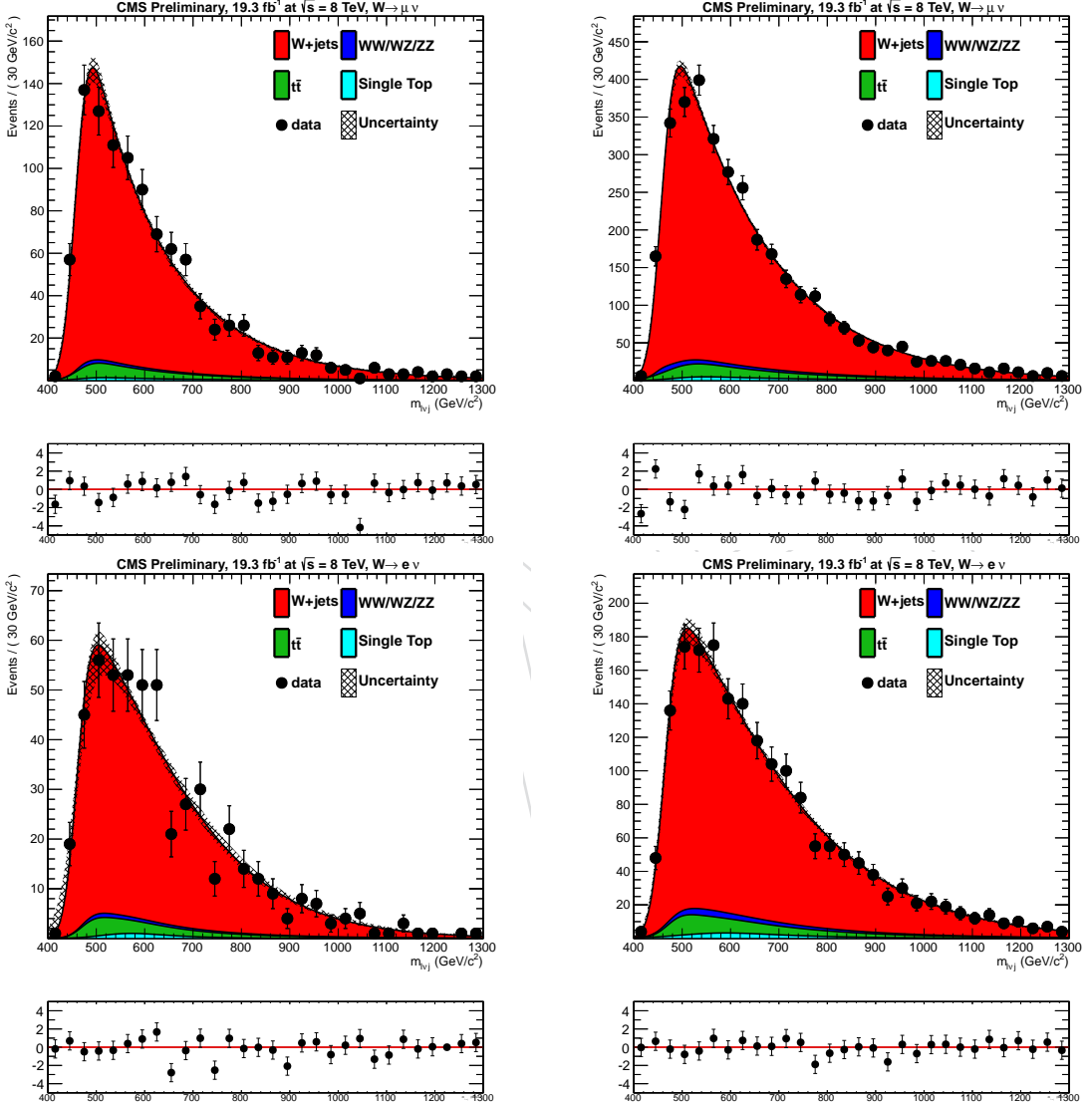


Figure 61:  $m_{lvj}$  sideband fit for  $A1 \rightarrow A2$  extrapolation for events with  $m_{lvj}$  in the range [0.4–1.3] TeV: (top) muon case, (bottom) electron channel. Left column high purity category, right low purity one.

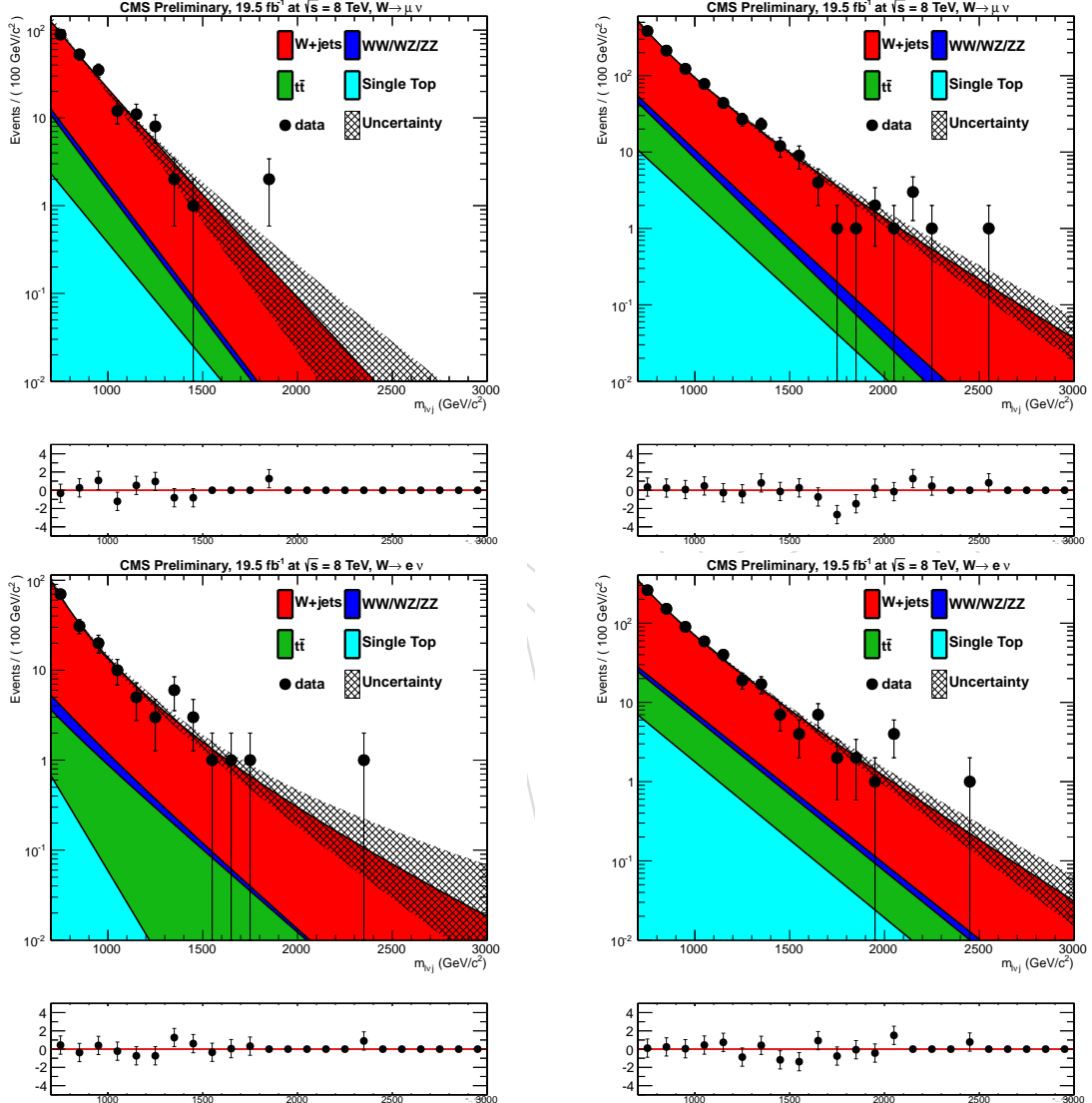


Figure 62:  $m_{lvj}$  sideband fit for  $A1 \rightarrow A2$  extrapolation for events with  $m_{lvj}$  in the range [0.7–3.0] TeV: (top) muon case, (bottom) electron channel. Left column high purity category, right column low purity one.

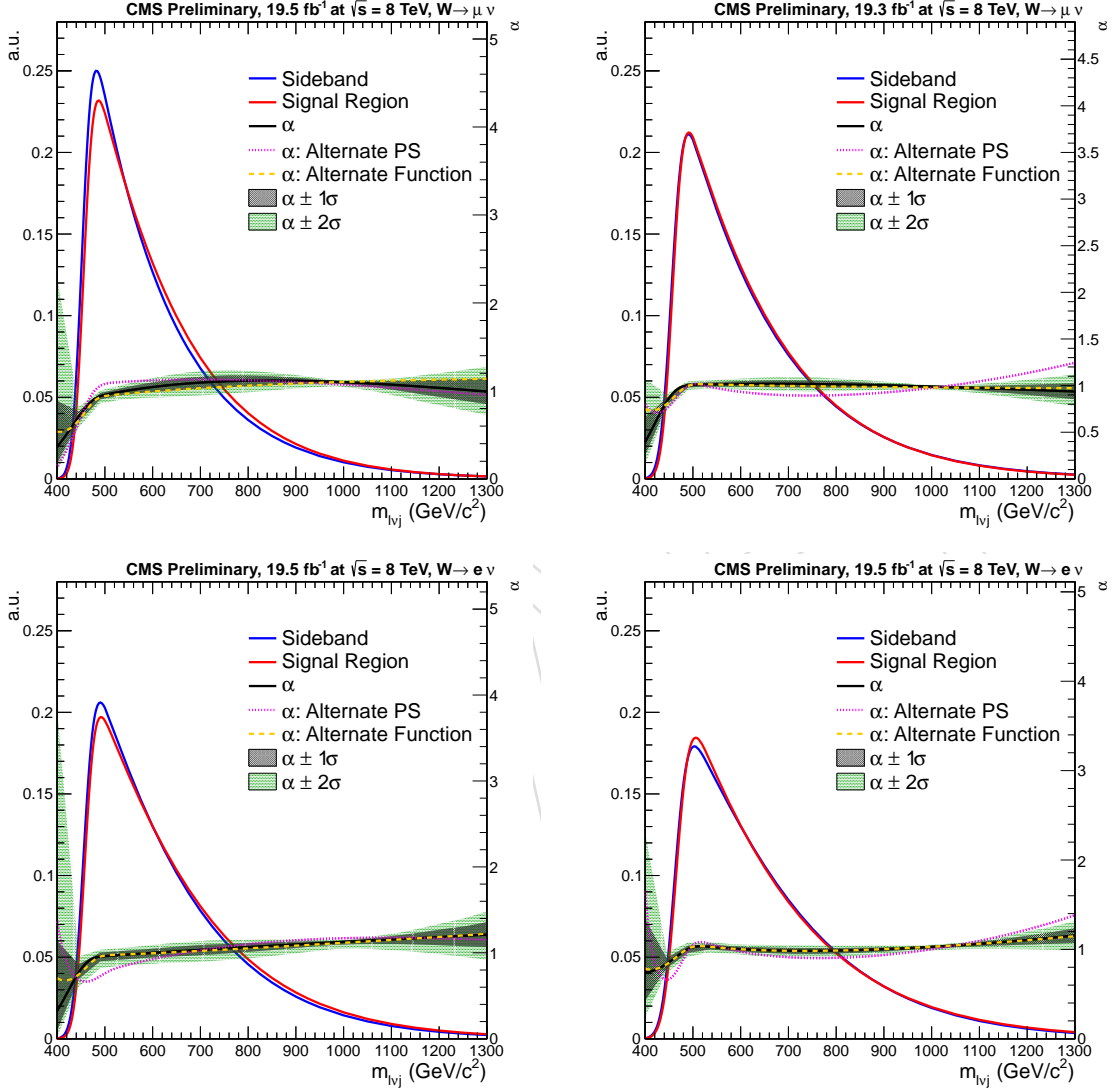


Figure 63:  $\alpha(m_{l\nu j})$  obtained fitting the simulated  $W + \text{jet}$  shapes in the sideband and in the signal region, for events with  $m_{l\nu j} \in [0.4-1.3]$  TeV. Top muon channel: left high purity, right low purity category. Bottom electron channel: left high purity, right low purity category.

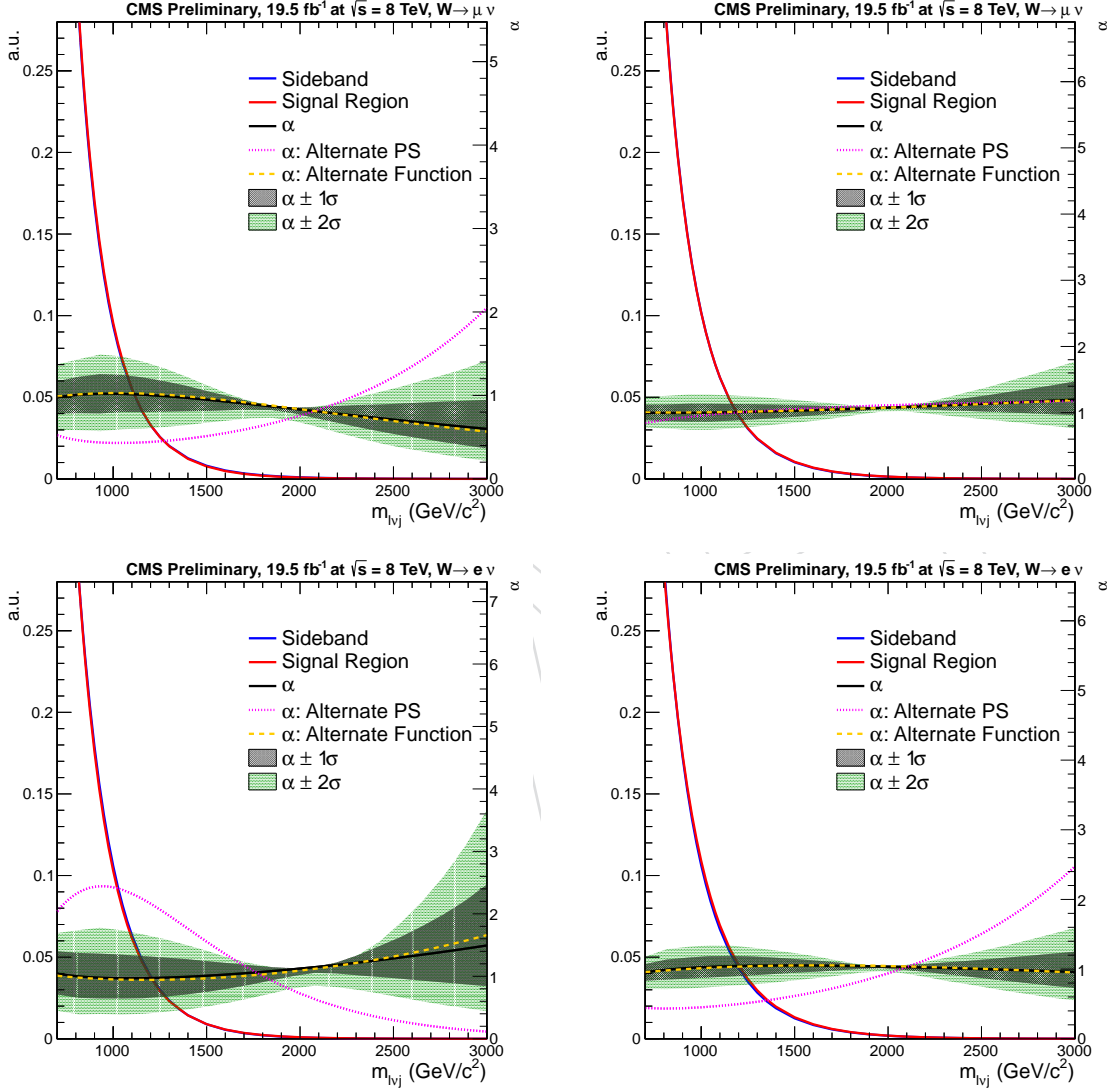


Figure 64:  $\alpha(m_{lvj})$  obtained fitting the simulated  $W + \text{jet}$  shapes in the sideband and in the signal region, for events with  $m_{lvj} \in [0.7\text{-}3.0]$  TeV. Top muon channel: left high purity, right low purity category. Bottom electron channel: left high purity, right low purity category.

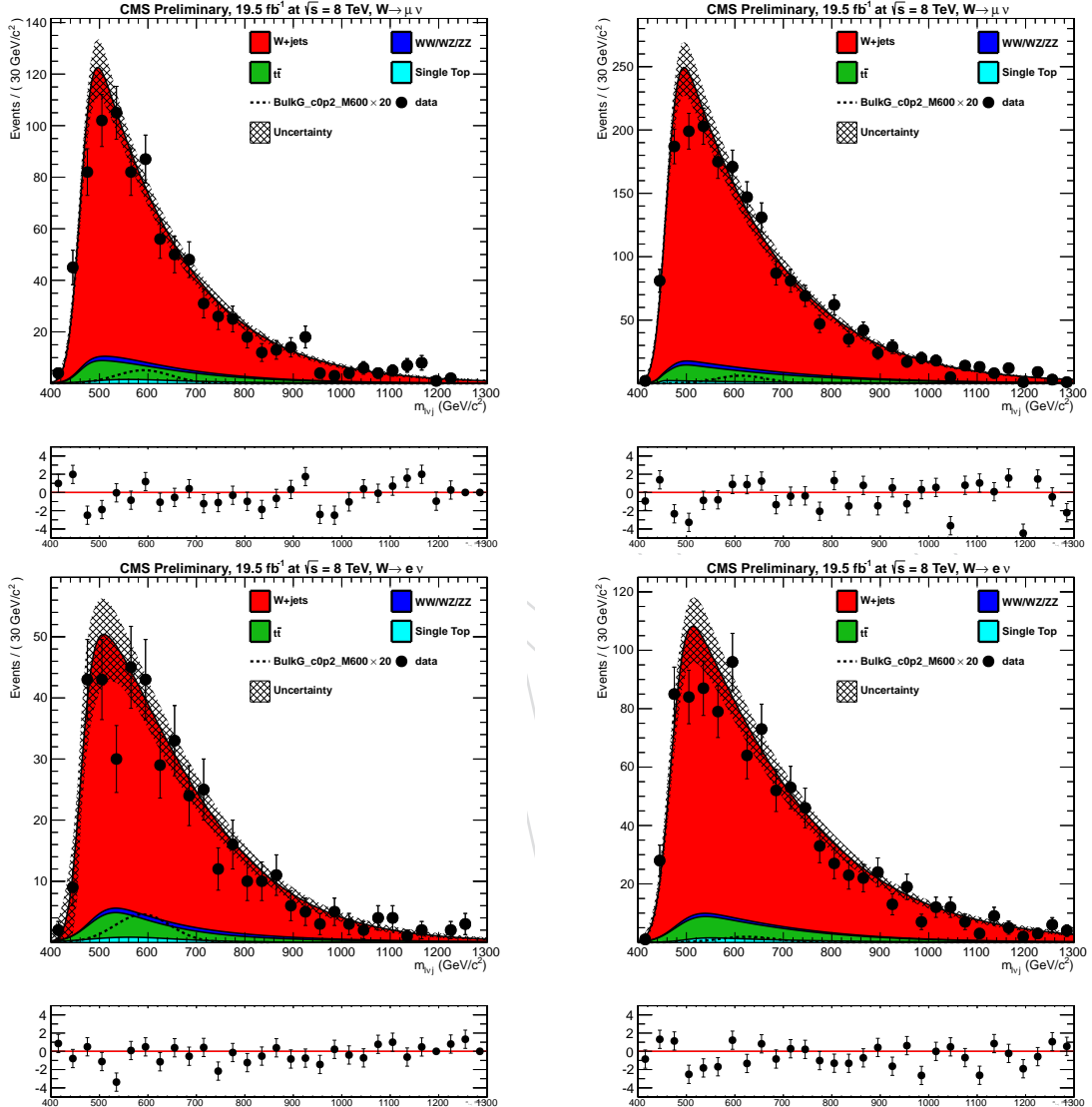


Figure 65: Comparison between data  $m_{lvj}$  distribution and the expected background, for events within A2 with  $m_{lvj} \in [0.4-1.3]$  TeV; in the top line, muon channel results for high purity (left) and low purity (right) categories. Bottom, electron channel result for high purity (left) and low purity (right) categories. In both cases, looking at the pull distributions, the agreement between data and the total background, in an almost signal free region A2, is acceptable.

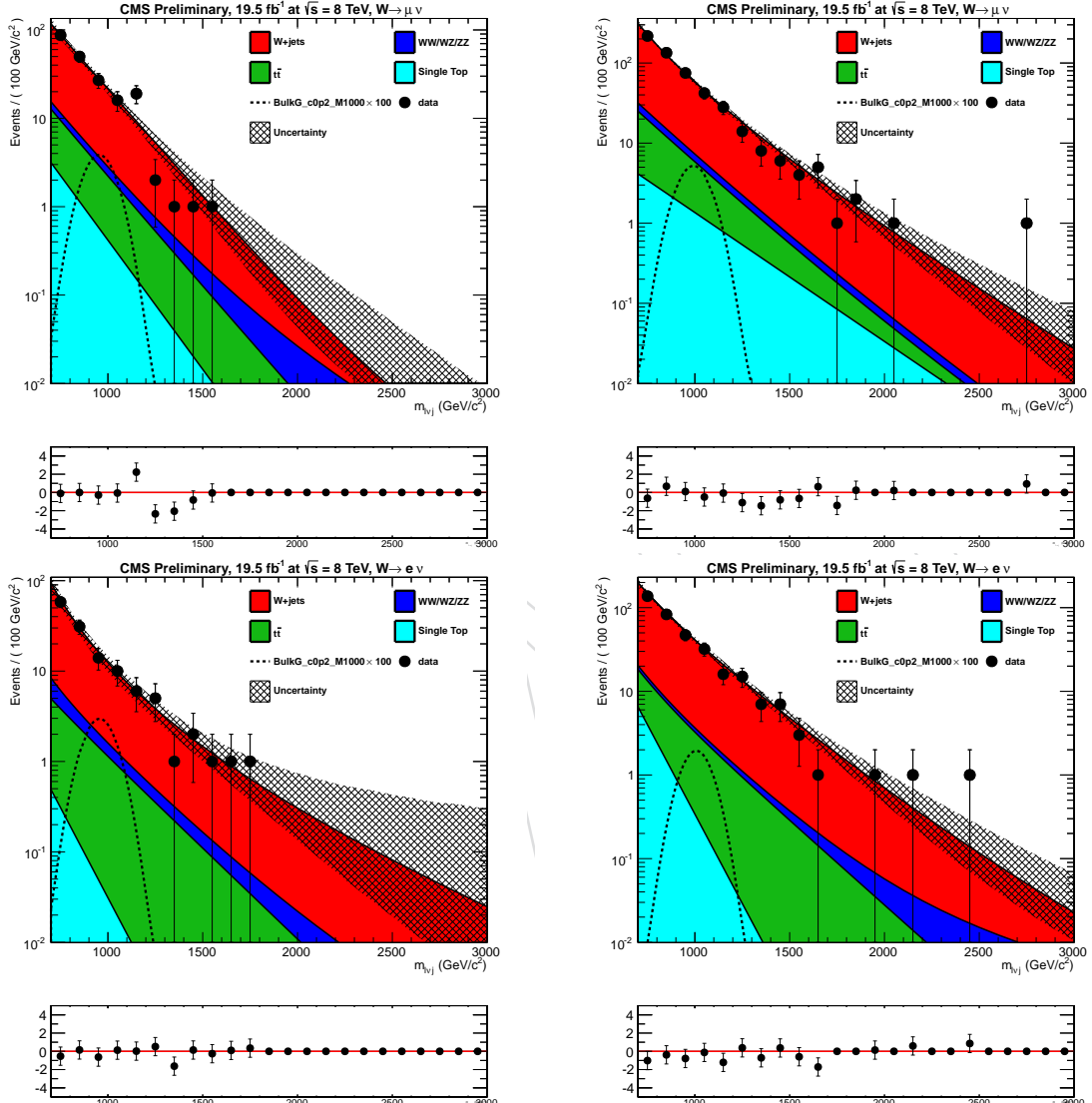


Figure 66: Comparison between data  $m_{lvj}$  distribution and the expected background, for events within A2 with  $m_{lvj} \in [0.7-3.0]$  TeV; in the top line, muon channel results for high purity (left) and low purity (right) categories. Bottom, electron channel result for high purity (left) and low purity (right) categories. In both cases, looking at the pull distributions, the agreement between data and the total background, in an almost signal free region A2, is acceptable.

## 1006 B.2 Closure Test A → B

1007 The background extraction procedure, in particular the data driven estimation of W+jets con-  
 1008 tribution, can be fully validated if it shows a good behaviour for an even larger extrapolation,  
 1009 respect to the one described in Sec. B.1. For this reason, we performed another closure test,  
 1010 extrapolating W+jets background from sideband region A to “signal region” B, as defined in  
 1011 Sec. B.

1012 In Fig. 67 and in Fig. 68, the  $m_j$  fits for the W+jets normalization in the signal region, for the  
 1013 A → B extrapolation, are presented for both muon (top) and electron (bottom) case, high purity  
 1014 (left) and low purity (right) categories.

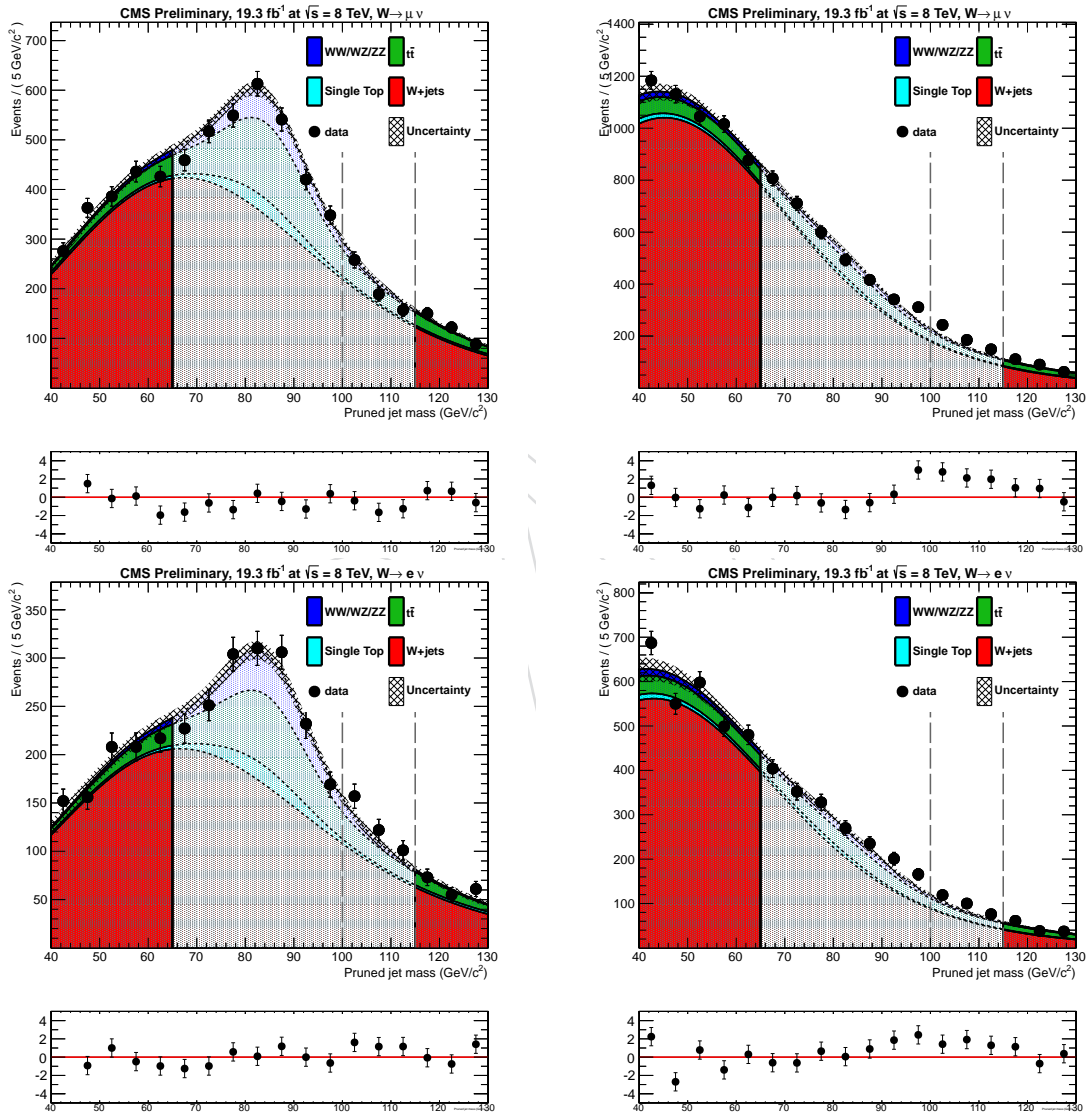


Figure 67: Jet mass  $m_j$  fit in A → B extrapolation, for events with  $m_{l\nu j}$  between [0.4-1.3] TeV: (top) muon case, (bottom) electron channel. Left column high purity category, right low purity one.

1015 In Fig. 69 and in Fig. 70, the data  $m_{l\nu j}$  fits, in the low sideband, are reported for each channel  
 1016 and each category, respectively for events with  $m_{l\nu j}$  between [0.4-1.3] TeV and [0.7-3.0] TeV. The  
 1017 agreement between data and the extracted background shape is consistent for each category  
 1018 and for both muon and electron channel.

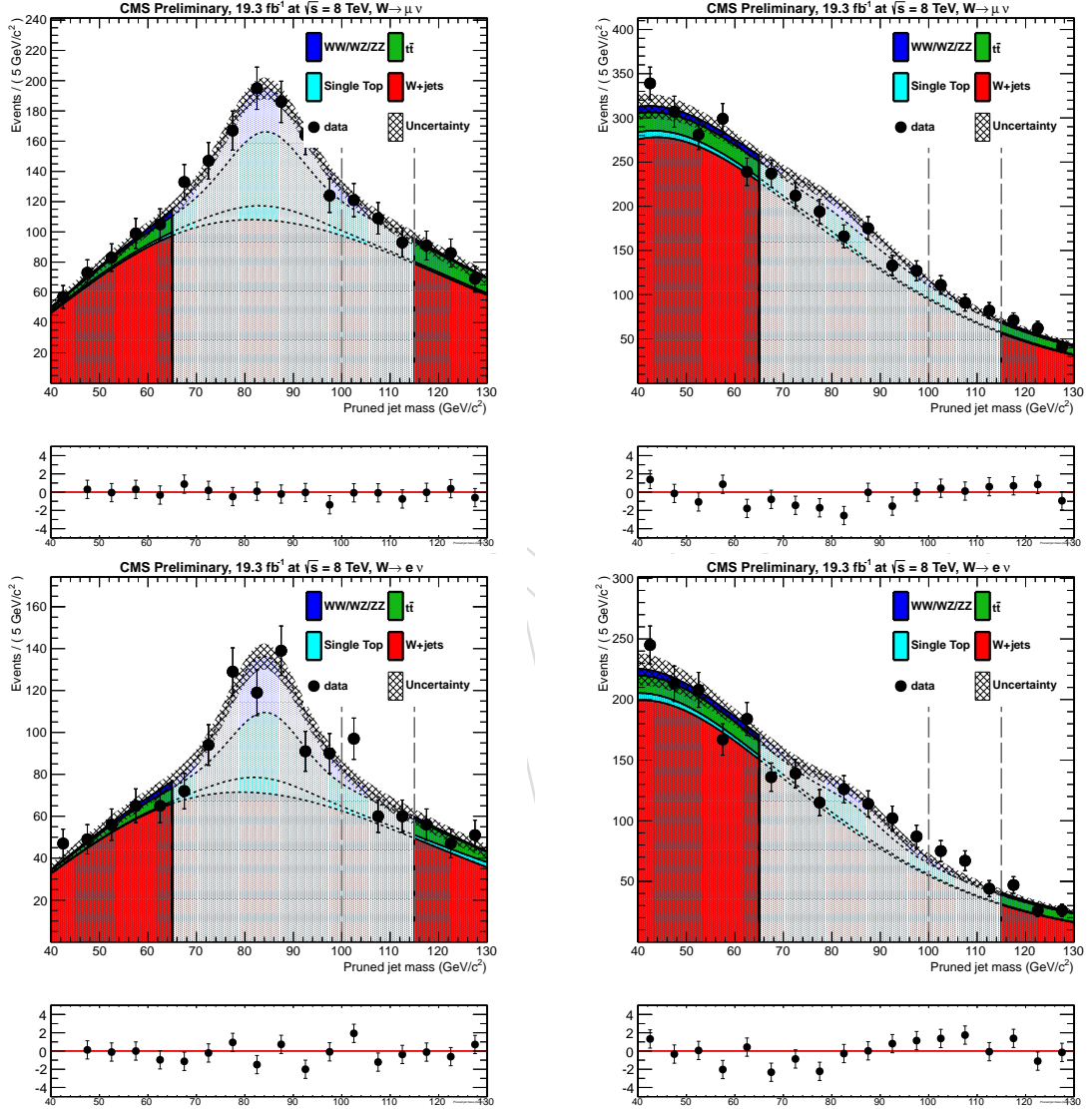


Figure 68: Jet mass  $m_j$  fit in A→B extrapolation, for events with  $m_{l\nu j}$  between [0.8-3.0] TeV: (top) muon case, (bottom) electron channel. Left column high purity category, right low purity one.

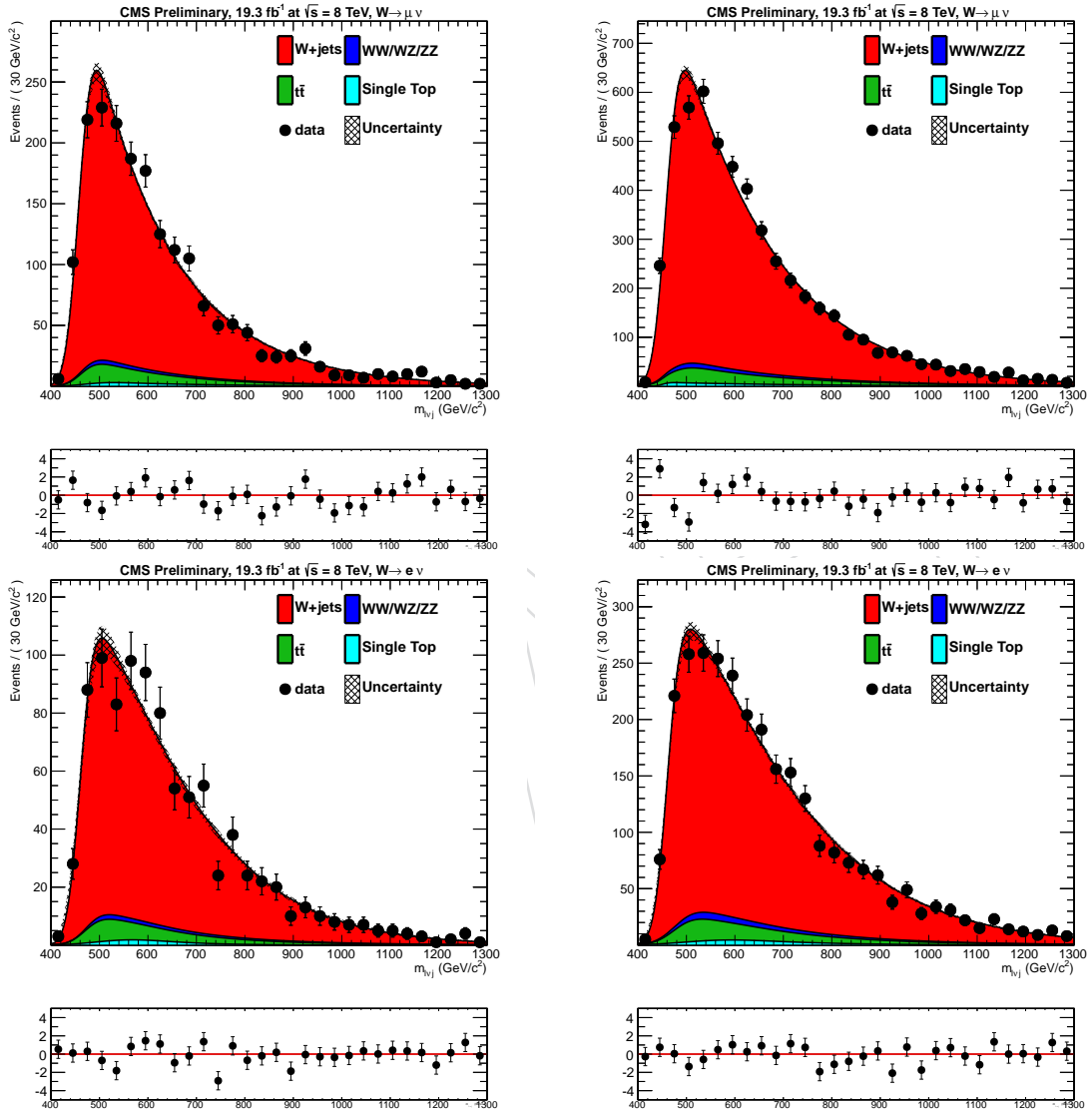


Figure 69:  $m_{lvj}$  fit for A→B extrapolation considering only the events with  $m_{lvj} \in [0.4-1.3]$  TeV : (top) muon case, (bottom) electron channel. Left column high purity category, right low purity one.

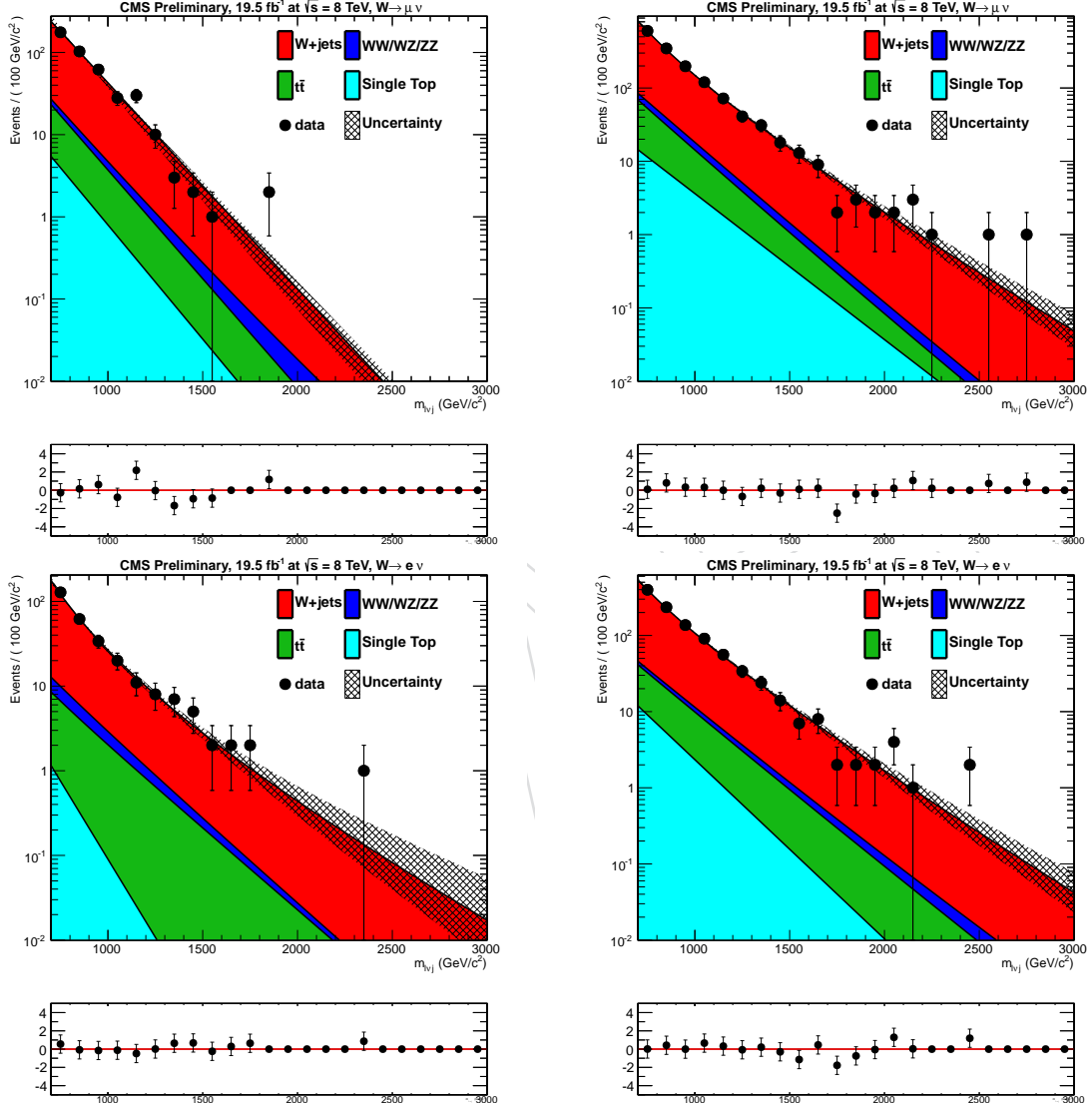
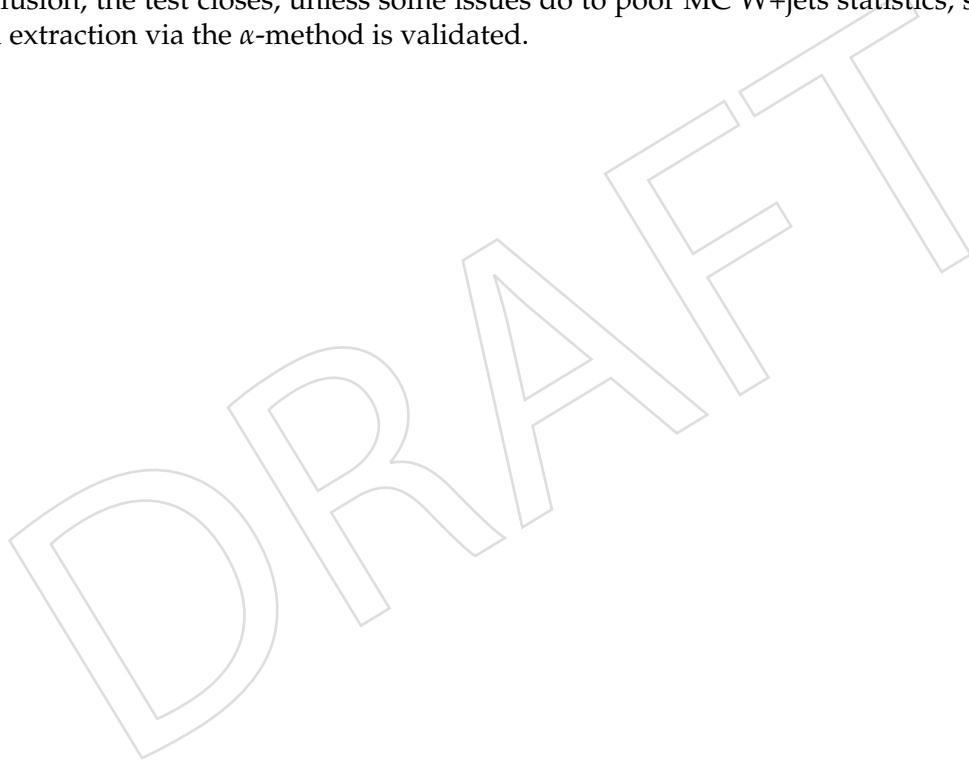


Figure 70:  $m_{lvj}$  fit for A→B extrapolation considering only the events with  $m_{lvj} \in [0.7-3.0]$  TeV: (top) muon case, (bottom) electron channel. Left column high purity category, right low purity one.

- 1019 In Fig. 71 and in Fig. 72, the extrapolation function  $\alpha(m_{lvj})$ , obtained fitting the W+jet MC in  
 1020 both the defined lower sideband and in the signal region, is shown for each channel ( $\mu$  and  $e$ )  
 1021 and each category, respectively for events with  $m_{lvj} \in [0.4\text{-}1.3] \text{ TeV}$  and  $m_{lvj} \in [0.7\text{-}3.0] \text{ TeV}$ .  
 1022 Finally, using the extracted W+jet normalization from fitting data in the  $m_j$  sideband (A) and the  
 1023 shape, drived from fitting data in the sideband of  $m_{lvj}$  times the alpha function, in Fig. 73 and  
 1024 in Fig. 74 , the extracted background prediction can be compared with data in the considered  
 1025 signal region (B) for each channel ( $\mu$  and  $e$ ) and each category.  
 1026 Looking at the pull distributions attached to each plot shown in Fig. 73 and Fig. 74, we can  
 1027 state that a reasonable agreement is found, in each category, between data and the extracted  
 1028 background in a completely signal-free region (B), especially for high mass fits.  
 1029 In fact, in the low mass range ( $m_{lvj} \in [0.4\text{-}1.3] \text{ TeV}$ , see Fig. 73), data and the total background  
 1030 extraction are in a good agreement for high purity categories while, for low purity ones, the  
 1031 peaking part of the spectrum,  $m_{lvj}$  between [550-650] GeV, is not well reproduced and this is  
 1032 probably due to the alpha factor shape.  
 1033 In conclusion, the test closes, unless some issues do to poor MC W+jets statistics; so the back-  
 1034 ground extraction via the  $\alpha$ -method is validated.



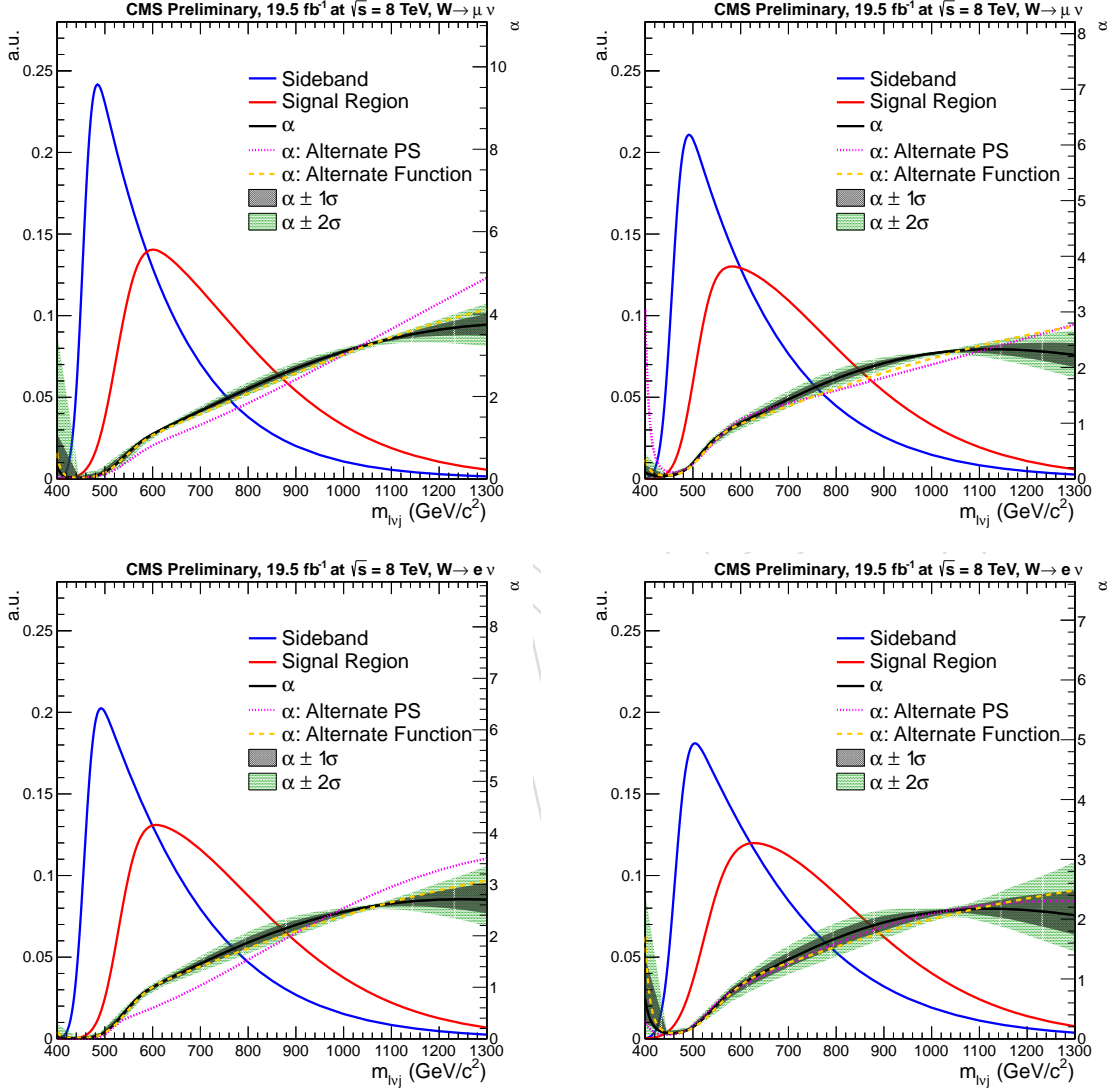


Figure 71:  $\alpha(m_{l\nu j})$  obtained fitting the simulated  $W + \text{jet}$  shapes in the sideband and in the signal region, for events with  $m_{l\nu j}$  in [0.4-1.3] TeV. Top muon channel: left high purity, right low purity category. Bottom electron channel: left high purity, right low purity category.

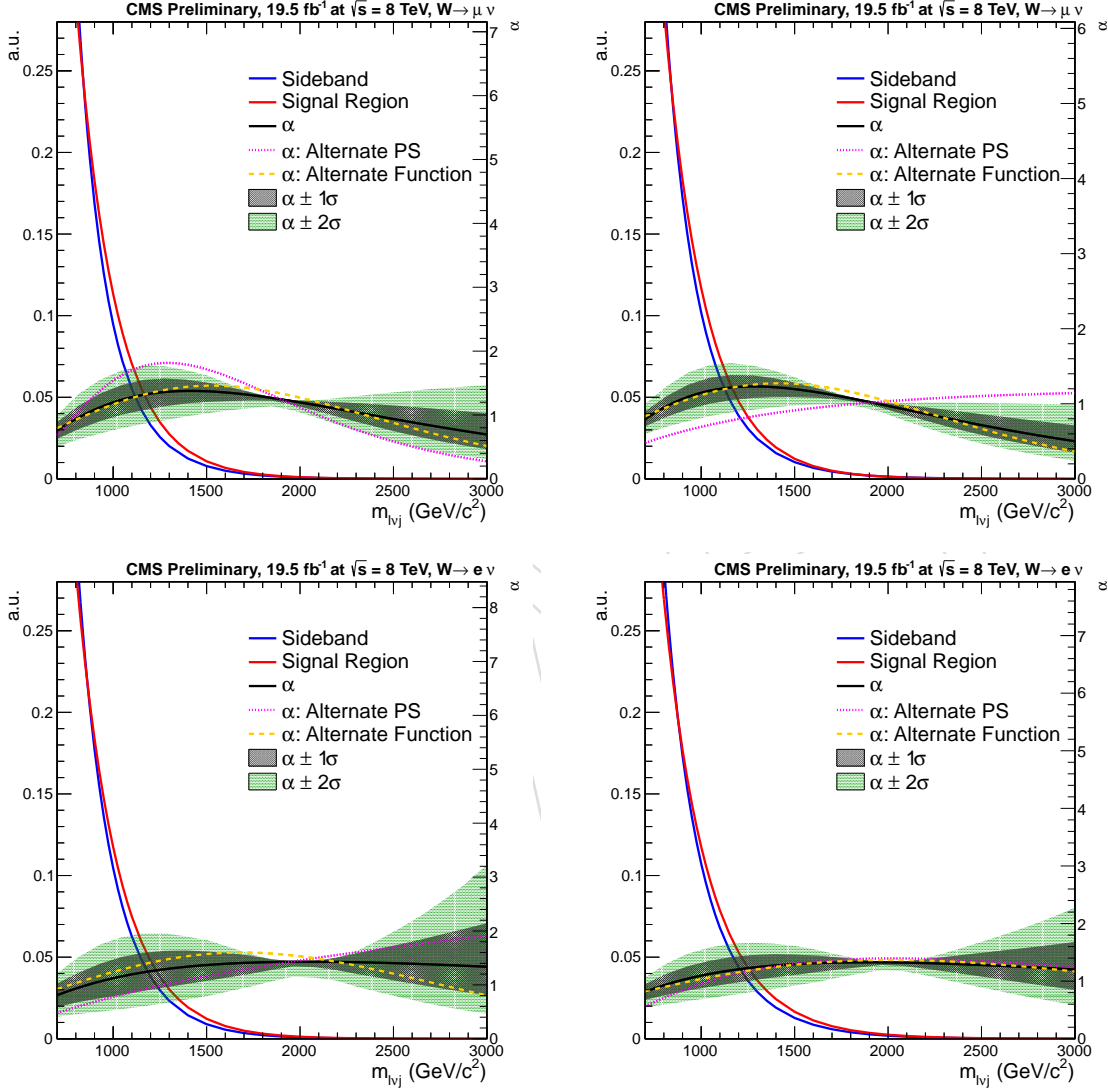


Figure 72:  $\alpha(m_{lvj})$  obtained fitting the simulated  $W+jet$  shapes in the sideband and in the signal region, for events with  $m_{lvj}$  in [0.7-3.0] TeV. Top muon channel: left high purity, right low purity category. Bottom electron channel: left high purity, right low purity category.

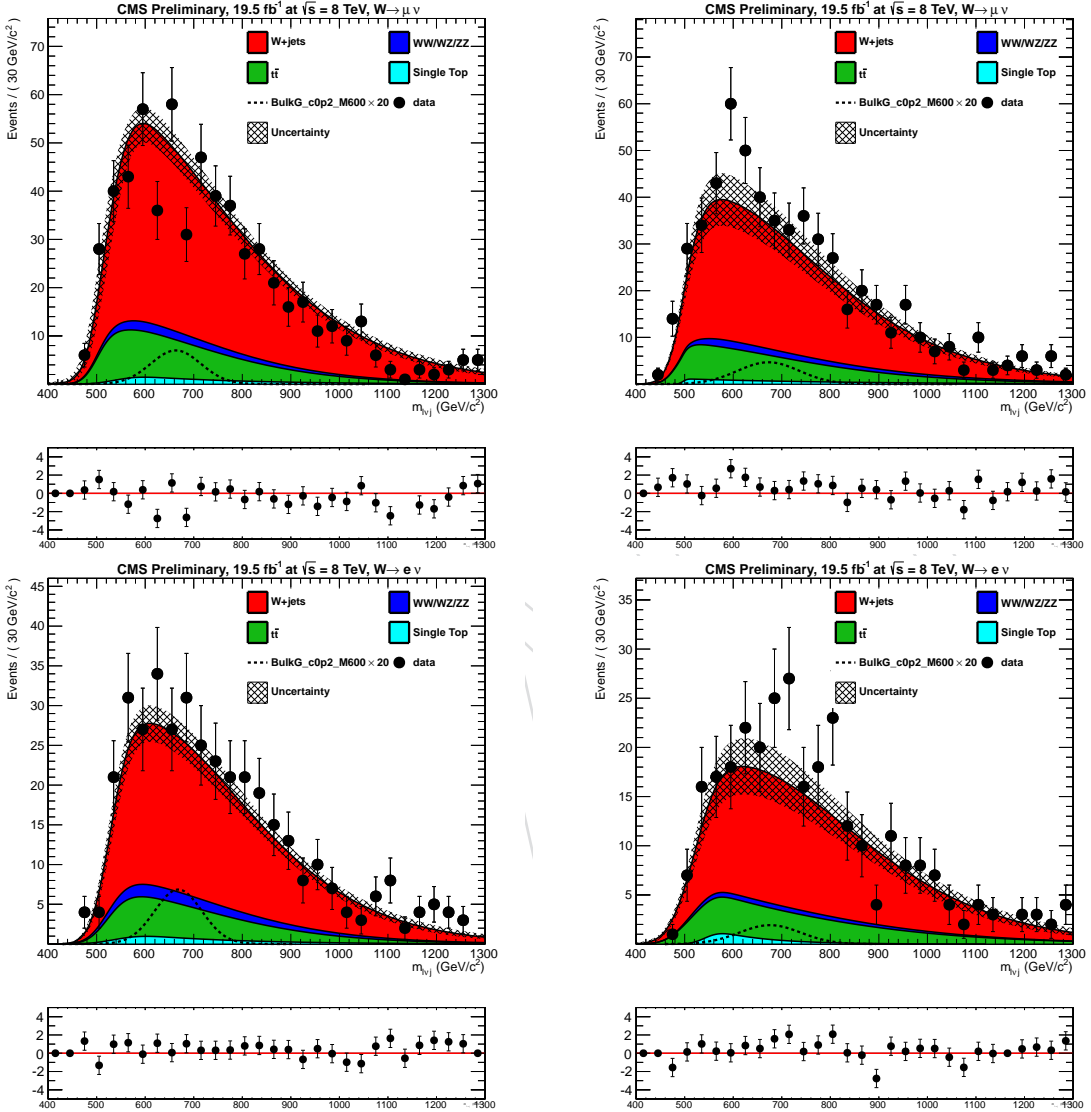


Figure 73: Comparison between data  $m_{lvj}$  distribution and the expected background, for events within B with  $m_{lvj}$  in  $[0.4-1.3]$  TeV; in the top line, muon channel results for high purity (left) and low purity (right) categories. Bottom, electron channel result for high purity (left) and low purity (right) categories. For low purity categories, the peak is not well reproduced, since there the agreement between data and the extracted background is worsening.

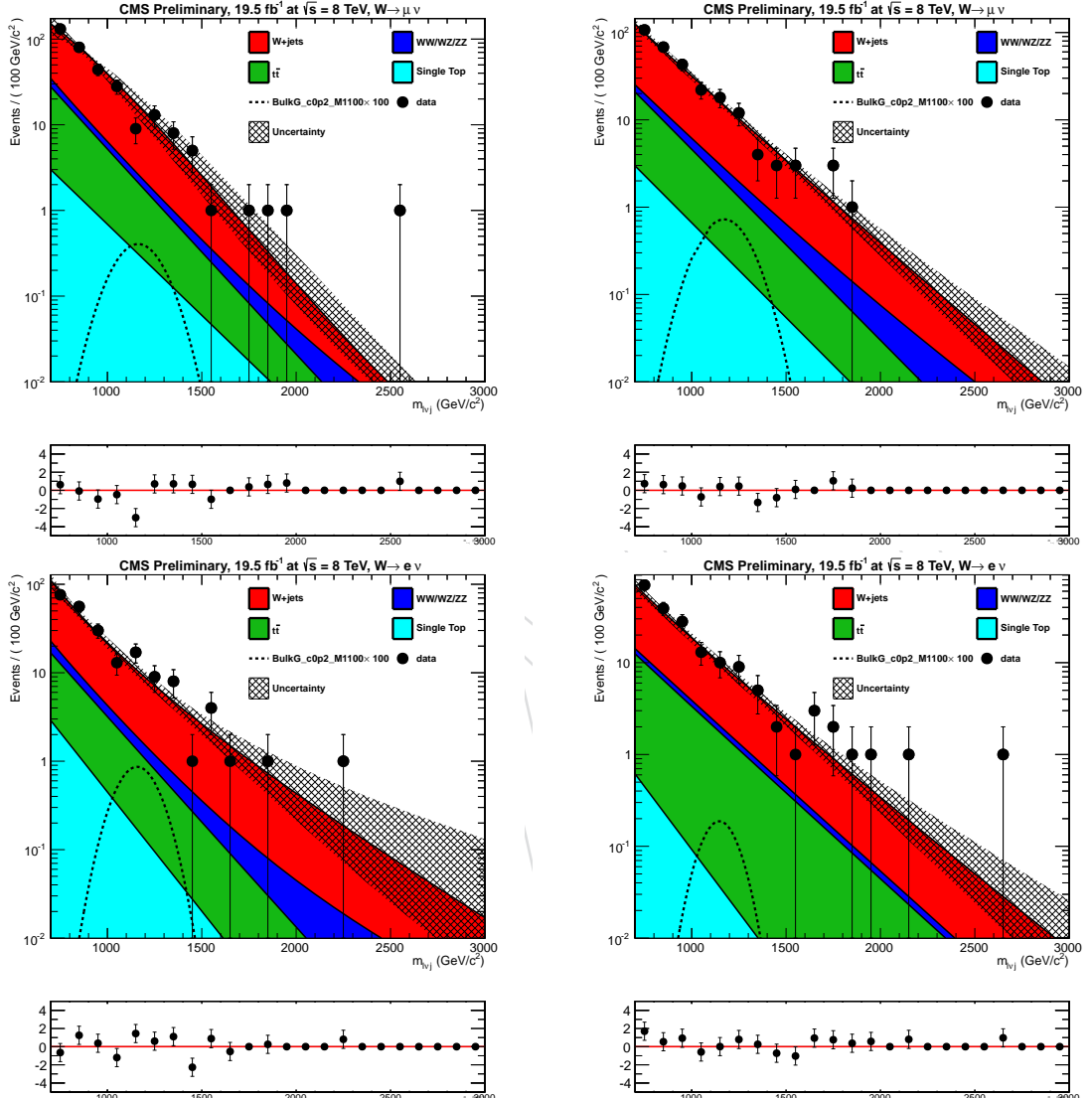


Figure 74: Comparison between data  $m_{lvj}$  distribution and the expected background, for events within B with  $m_{lvj}$  in [0.7-3.0] TeV; in the top line, muon channel results for high purity (left) and low purity (right) categories. Bottom, electron channel result for; high purity (left) and low purity (right) categories. In both cases, looking at the pull distributions, the agreement between data and the total background, in a almost signal free region B, is acceptable considering that, for alpha determination, the MC statistics in region B is limited.

## 1035 C Analysis Robustness Test

1036 In addition to the closure test, described in Sec.B, developed to check the data driven W+jet  
 1037 background extraction procedure, in this section several tests on the limit extraction are per-  
 1038 formed.

### 1039 C.1 Limit Extraction without any Systematic Uncertainty

1040 First of all we checked the effect of the quoted systematic uncertainties, described in Sec.6, on  
 1041 the final analysis result on the Bulk Graviton production cross section upper limit. The obtained  
 1042 results are shown in Fig.75 and in Fig.76 where, respectively, the Asymptotic upper limits for  
 1043 the final combination are reported and for each single category.

1044 If we compare this expected combined limit with the one reported at the end of the analysis in  
 1045 Sec.8.2, we can see that:

- 1046 • At 800 GeV, the sensitivity loss due to the systematics is at the level of  $\approx 38\%$ , in-fact  
 1047 the upper bound moves from 0.60 pb to 0.37 pb.
- 1048 • At 1.6 TeV, this effect is less pronounced, at the level of  $\approx 15\%$ . In-fact the upper  
 1049 bound moves from 0.55 pb to 0.65 pb.
- 1050 • Finally at 2.4 TeV, the difference is only at  $\approx 5.5\%$  so here the performance of the  
 1051 analysis are dominated by the actual statics.

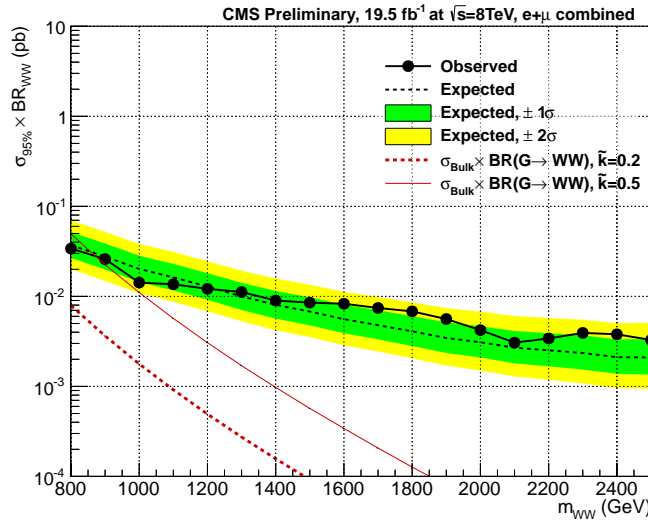


Figure 75: Observed (solid) and expected (dashed) 95% CL upper limit on the graviton production cross section times the branching fraction of  $G \rightarrow WW$  using  $19.3 fb^{-1}$  of data, obtained avoiding any systematic uncertainty. The 68% and 95% ranges of expectation are also shown with green and yellow bands. The expected product between the Bulk graviton production cross section and the branching fraction is shown as a red dashed (solid) curve for  $\tilde{k} = 0.2$  ( $\tilde{k} = 0.5$ ).

### 1052 C.2 Limit Extraction without Systematic Uncertainty on Alpha

1053 As explained in Sec.6.1.1, the extrapolation function  $\alpha$  has is sensitive to alternative fitting func-  
 1054 tions and parton shower models; this brings us to inflate its statistical uncertainty by a factor  
 1055 two during the limit extraction. The effect on the final expected and observed limit, due to this

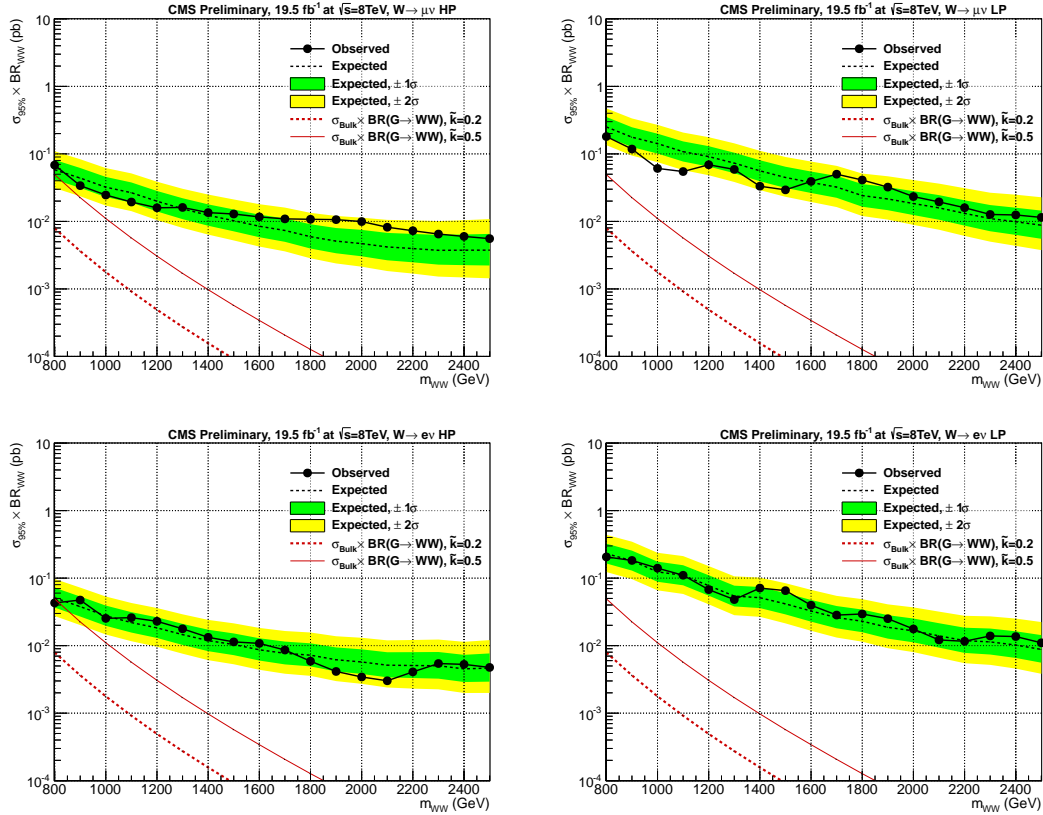


Figure 76: Observed (solid) and expected (dashed) 95% CL upper limit on graviton production cross section times the branching fraction of  $G \rightarrow WW$  using  $19.3 fb^{-1}$  of data, obtained avoiding any systematic uncertainty. The 68% and 95% ranges of expectation are also shown with green and yellow bands. Top panel: results for muon channel, HP category on the left, LP on the right. Bottom pnnel: results for electron channel, HP category on the left, LP on the right.

1056 conservative approach, has been studied running the full analysis chain without any systematic  
 1057 uncertainty on the alpha function.

1058 In Fig.78, the left plot shows the combined upper limit, while on the right there is a direct  
 1059 comparison between median expected and observed limit obtained with and without the alpha  
 1060 systematic uncertainty.

1061 The effect of this systematic on the final limit, both on the expected and the observed ones, is  
 1062 important at low mass, 16% at 800 GeV, but it remains stable at 4% level for each mass point  
 1063 above 1.2 TeV.

### 1064 C.3 Limit Extraction without Low Purity Categories

1065 Another interesting study is to study the contribution of LP categories in the final combined  
 1066 cross section upper limit. To quantify this effect, the combined limit has been extracted using  
 1067 only HP categories and compared with the one reported in Sec.8.2.

1068 In Fig.78, the left plot shows the upper limit obtained combining only HP electron and muon  
 1069 channels, while on the right there is a direct comparison between median expected and ob-  
 1070 served limits obtained with and without the contribution of LP categories.

1071 The gain on the expected cross section upper limit is limited at 2-4% till 2 TeV, while, for very

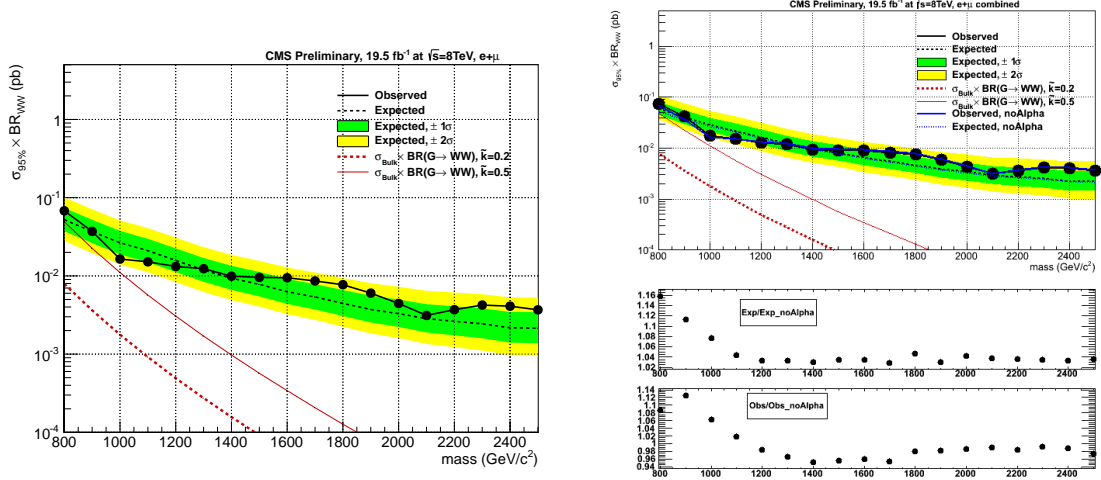


Figure 77: Observed (solid) and expected (dashed) 95% CL upper limit on graviton production cross section times the branching fraction of  $G \rightarrow WW$  using  $19.3\text{ fb}^{-1}$  of data: (Left) result obtained running the asymptotic CLs without any systematic uncertainty on alpha. (Right) comparison between observed and expected limits obtained in the standard configuration (black) and without the alpha uncertainty (blue).

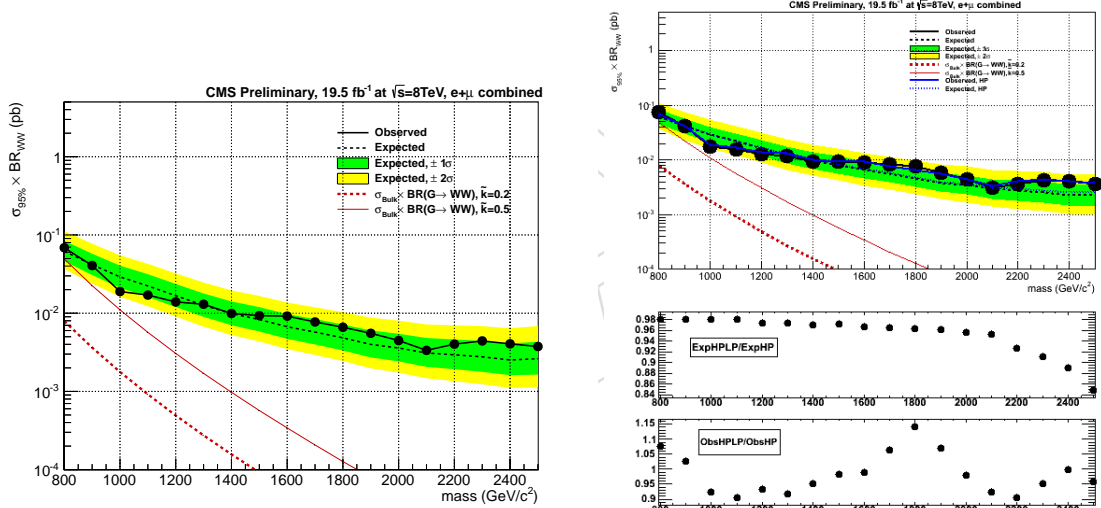


Figure 78: Observed (solid) and expected (dashed) 95% CL upper limit on graviton production cross section times the branching fraction of  $G \rightarrow WW$  using  $19.3\text{ fb}^{-1}$  of data: (Left) result obtained running the asymptotic CLs combining only HP categories. (Right) comparison between observed and expected limits obtained in the standard configuration (black, HP+LP) and without LP categories (blue).

high mass resonances  $m_G > 2\text{ TeV}$ , the effect is mass dependent and varies from 5% to 16%. This is essentially due to a degradation of the pruned mass resolution for high boosted W-jet, which brings a migration of signal events from HP to LP category at high mass.

#### C.4 Limit Extraction with full CLs

Limit results obtained through the Asymptotic CLs method and reported in Sec. 8.2 are cross checked with the modified frequentist CLs (full CLs) [25]. The comparison between Asymptotic results and full CLs is performed only for a set of 4 chosen mass point ( $m_G = 0.8, 1.2, 1.6, 2.4$

1079 TeV). This is why, since the full CLs method requires to compute a grid of the the test statics  
1080 distribution before the evaluation of the observed and expected upper limit, this procedure is  
1081 time consuming and is used only to cross check the reliability of the Asymptotic model. Re-  
1082 sults are reported in Table 13 where observed, expected and 68% bounds are compared for each  
1083 mass point and each category.

1084 Looking at the total combination, observed and expected limits, derived with Asymptotic and  
1085 full CLs, agree within 2-3% for  $m_G = [0.8,1.2,1.6]$  TeV, while they disagree by 5% at 2.4 TeV. It is  
1086 however significantly smaller than the size of the 68% interval of the expected limit.

DRAFT

$m_G$ (TeV)	Obs (Asy)	Obs (CLs)	Exp (Asy)	Exp (CLs)	$\pm 1\sigma$ (Asy)	$\pm 1\sigma$ (CLs)
Muon Channel High Purity						
0.8	13.56	14.08±0.17	10.10	10.92±0.09	14.54 (7.18)	15.34±0.11 (7.71±0.08)
1.2	37.04	38.09±0.29	49.80	50.35±0.95	71.44 (35.00)	73.12±0.69 (33.89±0.84)
1.6	223.75	228.90±2.07	175.78	179.60±1.65	261.96 (120.72)	258.9±2.04 (128.40±1.58)
2.4	4338.20	4366±50.62	2881.25	2947±52.46	4925.54 (2733.21)	4054±175.3 (2777±70.42)
Muon Channel Low Purity						
0.8	70.69	73.241.91	51.36	52.73±0.71	79.41 (25.08)	83.24±1.15 (28.26±0.53)
1.2	231.16	234.5±2.69	260.15	260.70±5.76	406.37 (175.06)	412.3±4.44 (181.00±6.23)
1.6	1029.17	1020±43.54	946.87	963.90±15.37	1484.14 (628.61)	1454±10.92 (659.80±11.61)
2.4	11207.78	11711±184.6	9350.34	9524±104.6	15984.5 (5793.6)	15450±223.4 (6461±98.95)
Electron Channel High Purity						
0.8	8.98	9.39±0.09	8.66	9.03±0.11	12.43 (6.14)	12.93±0.55 (4.51±0.21)
1.2	48.79	50.44±0.56	45.51	44.15±1.55	66.01 (23.73)	66.91±0.81 (22.97±0.59)
1.6	228.58	217.5±7.92	183.59	183.9±4.04	272.14 (126.31)	269.5±3.49 (135.5±1.95)
2.4	4222.67	4344±39.95	3381.25	3511±54.25	5510.74 (2143.67)	4896±43.13 (2635±91.53)
Electron Channel Low Purity						
0.8	45.15	45.89±2.14	42.38	44.85±0.91	65.86 (28.82)	69.95±2.05 (31.16±0.37)
1.2	153.15	152.5±1.99	216.40	217.10±2.05	338.03 (145.62)	332.80±4.22 (147.30±1.88)
1.6	888.10	902 <sup>+11.2</sup> <sub>-11.2</sub>	762.5	748±9.81	1209.28 (535.25)	1176±26.89 (553.1±9.3)
2.4	11812.44	12270±106.1	8825	9269±128.7	14945.77 (5491.05)	13200±322.7 (6887±72.9)
Final Combination						
0.8	9.15	9.35±0.13	6.61	6.75±0.50	9.38 (4.74)	9.68±0.25 (4.82±0.12)
1.2	26.15	26.52±0.28	32.13	32.94±1.36	45.83 (22.85)	47.00±0.38 (24.21±0.41)
1.6	165.94	165.9±1.95	117.58	116.9±1.69	171.47 (82.34)	174.1±1.82 (90.54±12.54)
2.4	2988.02	3131±36.11	1656.25	1730±27.15	2613.52 (1073.92)	2295±87.7 (1339±19.14)

Table 13: Comparison between limits obtained with the Asymptotic and the full CLs for four chosen mass point  $m_G = [0.8, 1.2, 1.6, 2.4]$  TeV in each category and for the final combination. From left to right, the following values are reported: observed limit, expected limit and 68% confidence belt around the expected one. Statistical error coming from toys is reported on each value given by the full CLs.

1087 **References**

- 1088 [1] K. Agashe, H. Davoudiasl, G. Perez, and A. Soni, "Warped gravitons at the CERN LHC  
1089 and beyond", *Phys. Rev. D* **76** (Aug, 2007) 036006,  
1090 doi:10.1103/PhysRevD.76.036006.
- 1091 [2] Y. Gao et al., "Spin determination of single-produced resonances at hadron colliders",  
1092 *Phys. Rev. D* **81** (Apr, 2010) 075022, doi:10.1103/PhysRevD.81.075022.
- 1093 [3] S. Bolognesi et al., "Spin and parity of a single-produced resonance at the LHC", *Phys.*  
1094 *Rev. D* **86** (Nov, 2012) 095031, doi:10.1103/PhysRevD.86.095031.
- 1095 [4] A. Belyaev, N. D. Christensen, and A. Pukhov, "CalcHEP 3.4for collider physics within  
1096 and beyond the Standard Model", *Computer Physics Communications* **184** (2013), no. 7,  
1097 1729 – 1769, doi:10.1016/j.cpc.2013.01.014.
- 1098 [5] "Electron reconstruction and identification at  $\sqrt{s} = 7$  TeV", Technical Report  
1099 CMS-PAS-EGM-10-004, CERN, Geneva, (2010).
- 1100 [6] T. C. collaboration, "Performance of CMS muon reconstruction in pp collision events at  $s$   
1101 = 7 TeV", *Journal of Instrumentation* **7** (2012), no. 10, P10002.
- 1102 [7] CMS Collaboration, "Particle-Flow Event Reconstruction in CMS and Performance for  
1103 Jets, Taus, and MET", *CMS PAS PFT-2009-001* (Apr, 2009).
- 1104 [8] CMS Collaboration, "Jet Performance in pp Collisions at  $\sqrt{s}=7$  TeV", CMS Physics  
1105 Analysis Summary CMS-PAS-JME-10-003, (2010).
- 1106 [9] CMS Collaboration, "Commissioning of the Particle-Flow Reconstruction in  
1107 Minimum-Bias and Jet Events from pp Collisions at 7 TeV", *CMS PAS PFT-2010-002*  
1108 (2010).
- 1109 [10] M. Cacciari, G. P. Salam, and G. Soyez, "The anti- $k_t$  jet clustering algorithm", *JHEP* **04**  
1110 (2008) 063, doi:10.1088/1126-6708/2008/04/063, arXiv:0802.1189.
- 1111 [11] Y. L. Dokshitzer, G. Leder, S. Moretti, and B. Webber, "Better jet clustering algorithms",  
1112 *JHEP* **9708** (1997) 001, arXiv:hep-ph/9707323.
- 1113 [12] CMS Collaboration, "Determination of the jet energy scale in CMS with pp collisions at  
1114  $\sqrt{s} = 7$  TeV", *CMS PAS JME-10-010* (2010).
- 1115 [13] "CMS MET Performance in Events Containing Electroweak Bosons from pp Collisions at  
1116  $\sqrt{s}=7$  TeV".
- 1117 [14] C. Collaboration, "Search for new physics in the single lepton + MET final states with full  
1118 2012 dataset at  $\sqrt{(s)} = 8$  TeV", cms-an-2012/423.
- 1119 [15] B. C. et al, "Search for High Mass Resonances Decaying to Electron Pairs at 8 TeV with  
1120 the Full 2012 dastae", cms-an-2012/415.
- 1121 [16] CMS Collaboration, "Performance of CMS muon identification in pp collisions at  $\sqrt{s} = 7$   
1122 TeV", *CMS PAS MUO-2010-002* (2010).
- 1123 [17] N. T. et al., "Identifying hadronically decaying W bosons merged into a single jet",  
1124 cms-an-2013/72.

- [18] C. Collaboration, "Searches for new physics in the  $WW \rightarrow l\nu j$  final state with hadronic W bosons merged into a single jet", cms-an-2012/381.
- [19] J. Thaler and K. Van Tilburg, "Identifying Boosted Objects with N-subjettiness", *JHEP* **1103** (2011) 015, doi:10.1007/JHEP03(2011)015, arXiv:1011.2268.
- [20] "Search for a Standard Model-like Higgs boson decaying into WW to l nu qqbar in pp collisions at sqrt s = 8 TeV", Technical Report CMS-PAS-HIG-13-008, CERN, Geneva, (2013).
- [21] F. S. et al., "Search for BSM resonance decaying to W vector bosons in the semileptonic final state", cms-an-2013/45.
- [22] Bortignon, Pierluigi et al., "Search for the Standard Model Higgs Boson Produced in Association with W and Z and Decaying to Bottom Quarks (HCP 2012)".
- [23] CMS Collaboration *PAS SMP-12-019* (2012).
- [24] C. Collaboration, "Combined results of searches for the standard model Higgs boson in pp collisions at  $\sqrt{s} = 7$  TeV", CMS Physics Analysis Summary CMS-PAS-HIG-11-032 2011/32, (2011).
- [25] A. L. Read, "Presentation of search results: the CL s technique", *Journal of Physics G: Nuclear and Particle Physics* **28** (2002), no. 10, 2693.

DRAFT